Diss. ETH No. 15519

GEOSCIENTIFIC INVESTIGATIONS FOR THE USE OF SHALLOW LOW-ENTHALPY SYSTEMS

A dissertation submitted to the

SWISS FEDERAL INSTITUTE OF TECHNOLOGY ZURICH

For the degree of

Doctor of Science

presented by

SARAH SIGNORELLI

Dipl. Natw. ETHZ

Born 25. April 1974

Citizen of Trimbach (SO)

Accepted on the recommendation of

PD Dr. Thomas Kohl, examiner

Prof. Dr. William Lowrie, co-examiner

Prof. Dr. Ladislaus Rybach, co-examiner

Prof. Dr. Christoph Clauser, co-examiner

2004

VORWORT

Diese Arbeit wäre ohne die Unterstützung verschiedener Personen nicht möglich gewesen. Ein spezielles Dankeschön geht an:

Thomas Kohl, für die Möglichkeit im meinem Wunschgebiet eine Doktorarbeit zu schreiben, für die Übernahme des Referates, für seine Unterstützung und sein Vertrauen.

Ladislaus Rybach, für die Übernahme des Korreferates, die stete Unterstützung und die vielen hilfreichen Diskussionen.

William Lowrie und Christoph Clauser, für die Übernahme des Korreferates und ihr Interesse an meiner Arbeit.

Ernst Rohner, von dessen Erfahrung im Bereich Erdwärmenutzung ich viel lernen konnte.

Wolfgang Rogg, durch dessen Einsatz dieses Dissertationsprojekt überhaupt erst zu Stande kam.

Christoph Bärlocher, der mit endloser Geduld alle meine Computer-Probleme löste, Viren und Hacker abwehrte.

Simone Bassetti, der viel zu dieser Arbeit beigetragen hat.

Nathalie Andenmatten Berthoud für die Bereitstellung des dreidimensionalen geologischen Models der Stadt Zürich und ihre Freundschaft.

Dominique Bächler, Sibylle Steimen, Michael Schnellmann, Silvio Maraini und Adrian Wyss, für die gute Zeit und die ablenkenden Gespräche in den Kaffeepausen.

Michelle Hug and Scott Putnam are warmly acknowledged for proof-reading the thesis.

Meine Eltern und meine Grossmutter, für die nie endende moralische und finanzielle Unterstützung.

Meine Schwester, fürs Zuhören.

Andreas Schroeder, dafür dass er immer für mich da war.

Diese Dissertation wurde vom Projekt- und Studienfond der Elektrizitätswirtschaft (PSEL) und vom Bundesamt für Energie (BFE) finanziert.

ABSTRACT

This presented study is part of the research project: "Productivity Investigation of the System Borehole Heat Exchanger (BHE) with Heat Pump", financed by the Projekt und Studienfond der Elektizitätswirtschaft (PSEL) and the Swiss Federal Office of Energy (BFE). It was jointly performed at the Institute of Geophysics and at the "Elektrizitätswerke des Kantons Zürich" (EKZ) (by order of the "Nord-Ostschweizerische Kraftwerke" NOK). The study aimed at the understanding of the scientific basis and the performance improvement of shallow low-enthalpy systems such as geothermal heat pumps. This includes a variety of subjects:

The 3D Finite Element modeling software FRACTure is used to simulate the hydraulic and thermal processes related to the operation of borehole heat exchanger (BHE). The suitability of FRACTure to simulate a BHE is demonstrated by performing various sensitivity studies. This is emphasized furthermore by a simulative comparison with the semi-analytical software EED and by validation with measured data.

The modeling parameters which largely determine the dimensioning of a BHE system are the ground surface temperature (GST) and the thermal conductivity of the subsurface. Methods to estimate these two factors are presented and discussed.

A regional GST analysis of Switzerland was performed considering both climatic and geothermal data. The altitude dependence of GST and the relationship between GST and surface air temperature was investigated carefully. By further processing, a GST map for Switzerland was generated. The results are important for evaluating geothermal resources and determines regional GST distribution under different climatic conditions typical in central Europe.

Thermal response tests became popular to measure the in-situ thermal conductivity. The breadth of their ideal application is investigated by FRACTure simulations. The applied procedure provides information about the necessary test duration, and the effects of heterogeneous subsurface conditions, groundwater movement, and of variable data quality. The results indicate that most thermal response tests underestimate the thermal conductivity; the difference can amount to over -10 %. A comparative analytical and numerical evaluation of an actual thermal response test

emphasizes the importance of more sophisticated numerical methodologies for thermal response test interpretation.

The evaluation of GST and thermal conductivity represents a common geoscientific aspect of applied and general geothermal research. Here, the influence of these two parameters on the performance of a single BHE system is determined by two sensitivity studies and visualized for different locations in Switzerland. GST can have a more dominate impact on the power production than thermal conductivity.

In the final step, the sustainable behavior of a BHE field is investigated. The results (ground temperatures and BHE delivery temperatures) are compared to a single BHE of the same length. In a BHE array, the recovery time is longer than for a single BHE. The BHE array spacing is a critical parameter in the investigated example; the minimum distance shall not fall short of 7 m to provide sustainable production. The lower temperatures of the production fluid can be compensated for by drilling additional meters. Estimates of the additional drilling necessary are given for certain conditions. The investigation shows that sustainable production from a BHE field can be achieved by proper design.

ZUSAMMENFASSUNG

Die vorliegende Arbeit ist Teil des Forschungsprojekts „Produktivitätsuntersuchung des Systems Erdwärmesonde mit Wärmepumpe“, welches vom Projekt- und Studienfond der Elektrizitätswirtschaft (PSEL) und vom Bundesamt für Energie (BFE) finanziert wurde. Dieses Projekt wurde am Institut für Geophysik der ETH Zürich und bei den „Elektrizitätswerken des Kantons Zürich“ (EKZ) (im Auftrag der „Nord-Ostschweizerischen Kraftwerke“ NOK) gemeinsam durchgeführt. Das Ziel dieser Arbeit war die Erarbeitung wissenschaftlicher Grundlagen für untiefe Niedrig-Enthalpie-Systeme wie Erdwärmepumpen und deren Betriebsoptimierung. Dies beinhaltet eine Vielzahl von Aufgaben:

Für die Simulation von hydraulischen und thermischen Prozessen in Zusammenhang mit dem Betrieb von Erdwärmesonden (EWS) wird die 3D Finite Elemente Software FRACTure verwendet. Die Leistungsfähigkeit von FRACTure zur Modellierung von EWS-Systemen wird durch verschiedene Sensitivitätsstudien gezeigt und des Weiteren durch Vergleichssimulationen mit der semi-analytischen Software EED und durch Validierung mit gemessenen Daten bestätigt.

Den grössten Einfluss auf die Dimensionierung einer EWS-Anlage haben die Bodenoberflächentemperatur (BOT) und die Wärmeleitfähigkeit des Untergrundes. Methoden zur Bestimmung dieser zwei Einflussgrössen werden beschrieben und diskutiert.

Für die Schweiz wird eine regionale BOT-Analyse durchgeführt, die sowohl klimatische als auch geothermische Daten berücksichtigt. Dabei wird die Höhenabhängigkeit der BOT sowie die Beziehung zwischen BOT und Lufttemperatur detailliert untersucht. Die Weiterverarbeitung der erzielten Erkenntnisse erlaubt es eine BOT-Karte der Schweiz zu erstellen, die wichtige Erkenntnisse für die Beurteilung geothermischer Ressourcen sowie für die Bestimmung der regionalen BOT-Verteilung unter für Zentraleuropa typischen klimatischen Bedingungen liefert.

Der Thermische Response-Test ist eine weit verbreitete Methode zur In-situ-Bestimmung der Wärmeleitfähigkeit. Der Gültigkeitsbereich dieses Tests wird mittels FRACTure-Simulationen untersucht. Das dafür gewählte Vorgehen liefert Erkenntnisse über die nötige Testdauer, über den Einfluss von Grundwasserfliessen

und heterogener Untergrundbeschaffenheit, sowie über den Effekt unterschiedlicher Datenqualität. Die erzielten Ergebnisse zeigen, dass die meisten Response-Tests die Wärmeleitfähigkeit unterschätzen; die Abweichung kann bis zu -10 % betragen. Der Vergleich einer analytischen mit einer numerischen Auswertung verdeutlicht anhand eines realen Response-Tests die Wichtigkeit gut durchdachter, numerischer Methoden für die Interpretation solcher Tests.

Die Bestimmung der BOT und der Wärmeleitfähigkeit sind grundsätzliche geowissenschaftliche Aspekte der angewandten und der allgemeinen geothermischen Forschung. In dieser Arbeit wird anhand von zwei Sensitivitätsstudien der Einfluss dieser zwei Parameter auf die Leistung einer Einzel-Erdwärmesonde untersucht und für verschiedene Standorte in der Schweiz visualisiert. Dabei zeigt sich, dass die BOT einen grösseren Einfluss auf die Leistung haben kann als die Wärmeleitfähigkeit.

In einem letzten Schritt wird die Nachhaltigkeit von EWS-Feldern untersucht. Die Resultate (Untergrundstemperatur und EWS-Fördertemperatur) werden mit denen einer Einzelsonde derselben Länge verglichen. Es zeigt sich, dass die Systemerholung bei EWS-Feldern länger dauert als bei einer Einzelsonde. Im untersuchten Beispiel ist zudem der Sondenabstand im EWS-Feld ein kritischer Parameter; der minimale Abstand sollte nicht unter 7 m liegen. Die tieferen Fördertemperaturen im Fall des EWS-Feldes können durch zusätzliche Sondenbohrmeter kompensiert werden. Abschätzungen bezüglich zusätzlich benötigter Bohrmeter werden für bestimmte Rahmenbedingungen gegeben. Die durchgeführte Untersuchung zeigt, dass bei richtiger Dimensionierung ein EWS-Feld nachhaltig betrieben werden kann.

TABLE OF CONTENTS

NOMENCLATURE

Indices

f	fluid
s	solid
i	Control variable

Latin letters

Symbol	Unit	Description
A	[m^2]	Area
A_0	[K]	Amplitude of GST change
A_{dom}	[K]	Dominate GST amplitude
c	[J $kg^{-1}K^{-1}$]	Specific heat capacity
const		Constant
COP	[-]	Coefficient of performance
d_{pipe}		Inner pipe diameter
D	[m]	Depth of thermal insulation
E_e	[kWh]	Electrical energy consumption
E_h	[kWh]	Heating energy
g	[m s^{-2}]	Gravitational acceleration
g	[-]	ĝ-function
GST	[°C]	Ground surface temperature
GST_m	[°C]	Monthly ground surface temperature
$<GST>_a$	[°C]	Annual mean ground surface temperature
$<GST>_m$	[°C]	Monthly mean ground surface temperature
ΔGST_m	[K]	Difference of GST_m from the sinusoidal annual GST variation

h	[W m^{-2} K^{-1}]	Heat transfer coefficient
h_g	[m]	Hydraulic head
H	[m]	Active borehole depth
k	[m^2]	Permeability
K	[m^2 Pa^{-1} s^{-1}]	Hydraulic conductivity
K_g	[m s^{-1}]	Hydraulic conductivity in a groundwater layer
l	[m]	Borehole length
L	[m]	Characteristic flow length
Nu	[-]	Nusselt Number
m	[-]	Exponent
n	[-]	Number of measurements
p	[W]	Thermal power
p_e	[W]	Electrical power
p_h	[W]	Heating power
P	[Pa]	Pressure
Pe	[-]	Peclet number
Pr	[-]	Prandtl Number
ΔP	[Pa]	Pressure loss
q	[W m^{-2}]	Heat flow
q_{spez}	[W m^{-1}],	Specific heat injection/extraction rate
Q	[m^3 s^{-1}]	Volumetric flow rate
r	[m]	Radial distance
r_b	[m]	Borehole radius
R	[W m^{-2}]	Global solar radiation
Re	[-]	Reynolds Number
R_a	[K m W^{-1}]	Internal borehole resistance

R_b	[K m W^{-1}]	Borehole thermal resistance
ΔR	[W m^{-2}]	Deviation of the local solar radiation from the annual mean radiation of a region
R^2	[-]	Correlation coefficient
SAT	[°C]	Air temperature at screen height
$<SAT>_a$	[°C]	Annual mean surface air temperature
$<SAT>_m$	[°C]	Monthly mean surface air temperature
$<SAT_{mod}>_a$	[°C]	Modified annual mean SAT
SPF	[-]	Seasonal performance factor
t	[s]	Time
t_c	[s]	Lower time creation for g-function
t_s	[s]	Upper time creation for g-function
Δt	[s]	Time increment
T	[°C]	Temperature
T_0	[K]	Undisturbed GST amplitude
T_{in}	[°C]	BHE inlet temperature
T_b	[°C]	Average borehole wall temperature along a BHE
T_f	[°C]	Fluid temperature
T_{meas}	[°C]	Measured temperature
T_{red}	[°C]	Reduced temperature
T_{out}	[°C]	BHE outlet temperature
T_{sim}	[°C]	Simulated temperature
$\overline{T}$	[°C]	Average fluid temperature along a BHE
ΔT	[K]	Difference between the measured GST and the polynomial fit

$\Delta T_{b\_<GST>a}$	[K]	Difference between $<GST>_a$ map and extrapolated $<GST>_a$ from boreholes
ΔT_{out-in}	[K]	Temperature difference between BHE outlet and inlet
∇T	[K m^{-1}]	Temperature gradient
v_D	[m s^{-1}]	Darcy – velocity
v_f	[m s^{-1}]	Particle – velocity
v_{pipe}	[m s^{-1}]	Flow velocity in the pipe
V	[m^3]	Volume
z	[m]	Vertical component, Depth
Z	[m a.s.l.]	Altitude above sea level

Greek letters

Acronym	Unit	Description
α	[-]	Borehole friction factor
γ	[-]	Euler's number
Φ	[-]	Porosity
φ	[-]	Phase
κ	[m^2 s^{-1}]	Thermal diffusivity
λ	[W m^{-1}K^{-1}]	Thermal conductivity
μ	[Pa s]	Dynamic viscosity
ρ	[kg m^{-3}]	Density
υ	[m^2 s^{-1}]	Kinematic viscosity
$\omega = \frac{2 \cdot \pi}{\text{year}}$	[a^{-1}]	Frequency
ξ	[-]	Friction factor of pipe fixture

1. INTRODUCTION

1.1 GEOTHERMAL ENERGY

Energy stored in the subsurface in the form of heat represents the basis of geothermal energy. The origin of this heat has two primary sources: 1) the decay of natural radioactive isotopes, and 2) the original heat from gravitational energy released during the earth's formation. This heat is continuously streaming towards the surface by conduction, radiation and advection via mass transport. On average the temperature in the continental crust increases with depth by 30 K Km^{-1} reaching high temperatures in the earth's interior (~900 °C at the crust – mantle boundary). Principally, a large reservoir of heat is available in the subsurface.

The aim of geothermal energy usage is to utilize this reservoir. In tectonically active zones (e.g. Iceland) molten magma will heat up subsurface rocks or deep fluid circulations will transport the heat to the surface, yielding surface manifestations like fumaroles or hot water springs. Such high-enthalpy resources (>120 °C) can be used for electricity generation. At other sites with lower temperatures, the geothermal energy is often tapped using specialized technology. Depending on the temperature level, the low-enthalpy resources can be utilized for direct heating of dwellings (e.g.: utilization of aquifer systems. Cooler resources (<30 °C) are made accessible by so-called geothermal heat pump systems. Although the temperature level is relatively low here, a wide spectrum of technologies exists to supply single and multiple family houses as well as commercial buildings with heating and, more recently, cooling, and with hot water. A heat pump is connected to the geothermal resource through a variety of systems:

- Borehole heat exchangers (BHE)
- Groundwater wells ("open" systems)
- "Geostructures" (foundation piles equipped with heat exchangers)
- Tunnel water utilization
- Utilization of aquifer systems

Geothermal energy is an indigenous and environmentally friendly energy. Contrary to most other renewable energy sources, it is available everywhere, independent of

the weather conditions or time of day. There are no CO_2 emissions from operation of geothermal systems and therefore they are a valid substitute for fossil fuels.

1.2 GEOTHERMAL HEAT PUMP SYSTEM

In Switzerland, geothermal heat pump systems have found a high level of popularity for space heating purposes and deliver in total an annual geothermal energy of ~1 TWh_{th} (Kohl et al, 2003). The basic principle of geothermal heat pump systems is to extract heat from the ground at a relatively low temperature and convert it through a heat pump into a higher temperature heat source for space heating and to produce hot water. Geothermal heat pump systems consist of three different, separate circuits (see Figure 1-1):

1. Heat source
2. Heat pump
3. Heating system

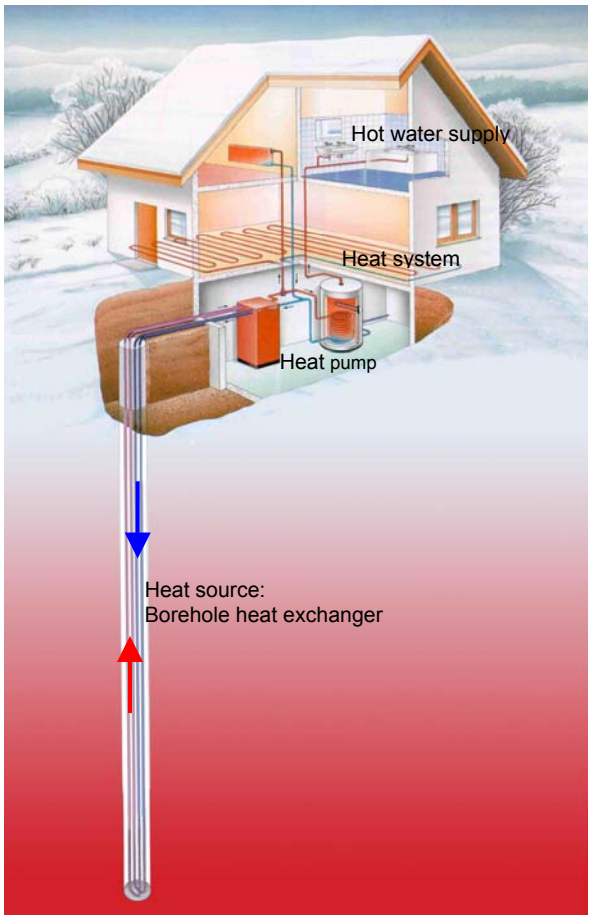

Figure 1-1: Principle of a BHE-coupled geothermal heat pump system (after Baumgartner, 1999).

Actual statistical evaluations (Kohl et al, 2003) show that in Switzerland >50 % of geothermal energy is produced by borehole heat exchangers (BHEs). BHEs consist generally of double U-tubes in backfilled boreholes. The depth of the BHE is typically 50 to over 300 m, and is determined by the amount of energy needed for heating. An environmentally-friendly heat carrier fluid (mainly Water or Ethyleneglycol – Water mixture) circulates in the tubing. It is heated by the subsurface while it flows down to the bottom of the borehole and is pumped up again. The collected heat is then delivered to the second circuit, the heat pump. The heat pump operates on the principle that heat can be transferred by a cycle of alternating vaporization and condensation. By alternately pressurizing and depressurizing a low boiling working fluid (called a refrigerant), the heat pump can absorb heat from the relatively low temperature heat extracted from the subsurface and transfer it to the warmer temperature level needed by the heating system (third circuit). Geothermal heat pumps are commonly attached to a low-temperature heating system like floor panels, partly in combination with a hot water supply. More and more these kinds of systems are used for cooling purposes in summer, by reversing the operation of the heat pump or by free cooling without a heat pump.

To run the heat pump process, electrical energy is needed. To quantify the efficiency of a geothermal heat pump over an annual time period the seasonal performance factor (SPF) is often used. It is defined as the ratio between the heating energy delivered by the heat pump, E_h, and the electric energy, E_e, supplied to heat pump, including the electrical energy consumption of auxiliary systems, such as the circulation pump:

Eq. 1-1 $$SPF = \frac{E_h}{E_e}$$

SPF-values can strongly vary with the seasonal depending temperature levels of the heat source and the heating circuit. Therefore, to compare the efficiency of different geothermal heat pumps it is more reasonable to consider the power input and output. The coefficient of performance (COP) describes the ratio of the heating power delivered by the heat pump, p_h, and the electric power supplied to heat pump, p_e,:

Eq. 1-2 $$COP = \frac{p_h}{p_e}$$

COP-values do not account for electrical consumption of auxiliary systems and therefore only rates the efficiency of the heat pump and not of the whole system.

Since BHE heating systems mainly use the temperature field below a depth of 20 m, which is not influenced by atmospheric conditions or seasonal variability, they always achieve a high efficiency even when the ambient air temperature is low. For BHE-coupled heat pumps COP-values are generally higher than 4 (WPZ-Bulletin, 2003). This fact has contributed to the high popularity of BHE systems in Switzerland. Since 1980 over 30'000 buildings have been heated by BHE systems (Rohner, 2003), corresponding to 4'700 km of drilled BHEs. The spatial distribution of the BHE systems installed by a single company until 1997 is shown in Figure 1-2. Most BHE systems are located in the Alpine Foreland, the most densely populated area. In terms of areal density (BHE / km^2), Switzerland is the world leader in this ecologically friendly technology (Rybach et al., 2000).

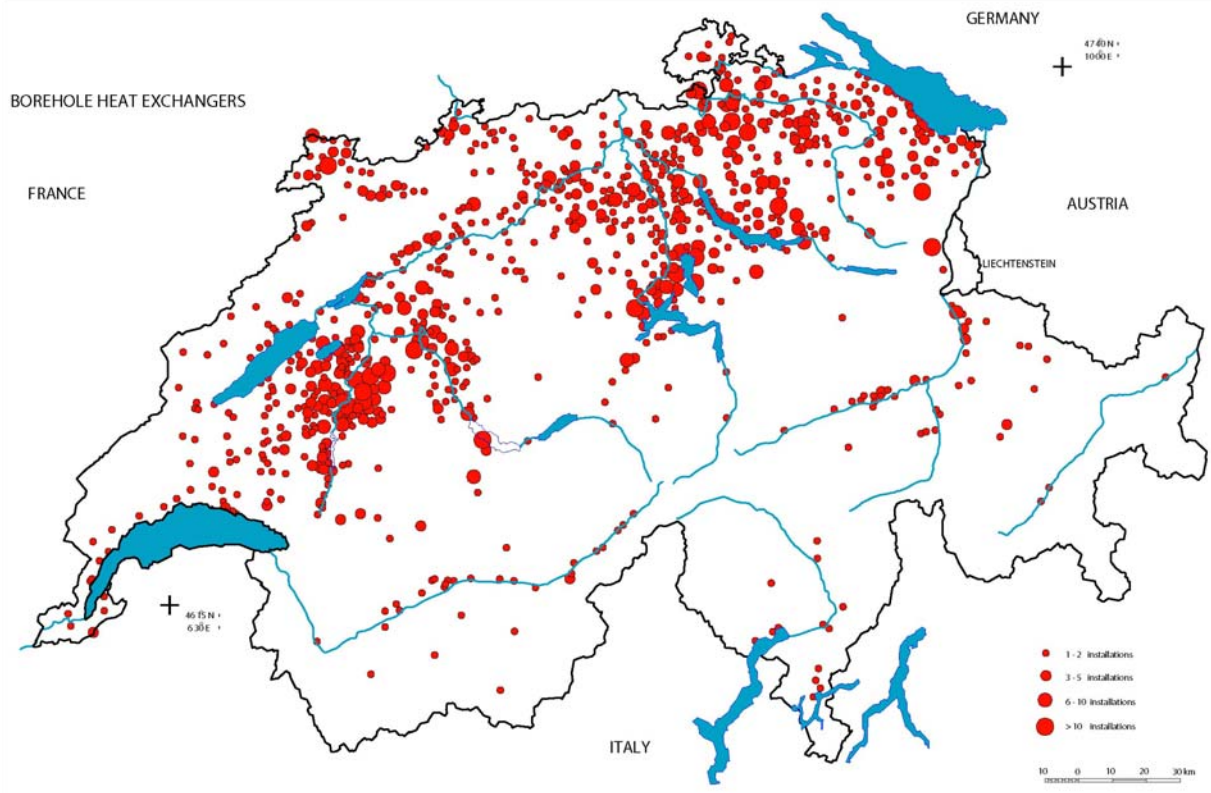

Figure 1-2: Location of BHE systems in Switzerland in 1997, delivered by a single company (adopted from Medici and Rybach, 2002).

The possible heat extraction varies from location to location depending on site-specific conditions and therefore there is no standardized BHE system. For a successful operation of BHE heating systems, a close adaptation of the three

separate circuits is essential. The heat pump and heating circuits are well-understood by heating engineers. The processes in the subsurface, however, require knowledge on complex heat transport mechanisms, and here geophysics plays a major role in linking basic scientific research to commercial applications.

1.3 PREVIOUS RESEARCH

In Europe, research on these low-enthalpy systems started in the 1980s. Theoretical thermal analysis of BHE systems prevailed in Sweden (Cleasson and Eskilson, 1988, Eskilson and Cleasson, 1988), monitoring and simulation was done in Switzerland (Gilby and Hopkirk, 1985, Hopkirk at al., 1985, Hopkirk at al., 1988, Burkart et al. 1989). In Germany, measurements of heat transport were made at a test site (Sanner, 1986). In the 1990s, experimental and theoretical investigations were conducted to elaborate a solid base for the design and for performance evaluation of BHE systems (Knoblich at al. 1993, Rybach and Hopkirk, 1995, Rybach and Eugster, 1997). Eugster and Rybach (1999) investigated the long-term behavior of single BHE systems and could demonstrate their sustainability. Furthermore, several qualitative studies have been performed to determine structural influences on the performance of BHE systems like subsurface structures, topographical elevation, and borehole spacing (Kälin and Hopkirk, 1991, Seifert et al., 1992, Rybach and Eugster, 1998). Thereby, the thermal conductivity of the subsurface was identified as one of the key parameters for the dimensioning of BHE depth. In the USA, among other topics, research was focused on thermal response tests (e.g. Morgensen, 1983, Austin, 1998) to determine in-situ thermal conductivity. Parallel research on this topic was started in Sweden, Germany and the Netherlands (Gehlin, 2002, Sanner at al., 2000, Witte, 2002).

1.4 OUTLINE OF THIS STUDY

This study evolved from within the framework of the research project "Productivity Investigation of the System Borehole Heat Exchanger with Heat Pump", financed by the "Projekt und Studienfond der Elektizitätswirtschaft" (PSEL) and the Swiss Federal Office of Energy (BFE). Until now research projects have considered either BHE or heat pump. Our project accounted for both subsystems: Borehole Heat Exchanger and Heat Pump. To achieve this broad coverage, the project was jointly

performed at the Institute of Geophysics and at the at the “Elektrizitätswerke des Kantons Zürich” (EKZ) (by order of the “Nord-Ostschweizerische Kraftwerke” NOK). It was intended that the project should benefit from the long-term running experience in geothermal research at the Institute of Geophysics acquired in numerous earlier studies. The present project involved the following 3 topics:

- Data assessment: In a first step, operational and geological data of well-documented BHE plants were collected.
- Productivity investigation: Since site factors can have a strong effect on thermal output of a BHE system (productivity), the influence of surface (ground surface temperature: GST) and geological subsurface (thermal conductivity) conditions were investigated by numerical 3D simulations. To transfer the results to any location in Switzerland, GST data had been collected and analyzed beforehand. In this context, also thermal response tests are investigated - a common method to estimate in-situ thermal conductivity for future BHE plants.
- Optimization: Financial aspects are important to promote this technology. Therefore, constructional (e.g. drilling costs) and operational (e.g. pressure losses) were analyzed and the performance (i.e. COP) of different BHE systems estimated. Accounting for the results of the performance investigation the individual BHE systems are optimized (e.g. length of heat exchanger).

This study concentrates on the first two objectives covering several geoscientific aspects ranging from GIS applications, over petrophysical measurement and determination of subsurface temperature levels to most importantly multidimensional simulation of coupled thermal transport in the subsurface. The third task is extensively reported in Signorelli and Kohl (2002) and Signorelli et al (2003). The individual topics for each chapter are discussed below:

In Chapter 2 a basic introduction into the physical background of BHE modeling is given. The complex thermal processes in and around the BHE require a simulation tool, which allows for flexible adoption to various problems. In Chapter 3, the Finite Element (FE) code FRACTure is introduced (Kohl and Hopkirk, 1995) and its capability to simulate BHE systems is shown. Additionally, the FRACTure code is

compared to the design tool “Earth Energy Designer” (EED) (Hellström and Sanner, 2000). Afterwards, FRACTure is applied to an extensive data set of an existing BHE system to quantify its short-term behavior (Chapter 4).

The impact of ground surface temperature (GST) and thermal conductivity on the performance of BHE systems is commonly known (Stadler et al., 1995). Chapter 5 is a systematic analysis of Swiss GST data in order to determine regional GST distribution for BHE installation. Chapter 6 is a theoretical and experimental study of thermal response tests to measure in-situ thermal conductivity. In Chapter 7, the influence of GST and thermal conductivity on the performance of BHE systems is analyzed for different locations in Switzerland.

Chapter 8 investigates the complex design requirements for large borehole fields, and the thermal interaction of adjacent BHEs. The general tendency of BHE installation is towards large BHE fields to supply larger buildings like multi-family houses or schools. Whereas the sustainability and renewability of single BHE systems has already been demonstrated (Rybach and Eugster, 2002), the interaction of adjacent BHEs cannot be underestimated in the design process.

Finally, Chapter 9 summarizes the main results and gives some suggestions for future work.

2. PHYSICAL BACKGROUND

The proper simulation of BHEs requires a precise understanding and corresponding treatment of the relevant thermal processes in the ground under transient conditions. The local thermal processes in and around the borehole combined with varying temperature along the borehole present particular complications. One specific problem is the successful modeling of the interaction of the advective heat flow in the pipes with the conductive thermal processes in the ground. Groundwater flow further complicates the thermal processes and advective heat transport must be considered.

This chapter is a general introduction to the physical background of thermal modeling. The description of the physical processes is based on a model assuming two different units: solids and fluids. First, the principles of groundwater hydraulics and hydraulics in pipes are described, then, a description of heat transport in a porous medium and pipe systems is discussed.

2.1 HYDRAULICS

2.1.1 GROUNDWATER HYDRAULICS

In groundwater hydrology the groundwater flow is generally described by Darcy's law. The ground water velocity is determined by the pressure difference along a flow path which is either density driven (convection) or forced by gravity such as by the relief of the groundwater table (advection). The average Darcy – velocity, v_D, is given by

Eq. 2-1 $$v_D = -K_g \cdot \nabla h_g$$

h_g is the hydraulic head, which is the equivalent of the fluid level. It is the sum of the actual external pressure and the hydrostatic fluid level and is defined as:

Eq. 2-2 $$h_g = \frac{P}{\rho_f \cdot g} + z$$

P is the pressure, ρ_f the fluid constant density, g the gravitational acceleration and z the z-direction vector.

The constant of proportionality in Eq. 2-1 is known as the hydraulic conductivity, K_g:

Eq. 2-3 $$K_g = \frac{k \cdot g \cdot \rho_f}{\mu_f}$$

k is the permeability, and μ_f the fluid dynamic viscosity.

The hydraulic conductivity value is a combination of solid and fluid related values. It can strongly vary for the same type of rocks depending on the porosity. It is generally high for gravel and low for unfractured rocks (see Table 2-1). Due to the temperature-dependence of density and viscosity the hydraulic conductivity is also temperature-dependent. In the temperature range relevant for BHE operation, the temperature dependence of density can be ignored; but the viscosity is strongly temperature-dependent. The value decreases by ~15 % when the groundwater temperature drops from 10 °C to 5 °C. Depending on the application, the temperature dependence must be considered.

Table 2-1: Typical hydraulic properties of rocks (Freeze and Cherry, 1997).

Medium	Hydraulic conductivity [m s^{-1}]	Porosity [-]
Gravel	10^{-3} – 10^{-1}	0.25 – 0.40
Silt	10^{-9} – 10^{-5}	0.35 – 0.50
Limestone	10^{-9} - 10^{-6}	0 – 0.20
Sandstone	10^{-10} – 10^{-6}	0.05 – 0.30
Fractured igneous and metamorphic rock	10^{-8} - 10^{-4}	0.05 – 0.30
Unfractured igneous and metamorphic rock	10^{-13} - 10^{-10}	0 – 0.05

The Darcy – velocity is a macroscopic concept and must be clearly distinguished from the microscopic velocity associated with the actual paths of individual water particles on their way through the grains of the rock matrix. The average particle velocity, v_f, is calculated from rock porosity, Φ:

Eq. 2-4 $$v_f = \frac{v_D}{\Phi}$$

This microscopic velocity is real, but it is probably impossible to measure its heterogeneous distribution. Therefore, for the porous thermal calculations, the Darcy–velocity concept will be used.

2.1.2 HYDRAULICS IN PIPES

When flowing through a pipe, a fluid loses pressure due to friction at the borehole wall and at the walls of the horizontal conduits. In BHE applications, the knowledge of the resulting pressure loss is necessary for sizing the circulation pump. Thereby, the volumetric flow rate is predetermined by the size of the heat pump, which is defined by the energy demand of the individual building. The volumetric flow rate itself defines then the flow velocity v_{pipe} in the pipe. Considering 1D flow in the pipe, the pressure loss, ΔP, along the BHE length, l, in a pipe of diameter, d_{pipe}, is defined by (Dubbel, 2001):

Eq. 2-5
$$\Delta P = \frac{\alpha \cdot l}{d_{pipe}} \cdot \frac{\rho \cdot v_{pipe}^2}{2} + \sum_{n=1}^{i} \xi_i \cdot \frac{\rho \cdot v_{pipe}^2}{2}$$

α is the borehole friction factor, ξ the friction factor of pipe fixtures ($\xi = 1$ for the pipe turn point fixtures at the bottom; a list of ξ for various pipe fixtures can be found in Dubbel, 2001) and i is the number of pipe fixtures.

Depending on laminar or turbulent flow regimes different formulations of the borehole friction factor, α, are applicable. The flow regime in pipes is described by the dimensionless Reynolds Number, Re:

Eq. 2-6
$$Re = \frac{v_{pipe} \cdot d_{pipe}}{\upsilon_f} = \frac{v_{pipe} \cdot d_{pipe} \cdot \rho_f}{\mu_f}$$

υ_f is the fluid kinematic viscosity and can be calculated from the fluid dynamic viscosity, μ_f, and the fluid density, ρ_f. Generally,

- Re < 2300 laminar flow
- 2300 < Re < 10^4 transient between laminar and turbulent flow
- Re > 10^4 fully developed turbulent flow

In practice, flow regimes with Re> 2300 are often treated as turbulent.

For laminar flow, α increases linearly with the flow velocity and is given by:

Eq. 2-7 $$\alpha = \frac{64}{Re} = \frac{64 \cdot \upsilon_f}{v_{pipe} \cdot d_{pipe}}$$

For turbulent flow, the Blasius approximation is often used and α is defined as (Dubbel, 2001):

Eq. 2-8 $$\alpha = 0.3164 \cdot \frac{1}{Re^{1/4}} = 0.3164 \cdot \left(\frac{\upsilon_f}{v_{pipe} \cdot d_{pipe}}\right)^{1/4}$$

For both flow regimes, α is dependent on the viscosity of the heat carrier fluid. As mentioned in the previous chapter, the viscosity is temperature-dependent. The same applies for α here.

In Signorelli et al. (2003) the pressure losses for different heat carrier fluids and BHE depths were investigated to optimize BHE length. Figure 2-1 shows the pressure loss for borehole depths ranging from 100 m to 350 m and for 32 mm and 40 mm pipe diameters, considering generally a horizontal conduit of 10 m. Two different heat carrier fluids, Water and Water/Ethyleneglycol(20%) mixture (WEM20), were investigated and the volumetric flow rate was fixed at 2100 liter h^{-1} (~$5.6 \cdot 10^{-4}$ m^3 s^{-1}). As can be expected from Eq. 2-5 the pressure loss increases linearly with BHE depth. For the 32 mm pipe diameter case, the values for WEM20 are between ~30 kPa and ~70 kPa. Reviewing the different heat carrier fluids, there is a lower pressure loss for Water than for WEM20 due to the lower viscosity for water. The difference even increases with depth, from 20 % for 200 m to 25 % for 350 m deep BHEs. However, due to the freezing point of water, it can be only used in systems where the production temperature is higher than ~5 °C, in the presented case only for BHE deeper than 200 m.

Much of the frictional pressure loss is due to the dependence of fluid flow on the pipe diameter of the pipe. Clearly, when reducing the pipe diameter by half, the flow velocity is squared for fixed flow rate. Due to the quadratic dependency of pressure loss on flow velocity in Eq. 2-5 this will lead to a 4^{th} order change in pressure loss. Figure 2-1 compares the pressure losses for 32 mm and 40 mm diameter pipes. Due to the material strength of the 32 mm pipes, their use is restricted to a borehole

depth shorter than ~150 m. The pressure loss for the 100 m and 150 m BHEs is more than double the pressure loss for 32 mm than for 40 mm diameter pipes. In installing less expensive, smaller pipes the pressure loss will increase which requires stronger circulation pumps and thus, may lead to inefficient BHE systems.

In Signorelli et al. (2003) it was shown that the higher pressure loss in deep BHEs is offset by lower runtimes and higher operational temperatures. The total electric power consumption is lower, resulting in higher COPs (see definition in Chapter 1.2) and lower operation costs. Therefore deeper BHEs can be labeled “more ecological” than shallower BHEs. Generally however, lower operational costs cannot compensate the higher installation costs of a deep BHE. It is up to the customer to balance economical and ecological aspects.

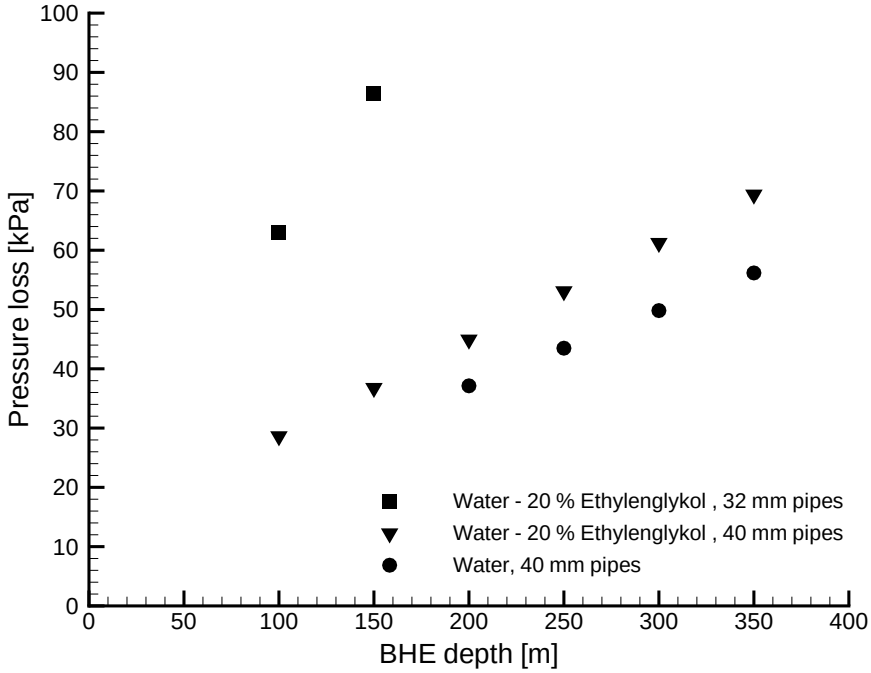

Figure 2-1: Pressure loss as a function of BHE depth and heat carrier fluid for a flow rate of 2100 liter h^{-1} (Signorelli et al., 2003). Due to the strength of the 32 mm pipes, their use is limited to borehole depths shorter than ~150 m.

2.2 HEAT TRANSPORT

In the context of BHE systems, heat is mainly transported by three mechanisms:

- **HEAT CONDUCTION**

Conductive heat transport occurs due to an energy transmission of molecular vibration. The heat is conducted through a medium in which there is a spatial

variation in temperature. Heat conduction is the dominant thermal process in solid rocks. The basic relation for conductive heat transport is Fourier's law. It states that the conductive heat flow, q_{con}, at a point is proportional to the temperature gradient, ∇T, at that point:

Eq. 2-9 $$q_{con} = -\lambda \cdot \nabla T$$

λ is the thermal conductivity.

- **HEAT ADVECTION**

Advective heat transport is associated with the motion of a medium. Although the thermal conductivity of water is low (0.6 W m^{-1} K^{-1} compared to an average value of 2.5 W m^{-1} K^{-1} for sedimentary rocks), groundwater flow can transport a large amount of thermal energy by advection through pores and fractures due to its high heat capacity (see later Table 2-2) and therefore can have a significant impact on BHE performance. Groundwater movement is mainly due to differences in pressure as described in Section 2.1. The specific thermal power p_{adv} which is provided by advective mechanisms can be calculated as follows:

Eq. 2-10 $$p_{adv} = \rho \cdot c_f \cdot v_f \cdot \nabla T$$

c_f is specific fluid heat capacity.

- **HEAT TRANSFER**

If two bodies of different temperature are in contact, heat is transferred from the warm body to the cold one. This mechanism is called heat transfer. The heat flow, q_{trans}, is proportional to the temperature difference of the two bodies:

Eq. 2-11 $$q_{trans} = h \cdot (T_1 - T_2)$$

h is the heat transfer coefficient, and T_i are the temperatures of the two bodies.

2.2.1 HEAT TRANSPORT IN THE GROUND

In principle the subsurface can be treated as two different systems: a fluid and a solid phase. The fluid phase is defined as the groundwater in pores and fractures and the solid phase represents the rock matrix. We get

for the fluid phase, f:

Eq. 2-12
$$\underbrace{\rho_f c_f \frac{\partial T_f}{\partial t}}_{\text{time variation}} = \underbrace{-\rho_f c_f v_f \nabla T_f}_{\text{advection}} \underbrace{+\nabla\cdot(\lambda_f \nabla T_f)}_{\text{conduction}} \underbrace{+h\cdot\frac{A}{V}\cdot(T_s - T_f)}_{\text{heat transfer}}$$

And for the solid phase, s:

Eq. 2-13
$$\underbrace{\rho_s c_s \frac{\partial T_s}{\partial t}}_{\text{time variation}} = \underbrace{\nabla\cdot(\lambda_s \nabla T_s)}_{\text{conduction}} \underbrace{+h\cdot\frac{A}{V}\cdot(T_f - T_s)}_{\text{heat transfer}}$$

t is the time, and A/V describes the heat transfer area A in a reference volume V.

In a water saturated subsurface, one can assume that the water temperature is equal to the rock temperature (Houpert et al., 1965) and the heat transfer term can be neglected. Thus, Eq. 2-12 and Eq. 2-13 can be reformulated as one single equation by implementing average material parameters:

Eq. 2-14
$$\overline{\rho c}\frac{\partial T}{\partial t} = -\rho_f c_f \cdot \Phi \cdot v_f \cdot \nabla T + \nabla\cdot(\bar{\lambda}\nabla T)$$

The parameters with overbars contain values from both phases. The average volumetric heat capacity value is calculated as the arithmetic mean of the two phases in a body:

Eq. 2-15
$$\overline{\rho c} = (1-\Phi)\cdot\rho_s c_s + \Phi\cdot\rho_f c_f$$

The calculation of the thermal conductivity is more complex. Generally, the geometric mean is assumed:

Eq. 2-16
$$\bar{\lambda} = \lambda_s^{(1-\Phi)}\cdot\lambda_f^{\Phi}$$

However, often an arithmetic formulation is used corresponding to Eq. 2-15 (Clauser, 1988). The thermal conductivity decreases with increasing temperature (Clauser and Huenges, 1995). In the temperature range relevant for the BHE operation (~-5 °C - ~10 °C), no significant temperature dependence occurs. Table 2-2 summarizes thermal properties of the soils and rocks.

The ratio between thermal conductivity and heat capacity can be described by the thermal diffusivity, κ:

Eq. 2-17 $$\kappa = \frac{\bar{\lambda}}{\rho c}$$

The heat advection in porous media (see Eq. 2-14) is only provided by the fluid phase. Since the advective part is weighted by porosity, the convective thermal front progresses with the Darcy – velocity (see Eq. 2-4). The ratio between the convective and the conductive transport is given by the Peclet Number:

Eq. 2-18 $$Pe = \frac{\rho_f c_f \cdot v_f \cdot L}{\bar{\lambda}}$$

L is the characteristic length (e.g. flow path).

Table 2-2: Typical thermal properties of rocks and fluids (Leu et al, 1999).

Medium	Thermal conductivity [W $m^{-1}K^{-1}$]	Heat capacity [MJ $m^{-3}K^{-1}$]
Rocks		
Gravel (saturated)	0.30 – 0.50 (1.8)	1.4 – 1.6 (2.4)
Silt	0.30- 2.30	1.5 – 2.8
Limestone	1.90 – 3.90	2.1 – 2.5
Sandstone	1.20 – 5.10	1.5 – 2.8
Fractured igneous and metamorphic rock	2.50 – 4.70	2.2
Unfractured igneous and metamorphic rock	2.50 – 4.70	2.2
Heat carrier fluid		
Water	0.6	4.18
Water – Ethylenglycol mixture (20 %)	0.51	4.05

2.2.2 HEAT TRANSPORT IN PIPE SYSTEMS

Inside the pipe, the axial heat conduction is insignificant compared with the advection of heat by the fluid due to the low thermal conductivity of the heat carrier fluids (see Table 2-2). There is only 1D heat flow inside the pipe and heat transport can be simplified by:

Eq. 2-19 $$\rho_f c_f \frac{\partial T_f}{\partial t} \cong -\rho_f c_f v_f \nabla T_f$$

During operation, the heat from the BHE surroundings is transferred into the circulation fluid by heat transport through the pipe wall. At the pipe wall, two independent thermal regimes are in contact, and the temperature for the fluid and solid phase cannot be assumed as identical. Therefore a heat transfer coefficient between the wall heat flux and the excess fluid becomes necessary. The heat transport through the pipe wall is defined as:

Eq. 2-20 $$\rho_{pipe} c_{pipe} \frac{\partial T_{pipe}}{\partial t} = \nabla \cdot (\lambda_{pipe} \nabla T_{pipe}) + h \cdot \frac{A}{V} \cdot (T_f - T_{pipe})$$

Only heat conduction in the radial direction has to be considered which can be simplified by a radial 1D process. If lateral temperature changes in the pipe fluid can be neglected (i.e. perfect lateral heat transport inside the pipe), then the heat transfer is limited to the pipe wall. The heat transfer coefficient at the interface, h, is found from the 1D Fourier equation:

Eq. 2-21 $$q = h \cdot (T_{pipe} - T_f)$$

Fluid mechanics literature commonly introduces a dimensionless measure of the heat transfer coefficient known as the Nusselt Number, Nu, the ratio of total to conductive heat transport:

Eq. 2-22 $$Nu = \frac{h \cdot d_{pipe}}{\lambda_f} = \frac{h \cdot (T_{pipe} - T_f)}{\lambda_f \cdot \frac{(T_{pipe} - T_f)}{d}} = \frac{q_{total}}{q_{cond}}$$

Depending on laminar or turbulent flow regimes (definition see Chapter 2.1.2) different formulations of the Nusselt Number are applicable. For laminar flow, the Nusselt Number can be calculated from the Prandtl Number, Pr, the Reynolds Number, Re, the dynamic viscosity of the fluid, μ_f, and the dynamic viscosity at the wall temperature, μ_w, formulated as the Sider – Tate equation (Perry and Chilton, 1984):

Eq. 2-23
$$Nu = 1.86 \cdot \left(\frac{d_{pipe} \cdot Re \cdot Pr}{l} \right)^{1/3} \cdot \left(\frac{\mu_f}{\mu_w} \right)^{0.14}$$

l is the pipe length.

In the temperature range relevant for BHE operation, the dynamic viscosity does not vary strongly for the wall temperature and the fluid temperature. The last term in Eq. 2-23 is close to 1 even for a temperature difference of 10 K.

A different correlation must be used for turbulent flow. An equation of the Dittus – Boelter form (Bennett and Myers, 1982) is often used:

Eq. 2-24
$$Nu = 0.023 \cdot Re^{4/5} \cdot Pr^{m}$$

The exponent of the Prandtl Number slightly varies depending on which correlation is used (Dittus – Boelter, Sider – Tate, …). For the Dittus – Boelter equation it is:

- m= 0.4, if $T_{pipe} > T_{fluid}$ (Fluid is heated)
- m= 0.3, if $T_{pipe} < T_{fluid}$ (Fluid is cooled)

The Prandtl Number is a material constant and defined as the ratio of the kinematic viscosity, υ, and the thermal diffusivity, κ:

Eq. 2-25
$$Pr = \frac{\upsilon_f}{\kappa} = \frac{\upsilon_f}{\lambda_f / \rho_f c_f} = \frac{\rho_f \cdot \mu_f}{\lambda_f}$$

Figure 2-2 shows a typical example for the heat transfer coefficient of a 100 m deep BHE equipped with 32 mm pipes as a function of the flow velocity. For the transient zone between laminar and turbulent ($2300 < Re < 10^4$), the Nusselt Number is linearly interpolated, although it is common in practice to treat this intermediate zone

as turbulent. Two different circulation fluids, Water and Water – 20 %Ethylenglycol mixture (WEM20), are analyzed. The heat transfer coefficient increases with the flow velocity (due to the dependence on Re) and is generally clearly higher for water than for WEM20 (due to the dependence on Pr). Using water as fluid, the flow regime is almost immediately in the transient zone between laminar and turbulent flow and beyond ~0.6 m s^{-1} flow is fully turbulent. In the case of WEM20, the flow regime is laminar for velocities <0.3 m s^{-1}. The transient zone is reached later and extends over a larger velocity range. Fully turbulent flow is only established for velocities >1.3 m s^{-1}.

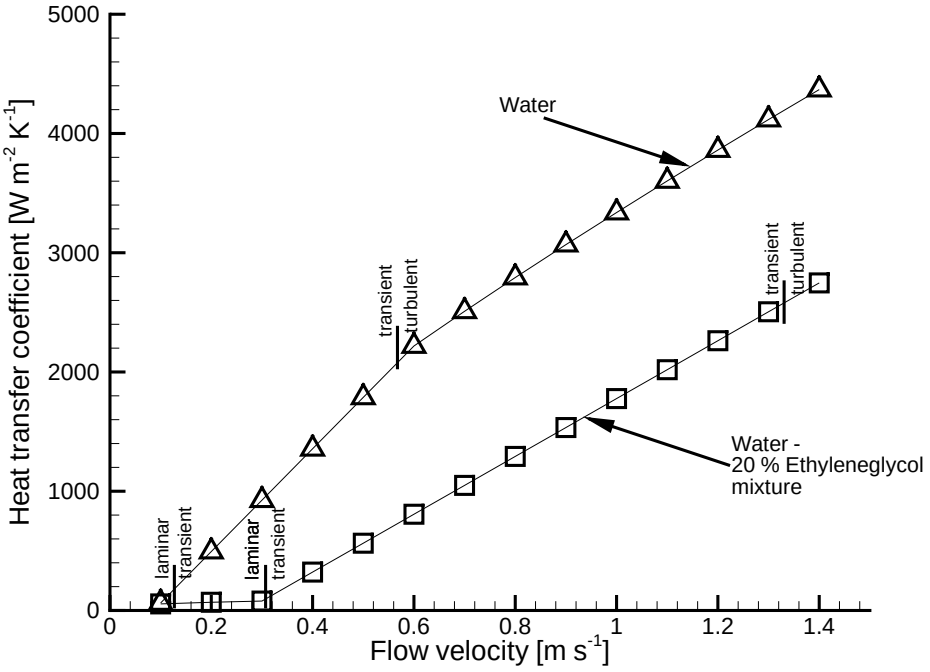

Figure 2-2: Typical example for the heat transfer coefficient of a 100 m deep BHE equipped with 32 mm pipes as a function of the flow velocity for two different circulation fluids.

The heat transfer coefficient does not directly yield information about the performance of a BHE system. In Signorelli and Kohl (2002), its influence on the thermal power production was investigated. For a 265 m deep BHE the average thermal power extraction over one year of operation was simulated for different flow velocities by the Finite Element code FRACTure (Kohl and Hopkirk, 1996). As a typical example, the results of this investigation are illustrated here for Water and WEM20. Figure 2-3 shows that the thermal power generally increases with flow

velocity. In the laminar and transient flow zone, small changes in flow velocity have a strong impact on the thermal power production. Once the turbulent flow regime is reached the power production levels off. The values vary from ~5 kW at 0.1 m s^{-1} up to ~13 kW at 1.4 m s^{-1}. Although the heat transfer coefficient is lower for WEM20, the power production is only slightly lower than for BHE plants operated with Water as a heat carrier fluid. For 0.2 m s^{-1} and 0.3 m s^{-1}, the transient flow regime is already reached for the water case, whereas for WEM20 the flow is still laminar. Here the difference is 6 %. When the intermediate zone is reached, the differences decrease and in the turbulent zone become negligible. However, due to the higher pressure loss (see Figure 2-1) more electrical power is needed for WEM20 operated BHEs to circulate the heat carrier fluid what makes a Water operated plant more efficient (Signorelli et al., 2003).

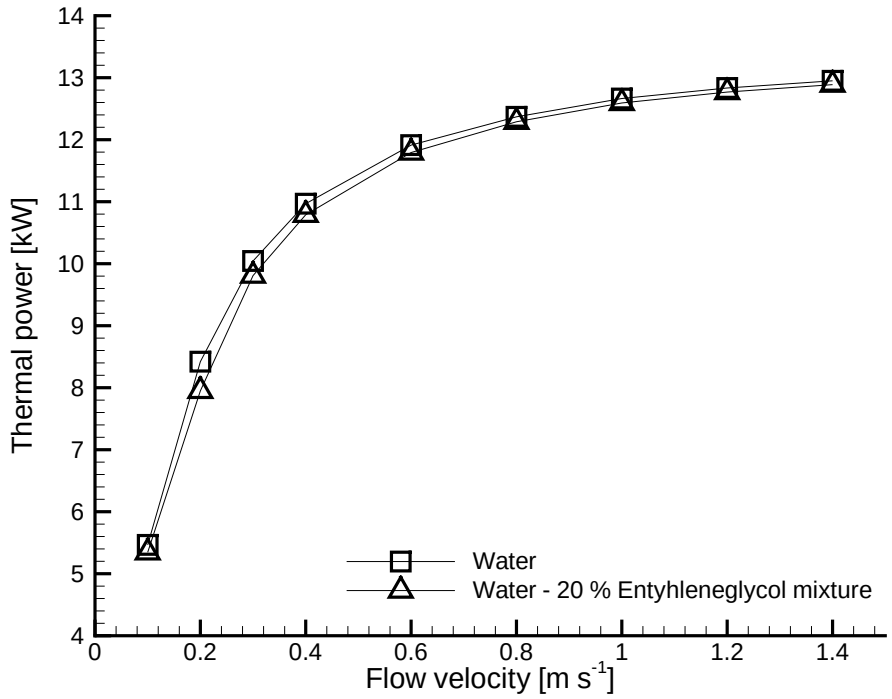

Figure 2-3: Thermal power extraction for a 265 m BHE as a function of the flow velocity (after Signorelli and Kohl, 2002).

3. BOREHOLE HEAT EXCHANGER MODELING

A variety of software applications for the design of BHEs have been developed and are currently in use around the world. Analytical models of heat transport (e.g. Hellström and Sanner, 2000) are limited to a restricted definition of material parameters and boundary conditions, but in many instances, are suitable for practical use. For complex cases, simulation can be done by numerical models of heat transport. They allow a more detailed representation of the borehole geometry and subsurface properties as well as time-varying operation conditions. The most commonly used numerical models are based on Finite Difference (FD) models (Shonder and Beck, 1999, Yavuzturk et al., 1999, Brehm, 1989). The limitation in FD models is that only rectangular spatial discretication is generally possible, whereas Finite Element (FE) models have no limitation implementing arbitrary structures. FE models are therefore particularly suitable for BHE modeling.

In the first part of this chapter the FE model FRACTure is introduced (Kohl and Hopkirk, 1995) with a focus on its applicability for BHE modeling. FRACTure was originally developed for studying the coupling of interactive mechanisms relevant to the long-term behavior of Hot Dry Rock reservoir. The code has also been successfully utilized for the simulation of BHE systems in several Diploma theses (Busslinger, 1994, Salton, 1999, Maraini, 2000, Brenni, 2000, Kurmann, 2003, Bassetti, 2003). These studies aimed at simulating deep BHE systems, demonstrating the influence of topographical and groundwater effects, and modeling of thermal response tests.

In the second part of this chapter, a comparison of FRACTure to the semi-analytical model EED is shown. The latter is the design analytical tool mostly used in Europe.

3.1 FINITE ELEMENT METHOD - FRACTURE

FRACTure offers 3D solutions to problems related to hydraulic, thermal, and elastic fields and their interactions. Hydraulic processes can be treated as laminar Darcy- or turbulent flow. For the thermal processes several mechanisms can be activated from pure diffusion to mass flow over heat generation and dispersion and absorption coefficients for solute transport. Furthermore, the impact of topography or groundwater flow on the thermal processes can be calculated.

Due to the FE approach, FRACTure has no limitation for geometrical (e.g. topography), structural (e.g. geological units) or process-related (e.g. groundwater flow) problems. A flexible mesh generation is possible. Tetrahedrons and prisms allow an accurate representation of the loop and borehole geometry of the BHEs with different dimensionality for the pipe walls (scale < 10^{-2} m) in arbitrary arrays and for any geological units (scale > 10^{2} m). The FE mesh generation is relatively easy due to the application of the mesh generation tool WinFra (Kohl, 2002) and the thermal and hydraulic properties of every element can be changed individually. Dirichlet and Neumann boundary conditions are set to simulate transport and hydraulic processes. By defining individual load-time functions, one can also control the transient behavior of selected parameters or boundary conditions, such as the variation of heat injection or of ground surface temperature. Generally, load-time functions define a linear variation between two arbitrary time steps. By defining small time intervals complex variations can be simulated. Load-time functions are flexible enough to transfer a BHE operation schedule into a numerical simulation (Kohl et al., 2002). Thus, not only theoretical but also operational investigations of the BHE systems are possible.

Since the heat conduction in the pipe systems is unimportant compared with the advection of the heat by the fluid (see Chapter 2.2.2), Peclet Numbers, Pe, in pipe systems are extremely high and for high flow velocities oscillations occur in numerical modeling. The rule of thumb for stable solutions using FE models is Pe<10. Therefore, advective thermal transports in pipe-like structures as in BHE are difficult to implement in 3D. A special feature of this code is the combination of lower and higher dimensional elements. Experience has demonstrated that high accuracy and stability is reached when fluid flow in the BHE pipes are calculated by lower dimensioned 1D tube elements, which are surrounded by 3D matrix elements. Special intermediate elements ensure that no temperature variation is encountered in the pipe perpendicular to the flow direction (see Chapter 2.2.2). The heat transfer from the surroundings through pipe walls into the circulating fluid is considered as a thermal resistance defined by the fluid velocity dependent thermal transfer coefficient (see Chapter 2.2.2).

Both steady state and transient state solutions of the FE mesh are possible. An iterative Preconditioned Conjugate Gradient (PCG) solver is used in FRACTure. A

more detailed description of FRACTure modeling can be found in the user manual (Kohl, 2002).

3.2 FE MODEL SETUP

The following section presents an overview of how BHE operations are simulated using FRACTure.

3.2.1 DEFINITION OF STANDARD MODEL PARAMETERS AND BOUNDARY CONDITIONS

The necessary model parameters and boundary conditions will be listed here. In this section the standard model conditions, which will be used for the following investigations, will be defined. For that, a 100 m deep BHE, equipped by four 32 mm polyethylene pipes ("double U-pipe type") grouted at the periphery of the 115 mm borehole is assumed. For the grouting material values for standard bentonite mixture are used. The BHE location is assumed to agree with the conditions at the site of the Swiss Meteorological Service, Zurich/Switzerland. The site represents average conditions for the Alpine Foreland, the most densely populated area in Switzerland. The elevation is 556 m.a.s.l. and the mean annual ground surface temperature is 11.1 °C with annual variations between + 9.0 K and -9.5 K (see later Figure 5-2). The geothermal heat flow is assumed to be 80 mW m^{-2}. From neighboring boreholes (Signorelli and Kohl, 2002) the geology could be estimated. The geologic profile in the top 100 m comprises Quarternary moraine (0 – 14 m) covering an alternating sequence of Tertiary „Molasse" marls (73 %), marly sandstones (14 %) and clean sandstones (13 %). From the software SwEWS (Leu et al, 1999), the average thermal conductivity (2.44 W m^{-1} K^{-1}) and heat capacity (2.51 10^6 J m^{-3} K^{-1}) are estimated. Under the given geological setting, the thermal power of the single BHE is assumed to be 5 kW (q_{spez}= 50 W per meter of specific heat extraction rate) corresponding to the Guideline VDI 4640 (2001). The flow velocity in the pipes, v_{pipe}, can be calculated for given thermal power, p, and the difference between the BHE outlet and inlet temperature, $\Delta T_{out\text{-}in}$, by:

Eq. 3-1
$$v_{pipe} = \frac{Q}{A} = \frac{p}{\rho_f c_f \cdot \Delta T_{out\text{-}in} \cdot A}$$

Q defines the volumetric flow rate and A the cross sectional area of the flow channel in the pipe.

Considering a temperature difference between the outlet and inlet fluid temperature of ΔT_{out-in}= 3 K (general customary design figure) and water with 20 % Ethylenglycol (WEM20) as heat carrier fluid, the flow velocity inside one tube circuit is 0.38 ms^{-1}. To simulate time-varying thermal heat extraction in FRACTure, the difference ΔT_{out-in} would be changed by defining a load-time function.

All model parameters are listed in Table 3-1. This model setup is assumed as the standard model setup for the following sensitivity studies in this chapter as well as in the Chapters 7 and 8.

Table 3-1: BHE design, material properties, and boundary conditions.

BHE design	Depth= 100 m Pipe radius= 32 mm (inner), 26.2 mm (outer) Borehole diameter = 115 mm		
Material properties		Thermal conductivity [W m^{-1} K^{-1}]	Heat capacity [MJ m^{-3} K^{-1}]
	Rock matrix	2.46	2.51
	Pipe	0.42	1.62
	Grouting	0.81	2.00
	Heat carrier fluid (Water - Ethyleneglycol mixture 20 %)	0.51	4.05
Boundary conditions	Constant basal heat flow		80 mW m^{-2}
	Constant ground surface temperature		$<GST>_a$= 11.1 °C
	Thermal power assumed		p= 5 kW
	Temperature difference BHE outlet / inlet		ΔT_{out-in}= 3 K
	Flow velocity in the pipe		v_p= 0.38 m s^{-1}

3.2.2 MESH GENERATION

An initial FE mesh is generated according to the model conditions in Table 3-1. Figure 3-1 shows the implementation of this borehole geometry with four tubes grouted at the periphery of the borehole. The FE mesh generation is performed by the interactive, semi-automated WinFra program (Kohl, 2002). It can be linked to common CAD programs, which allows the easy generating of technical and

geological structures. In WinFra the element properties and boundary conditions are defined and the input-file for the FRACTure simulations is generated. The general procedure is to design the FE mesh with different numbers of horizontal layers. First a coarse horizontal 2D section through the BHE is created which is then duplicated according to the depth extent of the BHE system in question. The nodal spacing is fine in the center around the borehole where the largest temperature gradients are expected. In the vertical direction the FE mesh is discretizied generally in 20 m steps with refinements at the top near the surface (1 m) and at the bottom of the borehole (<0.1 m) to reduce numerical instabilities (Bassetti, 2003).

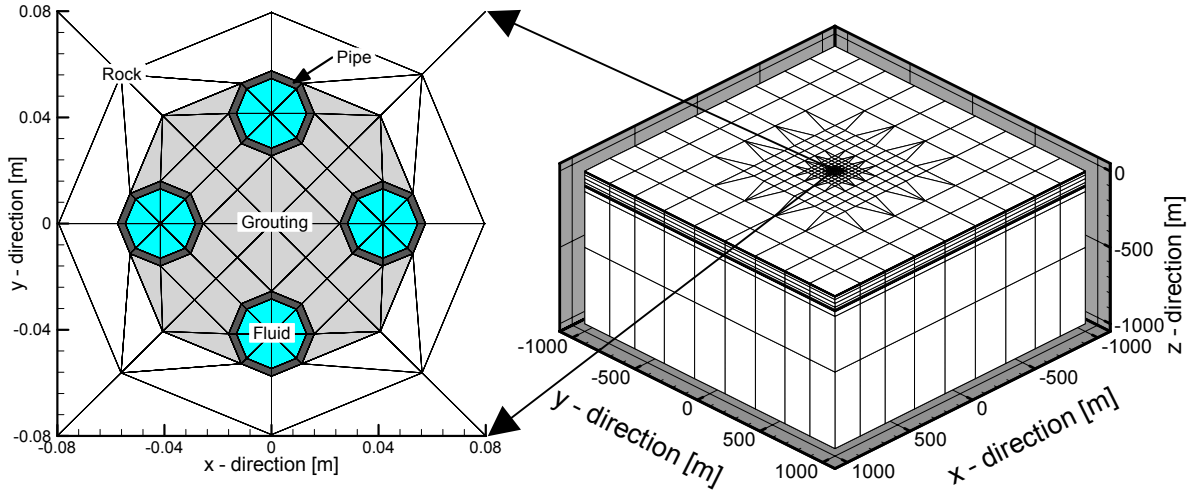

a) b)

Figure 3-1: Initial rough discretization FE mesh: a) plane view of the borehole interior, b) complete model volume 2 x 2 x 1 km.

For the modeling of BHE operation, either Neumann (flux through an area) or Dirichlet (potential at a node) boundary conditions must be defined as listed in Table 3-2. For the thermal processes, boundary conditions must be set for ground surface temperature, geothermal heat flow and the fluid temperature at the BHE inlet. Hydraulic boundary conditions are the flow rate and the hydraulic potential at the BHE outlet (= 0 m, allowing fluid up-flow). At the lateral sides, no-flow boundaries are assumed. To avoid boundary effects, the bottom and side boundaries must be at some distance from the BHE in the center of the FE mesh (see also Chapter 3.2.5). The initial mesh shown in Figure 3-1 is constructed from 26 horizontal layers, based on the layer spacing suggested by Bassetti (2003), and consists of ~17'000 nodes. A model size of 2000 x 2000 x 1000 m is assumed which is absolutely sufficient (see Chapter 3.2.5). The following test runs are all based on this initial FE mesh.

Table 3-2: Boundary conditions to define for the simulation of a BHE.

For the thermal processes	Type of boundary condition
Basal heat flow	Neumann
Ground surface temperature	Dirichlet
Fluid temperature at the BHE inlet (either constant or dependent on the BHE outlet temperature)	Dirichlet

For the hydraulic processes	Type of boundary condition
Flow velocity in the pipe system	Neumann
Zero hydraulic potential at the BHE outlet (allowing the fluid up flow)	Dirichlet

3.2.3 DISCRETIZATION IN TIME

In the transient mode, FRACTure performs calculations only at defined and discrete time intervals. These time points are defined by time increments (Δt) of arbitrary lengths, which can be changed at any time. Small increments lead to a high temporal resolution, but are CPU time-consuming. Large time steps only inaccurately resolve the temperature evolution during BHE operation. An ideal sequence of different time increments has to be estimated with small time steps for the simulation of operation cycles and large steps for the long-time behavior. Therefore, calculations are performed for Δt= 1 sec, 1 min, 10 min and 1 hr with the FE mesh in Figure 3-1 and the model parameters in Table 3-1. Initially an undisturbed steady-state temperature field is assumed and then the heat extraction starts for a period of 24 hrs. The model runs require different CPU-time from 1 min to 3 hrs on a 2 GHz PC.

For the different model runs, the modeled production temperatures (BHE outlet temperature) during the first 3 hours are illustrated in Figure 3-2. The short-term behavior will be discussed for Δt= 1 sec. Initially, after the start of operation, production temperature increases due to the initial warm, stagnant water column in the pipe and decreases after ~10 min. This peak is only relevant for the short-term behavior. It is not relevant for the long-time performance consideration, since the temperature drops quickly to lower values once the water column has been changed. This peak occurs during every further operation cycle, whereas the shape is

dependent on the recovery duration: The shorter the recovery, the lower the peak. From Figure 3-2 it is recognized that long time increments resolve the temperature evolution in the first hour worse. However, in the long-term behavior the differently discretized model runs show negligible differences (~0.2 K after 24 hrs of operation). To exactly simulate the temperature evolution the combination of time steps in Table 3-3 has proved to be optimal during operation period (Signorelli et al, 2003) and will be used for all following investigations. During the shutdown period (no operation), time steps of 1 hour are sufficient which can be progressively increased to weeks and months depending on the shutdown duration.

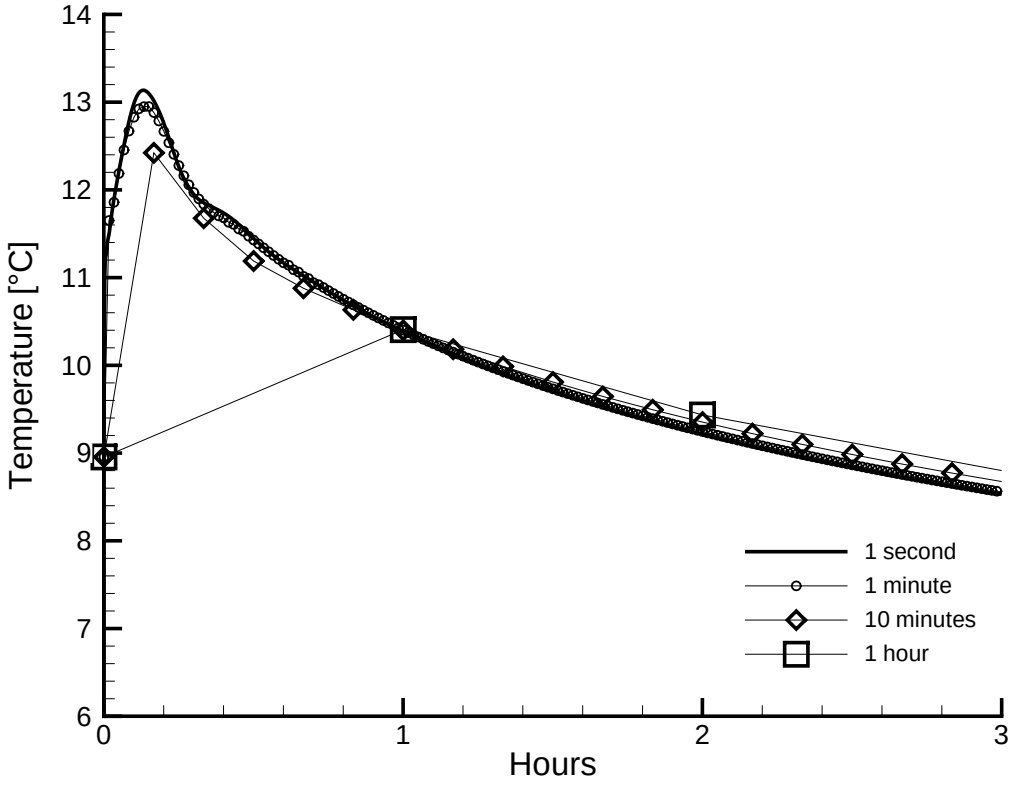

Figure 3-2: Temperature simulation for different discretizations in time.

Table 3-3: Discretization in time for the operation phase.

Operation phase	Time step lengths
0 – 1 minute	1 second
1 – 30 minutes	1 minute
30 minutes – 1 hour	10 minutes
1 - 10 hours	1 hour
After 10 hour	10 hours

3.2.4 SPATIAL DISCRETIZATION

Generally, finer spatial discretization results in higher accuracy, but is more time-consuming. To define the necessary horizontal discretization the mesh size of the initial mesh in Figure 3-1 is reduced in two steps, whereas in every step the meshes are subdivided into new elements. Model runs are performed for:

- M_1: coarse spatial discretization (initial mesh, ~17'000 nodes)
- M_2: fine spatial discretization (~70'000 nodes)
- M_3: very fine spatial discretization (~360'000 nodes)

Based on the parameters in Table 3-1, simulations were performed again for a constant 24 hours operation time. The time steps for the numerical calculations are those in Table 3-3.

Figure 3-3 illustrates the evolution of the production temperature during the first hour. In the short-term behavior the highest production temperatures do not occur at the same time. The temperature peak for the coarse model run M_1 is slightly phase-delayed compared to the refined model runs. Due to the refinement the peak time stabilizes and for model run M_2 and M_3 occurs nearly at the same time (6.6 and 7.2 min, respectively). Furthermore, Figure 3-3 illustrates that the highest temperature does not arise after the half circulation time (time the fluid needs to rise from the bottom of the BHE to the top, 4.4 min), but later at 6.6 min. This is due to three-dimensional effects: The hottest water from the BHE bottom is cooled by the borehole wall on its way up and as a consequence the highest production temperature at the outlet originates not from the absolute bottom of the BHE, but from the downflow side of the pipe. The temperature peak (Figure 3-3) is slightly

delayed from the arrival of the bottom water at the production outlet. The mesh size not only has an influence on the short-, but also on the long-term behavior. Between M_2 and M_3, the difference after 1 day is less than 0.2 K, but between M_1 and M_3 the difference increases with the operation duration up to 0.9 K.

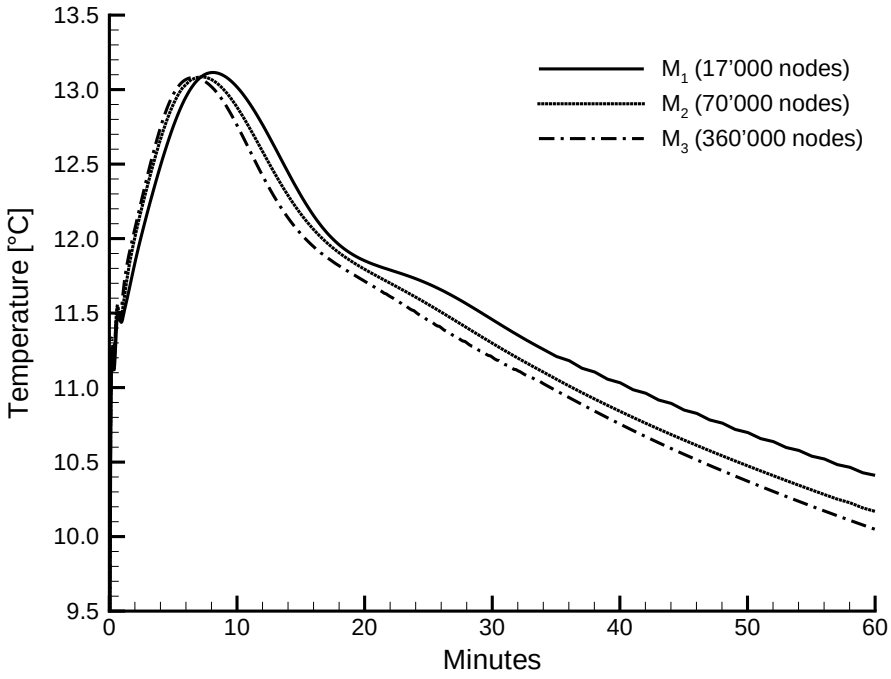

Figure 3-3: Temperature simulation for different horizontal spatial discretization model runs.

Figure 3-4 compares the temperature profiles along the BHE in 0.1 m and in 1 m distance after 1 day. In 0.1 cm M_1 shows ~0.4 K higher temperatures than the other model runs. But, after ~1 m, the difference in subsurface temperature between the model runs reduces and is already less than 0.2 K (It may be noted that a temperature difference of this size is not relevant for practical applications). Thus, the borehole and its nearest surroundings (<1 m) must be finely discretized, but outside the borehole the mesh size can be rapidly increased. Therefore, a new FE mesh is generated where the fine-scale BHE discretization of M_3 is taken and the surrounding has a larger scale. This FE mesh is shown in Figure 3-5. For the following simulations and for the investigation in Chapters 7 and 8, this fine FE mesh is used.

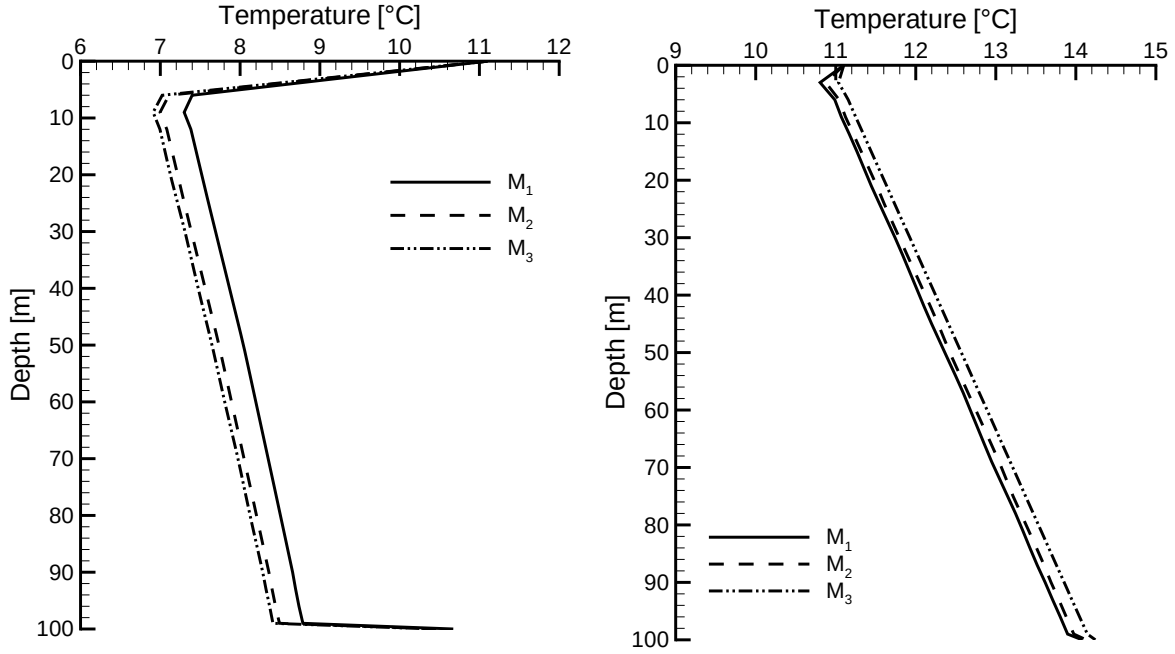

Figure 3-4: Temperature profile in the ground in a) 10 cm and b) 1 m distance from the BHE after 24 hrs of operation for different horizontal spatial discretization models M_1, M_2 and M_3 (see text). The difference between the model runs decreases with increasing distance from the BHE.

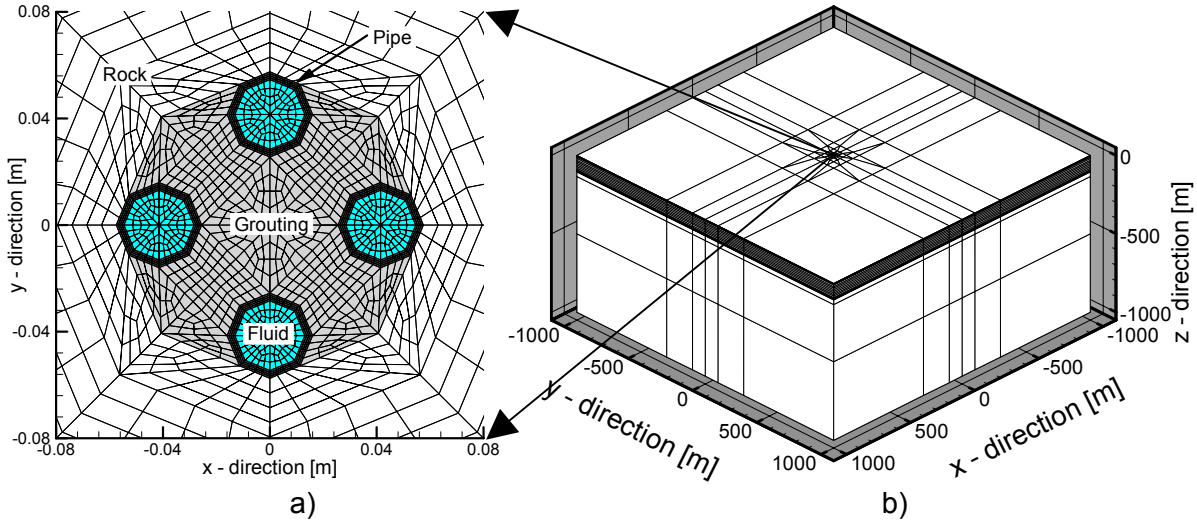

Figure 3-5: Standard FE mesh: a) very fine discretized borehole interior, b) coarse spatial discretization of the far field.

3.2.5 MESH EXTENT

Kurmann (2003) investigated the minimum block size of the FE mesh under steady-state conditions. By evaluating the influence of borders, he defined the minimum distance of the side and bottom boundary from the BHE for different BHE systems ranging from 50 m to 350 m depth. The inlet temperature was fixed at 1 °C and from the difference to the produced fluid temperature, the extracted thermal power was calculated. The criterion for the minimum permissible model extent was defined so that the thermal power must at least be 99.9 % of the power for a large reference model. This model was assumed to have a block size of 3’000 m horizontal (1’500 m distance from the BHE in the middle of the mesh) and 10’000 m vertical extent. For every borehole depth the site boundary was shortened, whereas the depth extent was fixed at 10’000 m, until the difference in thermal power fell short of the criterion. Later, the depth extend was estimated by the same procedure. The results are illustrated in Figure 3-6 and depend upon the individual boundaries. Both the required vertical and horizontal model extent can be approximated by a linear relation. The figure shows that the model is more sensitive to the distance of the lateral boundaries from the BHE where no-flow boundary conditions are assumed than to the depth of the bottom boundary where a constant heat flow is applied. From Figure 3-6 it is recognized that the 2000 x 2000 x 1000 m block size as assumed in Figure 3-5 is not necessary. For a 100 m BHE system, the block size of 750 x 750 x 300 m would be sufficient.

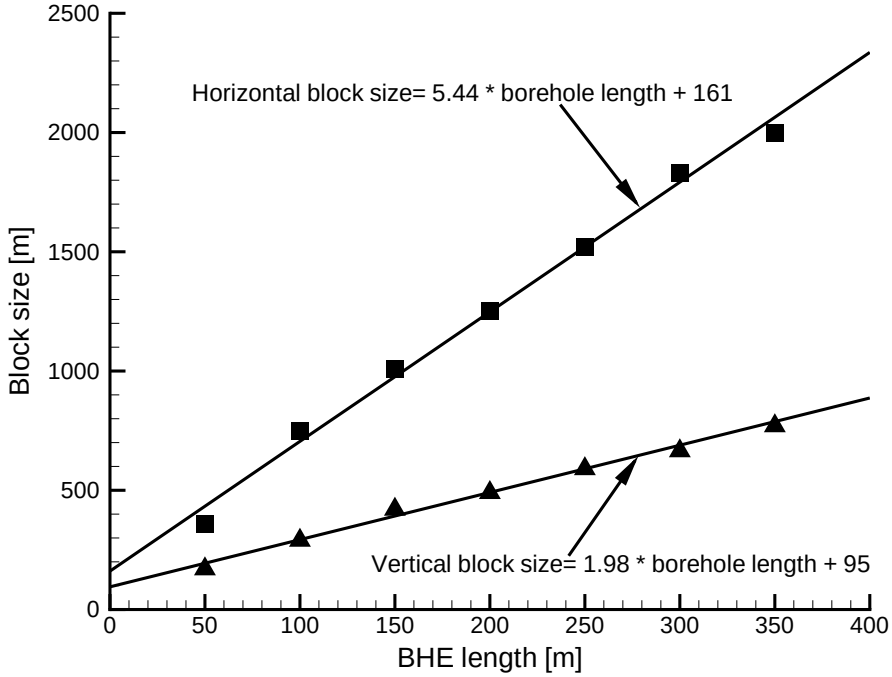

Figure 3-6: Linear relation between the BHE depth and the minimal vertical and horizontal block size needed to avoid boundary effects (after Kurmann, 2003).

3.2.6 THERMAL POWER MODELING PROCEDURE

In FRACTure a given extracted thermal power, q, is simulated by subtracting a constant temperature value, $\Delta T_{out\text{-}in}$, from the fluid outlet temperature, T_{out}, and considering the difference as the new inlet temperature, T_{in}:

Eq. 3-2
$$T_{in}^{i+1} = T_{out}^{i} - \Delta T_{out-in} = T_{out}^{i} - \frac{q^{i}}{\rho \cdot c_p \cdot Q}$$

i denotes the time step.

Using such an explicit simulation mode, the temperature value for the inlet is defined by the last time step and the extracted power load calculated from outlet and inlet temperature at t_i does not equal the power which is applied. Thus, an implicit treatment must be considered to define the inlet temperature from the outlet temperature and the actual time step. Solving implicitly, however, is time consuming (> 6 times explicit) and is not always necessary for certain conditions.

Figure 3-7 shows the comparisons of the simulated outlet temperature evolution over 24 hrs of constant operation for the explicit and implicit treatment. The used

treatment for the simulation of the inlet temperature conditions has a minimal influence on the temperature calculations. The difference between the two approaches is maximally 0.2 K and becomes lower during periods of same time step length. After 24 hrs it is less than 0.1 K. However, it has an effect on the actual thermal power value. In the implicit case, the thermal power is exactly 5 kW as defined for our standard model setup in Chapter 3.2.1, but not in the explicit case. Figure 3-8 shows the extracted thermal power in the explicit model runs calculated at every time step relatively to the heat extraction in the implicit case. On average over the 24 hrs simulation period, the extracted thermal power in the explicit case is only 1.4 % lower than in the case with implicit treatment, but during shorter periods, differences up to 15 % occur. The variations in the differences are related to the change in time step length. If the time increments are increased (see Table 3-3), the difference in thermal power increases and progressively approaches zero again afterwards during the following period of constant time step length.

We can conclude that applying an explicit or implicit treatment has no significant influence on the simulation of the fluid temperature evolution. However, the implicit treatment can be important in cases where exact modeling of heat extraction or injection is essential, as for the investigation of thermal response tests in Chapter 6.

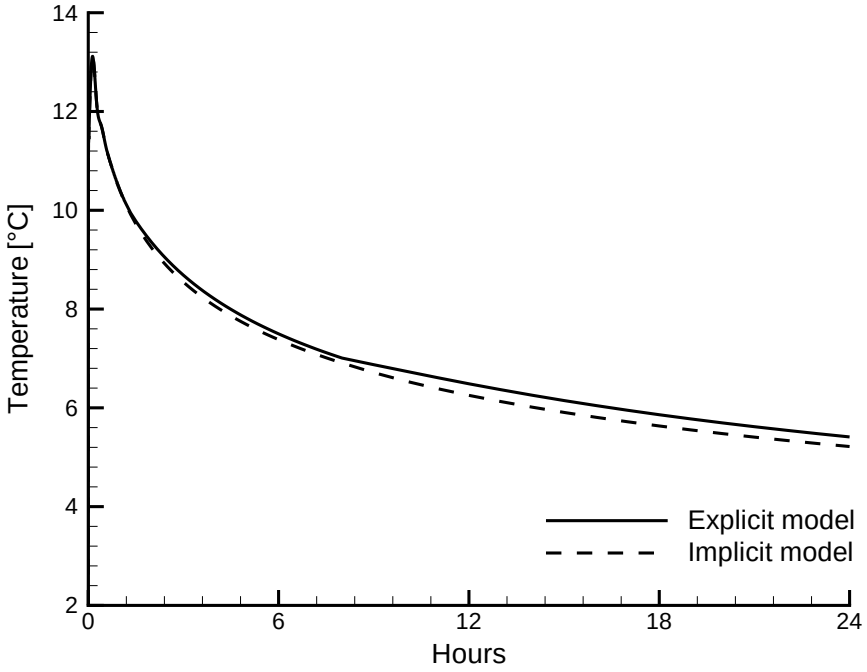

Figure 3-7: Comparison of the outlet temperature evolution with implicit and explicit simulation of the thermal power.

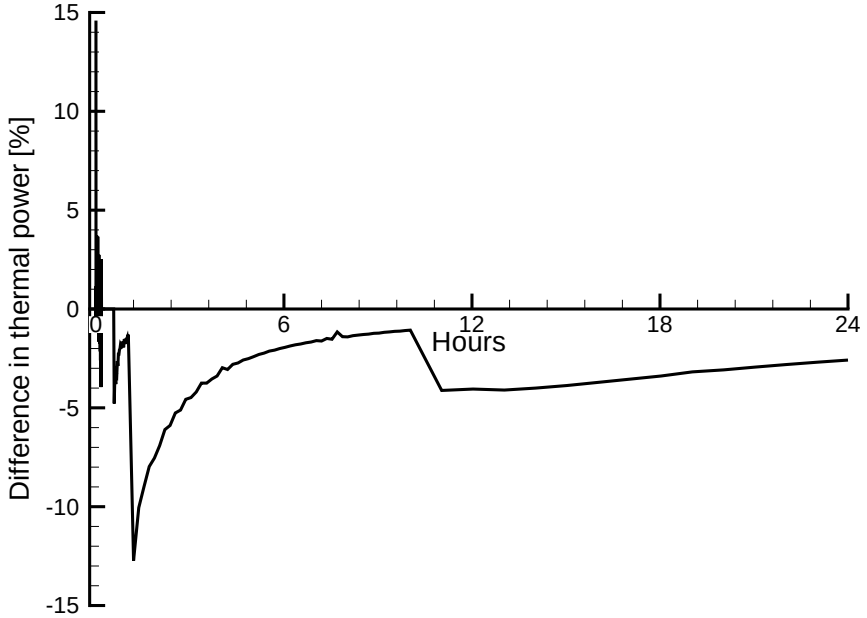

Figure 3-8: Comparison of the thermal power at time t_i in the case of explicit simulation of the thermal power relatively to the thermal power applied.

3.2.7 ENERGY LOAD PROFILE

In the following, the system behavior of a BHE in heating mode is investigated. For this purpose, we are interested in the production BHE outlet temperature, which must not fall below a certain acceptable value (5 °C for the heat carrier fluid Water and -5 °C for Water - Ethyleneglycol mixture), and in the evolution of the subsurface temperature, which defines the energy reservoir and the long-term sustainability of the BHE system. The outlet temperature as well as the cooling of the subsurface depends on the load profile applied. FRACTure allows any load profile consisting of an arbitrary sequence of operation and recovery cycles. But, the CPU – time for the simulation required is dependent on the number of operation/recovery cycles, and prudent modeling should consider a regular operation scheme. Furthermore, the load profile is generally not known in advance. Therefore, it becomes necessary to investigate the influence of the energy load distribution on the outlet temperature and on the subsurface cooling.

Kohl et al. (2002) studied the behavior of the production temperature for different operation and recovery cycles for one month. In their application the inlet temperature was fixed at a constant value. It could be demonstrated that for identical flow rates and for identical total operation time the outlet temperature at the end of an operational period is identical no matter how the operation and recovery cycles are distributed. For general design purposes, not the inlet temperature but the extracted thermal power is fixed. Therefore, the transient behavior of the BHE outlet temperature and of the subsurface will now be investigated for different load profiles with identical heat extraction. The goal is to find a load time profile, which provides on one hand a realistic temperature simulation, and on the other hand, only needs a short CPU – time.

For this investigation, a total runtime of 1'800 hrs per year is applied. This corresponds to the average annual operation time in the Swiss Alpine Foreland. The runtime is subdivided into various runtimes per months. The proportion has been set accordingly to the number of days below the threshold for the onset of the heating (air temperature of 16°C). The values in Table 3-4 are estimated on the basis of the long-term measurements at the Swiss Meteorological Service in Zurich (Meteotest, 1997). Assuming the thermal heat extraction rate from Table 3-1, different energy

loads per month result. Table 3-4 lists the runtime and energy load distribution over the annual cycles.

The monthly energy demand from Table 3-4 is simulated considering three differently loaded model cases:

- **Single load model:** Constant operation at the beginning of the month is assumed, followed by a recovery phase during the rest of the month.

  $\Rightarrow \Delta T_{out\text{-}in}$ and v_p are taken from Table 3-1 and the operation time from Table 3-4.

- **Multiple load model (so-called peak load):** Constant operation at the beginning of the day is assumed, followed by a recovery phase during the rest of the day. This is normally the maximum output of the heat pump per day and represents the minimum temperature, which can occur.

  $\Rightarrow \Delta T_{out\text{-}in}$ and v_p are taken from Table 3-1, the monthly operation time from Table 3-4 is divided in daily operation times.

- **Distributed load model (so-called base load):** The load is homogenously distributed over a month. From the annual heating, the individual monthly based load is estimated:

  $\Rightarrow v_p$ is taken from Table 3-1, $\Delta T_{out\text{-}in}$ is adjusted so that the energy load in Table 3-4 is supplied during constant operation.

For real operation modes, the temperature profile will lie between the “multiple load model” and the “distributed load model”.

Table 3-4: Runtimes and energy loads per month subdivision according to the climatic data at the site of the Swiss Meteorological Service (20 years average; Meteotest, 1997).

Month	Runtime per month [h]	Energy load per month [kW h]	Percentage [%]
September	60	300	3.3
October	124	620	6.9
November	240	1’200	13.3
December	296	1’480	16.4
January	308	1’540	17.1
February	252	1’260	14.0
March	186	930	10.3
April	119	595	6.6
May	93	465	5.2
June	60	300	3.3
July	31	155	1.7
August	31	155	1.7
Total	1’800	9’000	100

The simulation starts in September which is generally the beginning of the heating season. Figure 3-9 shows the simulated BHE outlet temperature during the first year of operation and the September of the second year. For readability, the production temperatures for the “multiple load profile” are only plotted for September, February and August. The general behavior of the fluid temperature will be discussed for “single load profile”. After the start of the operation, the production temperature increases first (see Chapter 3.2.3) due to the warm, stagnant water in the pipe and decreases afterwards. When the recovery period starts the temperature immediately rises to a fixed value, which corresponds to the boundary condition value of the annual ground surface temperature (see Table 3-1). This period is not interesting for performance considerations, but only for the recovery of the ground. Thereafter, operation will start again. The production temperature during every operation cycle depends on the runtime before the new production and on the specific runtime length. The same behavior shows the “multiple load profile” on a daily cycle. For the homogenously “distributed load profile”, there is no recovery phase and the variation in temperature is due to changes in the heat extraction rate. The “single load profile”

with the whole heat extraction at the beginning of every month is an unrealistic load profile; BHE systems will never run constantly over such a long time and the simulated production temperature is therefore much too low (and BHE dimensioning would be too conservative). In contrast, temperatures for the “distributed load profile” are too optimistic. A good approximation of the real minimum temperature is provided by the “multiple load profile”, since it simulates the maximum heat load, which must be expected for one day.

Figure 3-9 shows that contrary to the investigation of Kohl et al. (2002) where the BHE inlet temperature was fixed the simulated outlet temperature is highly dependent on the load profile when the extracted thermal power is kept fixed. The estimation of the effective produced temperature is difficult. However, if the changes in production temperature for individual heating seasons are compared at the end of September (see dT in Figure 3-9), one recognizes that the relative temperature drop from one year to the following is identical (~0.6 K) for all load profiles. Even if the absolute value is not known, the real drop of production temperature can be simulated. Therefore, any load profile can be applied when the evolution of the produced temperature is compared from one year to the other.

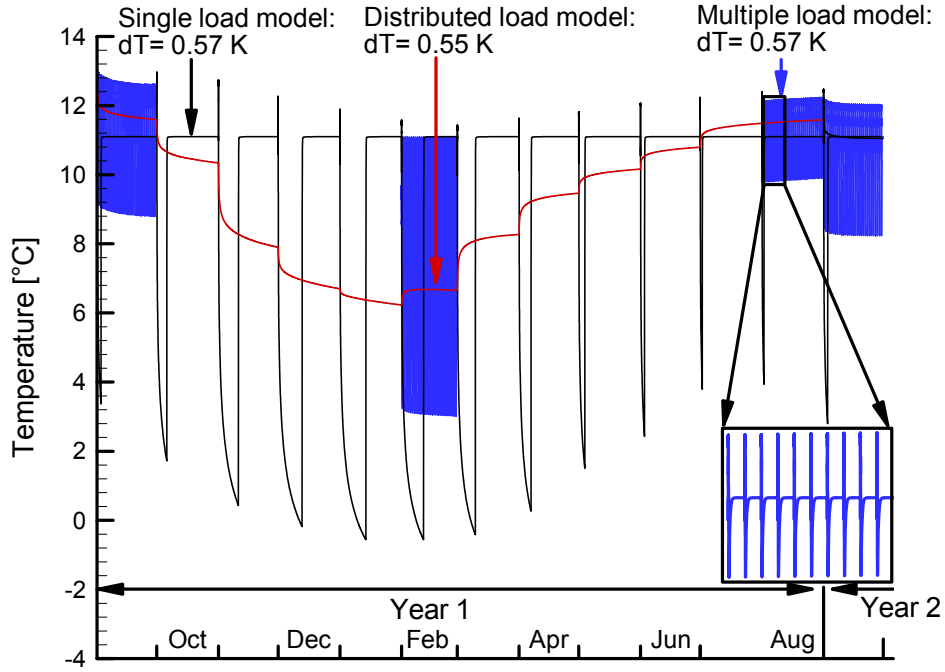

Figure 3-9: Production temperature as function of the load profile during the first operational year. For readability, the production temperatures for the “multiple load profile” are only plotted for September, February and August. dT indicates the fluid temperature drop between September of the first and second year for the individual load profiles.

Figure 3-10 illustrates the influence of the different load profiles on the simulation of the ground temperature evolution at 50 m depth in a distance of 0.1 cm for February (strong heating) and August (nearly no heating) in the first year of operation. In the “single load case” the cooling of the subsurface is strong during operation and subsequent recovery (+/-10 K). For the “multiple load profile”, the changes are less prominent. The “distributed load profile” shows a constant subsurface temperature per month with generally the lowest temperature at the end of the month of all load profiles. In February the differences between the individual load profiles are rather large (>5 K), whereas at the end of August, is only ~0.3 K (see Figure 3-10). Since for real operation, the load profile lies between the “multiple load profile” and the “distributed load profile”, the subsurface cooling will also lie in-between these two cases. Figure 3-10 shows that at the end of August the temperature is nearly identical no matter which load profile is applied. Therefore, any load profile can be taken for the investigation when the reference point is chosen at 31 August, the time right before the new heating season starts. This also corresponds to the procedure of Rybach and Eugster (2002). The temperature perturbation at the end of August is a function of the energy that has been extracted from the subsurface and the recovery period during the summer season. It defines the amount of energy that is available for the coming heating season.

The investigation shows that the distribution of the load does not affect the simulation of the produced temperature and subsurface cooling significantly, when the right time points are compared. However, the production fluid temperature can only be analyzed as the relative change.

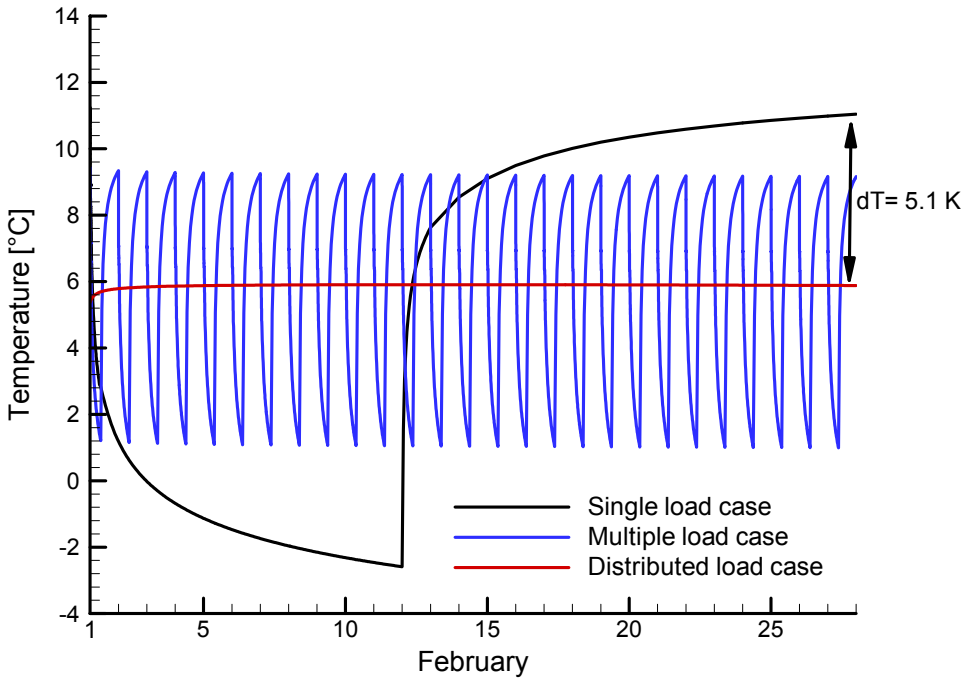

a)

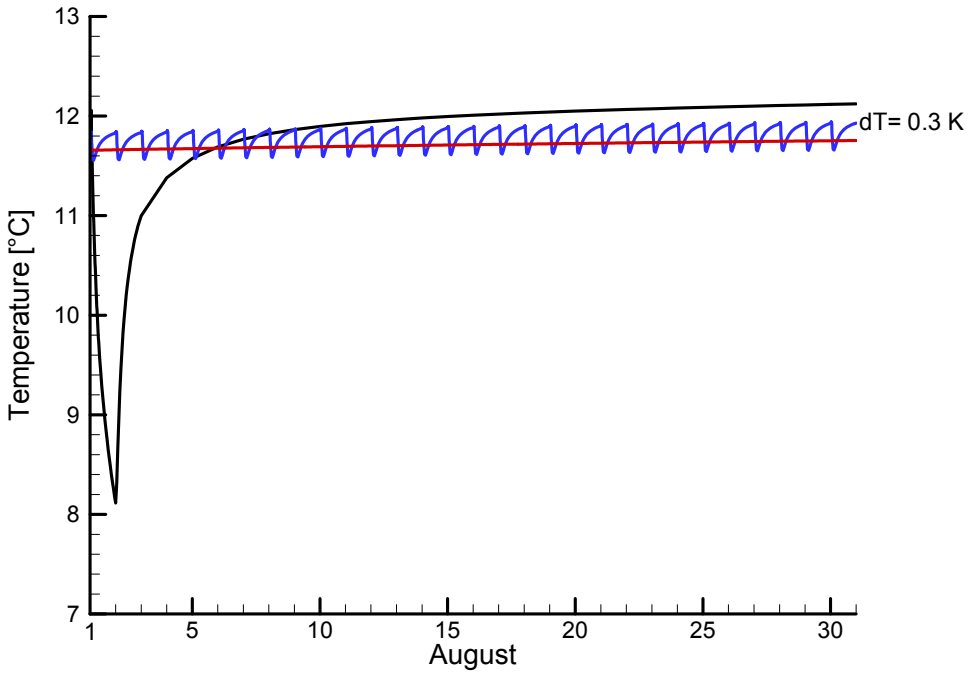

b)

Figure 3-10: Ground temperature at 50 m depth and in 0.1 cm distance from the BHE during a) February and b) August of the first year of operation for the two different load profiles. ΔT is the maximum difference between the different load regimes at the end of the individual months.

Due to heating operation the subsurface temperature in a certain volume around the BHE drops and a temperature drawdown develops. The development of this drawdown during the first operational year is shown in Figure 3-11 for the “single load profile” case. The subsurface temperature field is illustrated by vertical cross sections with the BHE at the intersection. Figure 3-11a shows the initial temperature field with horizontal stratified temperature isotherms. The temperature increases from ~11 °C at the surface to ~15 °C in 150 m. In January during the period of highest heat extraction, the typical drawdown around the BHE system can be recognized from Figure 3-11b. The BHE near-field cools even more than the mean surface temperature. The area of perturbation is approximately 5 m, but increases during further operation to ~10 m (Signorelli et al, 2003). The depth extent of the drawdown corresponds almost exactly to the borehole depth. Only after many more years of operation will the diffusive thermal front slowly progress deeper. During the summer months with low heat extraction the subsurface temperature field recovers, but does not reach the initial level any more (Figure 3-11c). This temperature drawdown is strong during the first years (Rybach and Eugster, 2002; see also later Chapter 8). Later the yearly deficit decreases asymptotically to zero.

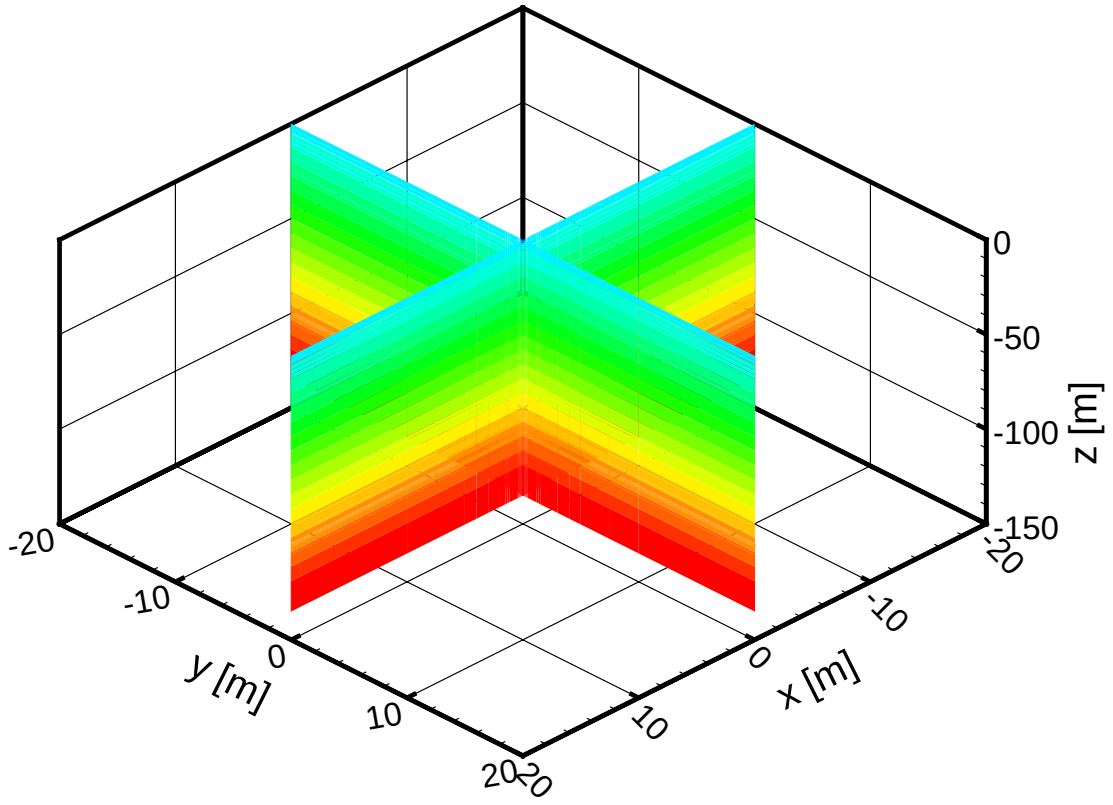

a)

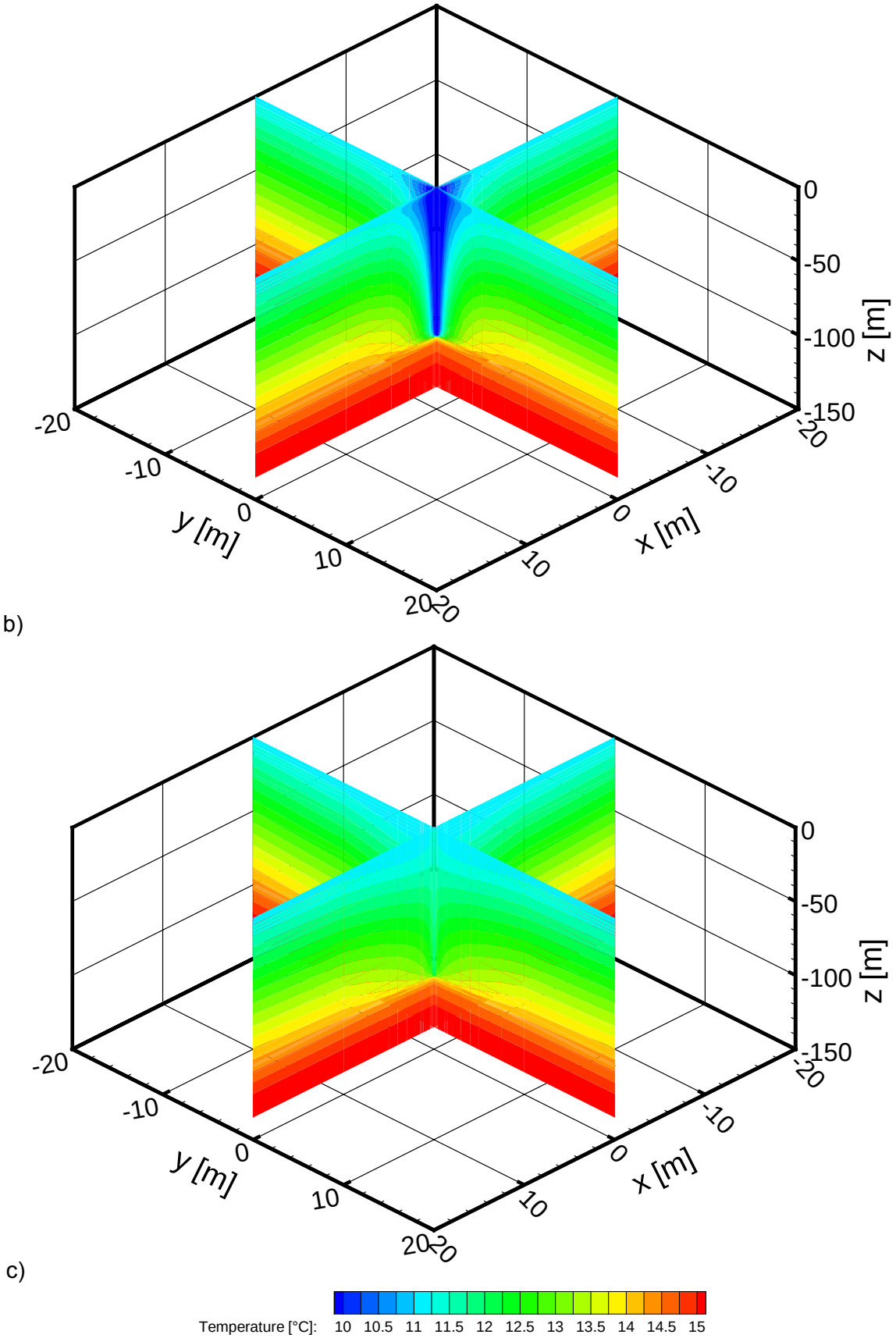

Figure 3-11: Development of the temperature drawdown around a BHE system, showing a) the initial temperature conditions, b) the temperature field in January and c) in August during the first operational year.

3.3 SOFTWARE COMPARISON: FRACTURE VS. EED

In Signorelli and Kohl (2002) and Signorelli et al. (2003) studies were performed to optimize the length of typical BHE configurations with regard to thermal power production, drilling cost and pressure loss. These investigations were performed using a software tool which was made available from Geowatt AG. This tool provides for the dimensioning of the hydraulics of a BHE system (e.g. pressure loss) and simulates the operation performance based on the semi-analytical software tool Earth Energy Desinger (EED) (Hellström and Sanner, 2000). To understand its simulation mode, a comparative simulation between FRACTure and EED for a single BHE and a BHE field is presented in this chapter.

3.3.1 SOFTWARE TOOL EED

EED is a useful tool in routine dimensioning of geothermal heat pump systems (Hellström and Sanner, 2000). It is an easy-to-use and fast computer program based on an algorithm adapted from the SBM model (Eskilson, 1986). EED, however, only provides an average value for the fluid temperature along the BHE and it is only valid for borehole depths between 20 – 200 m (Hellström and Sanner, 2000).

Claesson and Eskilson (1987) showed by numerical studies that the thermal process within the borehole can be decoupled from the thermal process in the surrounding ground when considering an average temperature along the borehole wall, T_b. Assuming an infinite line source within a homogeneous, isotropic infinite medium and by neglecting vertical heat flow along the BHE, the temperature field around the BHE is only dependent on time, t, and radial distance, r, from the borehole axis. Thus, for a constant specific heat extraction rate, q_{spez}, the evolution of the borehole wall temperature may be calculated by a dimensionless step function, the so-called ĝ-function (Eskilson, 1987):

Eq. 3-3
$$T_b(t) = T_0 - \frac{q_{spez}}{2\pi\lambda} \cdot \int_X^{\infty} \frac{e^{-\beta^2}}{\beta} d\beta \cong T_0 - \frac{1}{2\pi\lambda} \cdot \hat{g}$$

T_0 is the undisturbed ground temperature, representing the average temperature of the ground layers crossed by the borehole.

For constant heat extraction rate, the ĝ-function can be approximated by one of the following equations depending on the stage of operation (Ingersoll and Plass, 1948):

Eq. 3-4 $$\hat{g} \cong \ln\left(\frac{\sqrt{4\kappa t}}{r_b}\right) - \frac{\gamma}{2} \qquad t_c \le t \le t_s$$

Eq. 3-5 $$\hat{g} \cong \ln\left(\frac{H}{2r_b}\right) \qquad t \ge t_s$$

γ is the Euler's constant (~0.5772…). H is the so-called active borehole length over which the BHE extracts heat from the ground by pure conduction. The total depth of the BHE is H + D, where D is assumed as a shallow upper part of the borehole (< 10 m) which acts as thermally insulating. r_b is the borehole radius.

Eq. 3-4 is only valid when the thermal front has reached the surrounding rock and the heat capacities inside the borehole are not important. There exits a lower time limit, t_c, below which the model cannot simulate variations:

Eq. 3-6 $$t_c = \frac{5r_b^2}{\kappa}$$

The upper limit for the validity is the time t_s - the time scale when a single BHE has reached quasi steady-state conditions - defined from:

Eq. 3-7 $$t_s = \frac{H^2}{9\kappa}$$

After the system has reached the steady-state ($t \ge t_s$ >25 years), the ĝ-function can be approximated by Eq. 3-5.

The thermal processes in the ground are coupled to both the advective and diffusive thermal processes in the borehole. The heat transfer from the surrounding rock into the heat carrier fluid depends on the location of the pipes in the borehole relative to the borehole wall, and the advective heat transfer within the pipes. The general procedure in EED is to consider different thermal resistance associated with these different processes. These resistances are assembled to form a single thermal resistance between the heat carrier fluid and the borehole wall which is called the

“borehole thermal resistance”, R_b, and a thermal resistance between the fluids in the individual pipes called “internal thermal resistance”, R_a. For example, assuming the pipes as individual line sources, the thermal borehole resistance can be described:

Eq. 3-8 $$R_b = \frac{T_b - T_f}{q_{spez}}$$

T_f is the fluid temperature. Detailed description of the resistance for arbitrary pipe systems is given in Hellström (1991).

ĝ-functions have to be defined individually for every specific borehole geometry. Borehole fields are treated by a superposition of the ĝ-functions for single boreholes. EED has implemented >300 ĝ-functions for various borehole configurations computed by the numerical model SBM (Eskilson, 1986). Also implemented are databases of the thermal ground parameters as well as of properties of pipe materials and heat carrier fluid. Based on these input parameters, EED calculates a pseudo-fluid temperature which represents the average fluid temperature, $\overline{T}$, along the BHE. The $\overline{T}$ calculation is done by simulating first an average monthly base load, and then considering one extra pulse for peak heat load at the end of each month (see also Chapter 3.2.7). The comparisons to measured data (Sanner and Hellström, 1995) and further codes (Hellström et al., 1997), suggest that the accuracy of the model is well established.

3.3.2 GENERAL PROCEDURE

FRACTure and EED are compared for the simulation of a 100 m single BHE case, and for a rectangular field of 6 BHEs with 100 m length spaced by 7.5 m (see Figure 3-12). For the comparison, the input parameters described in Chapter 3.2.1 are used. Calculations are performed for base load (with monthly heat demand from Table 3-4) and peak load (variable one-daily operation cycle; see Chapter 3.2.7) profiles. In FRACTure, the base load is applied first and the temperature development during the whole month is simulated. At the end of every month a thermal output file is generated, which is used as a restart file to define the initial temperature conditions for the peak load simulation, which is performed at the end of the month.

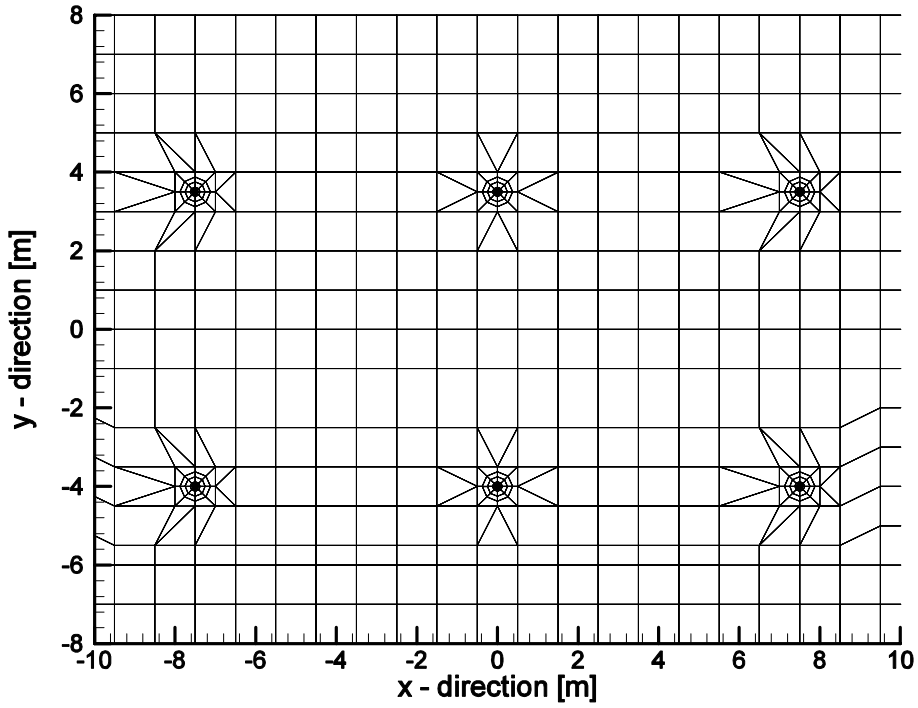

Figure 3-12: Plane view of the 2 x 3 BHE field model. The spacing in the BHE field is 7.5 m. The FE mesh is generated according to the findings in Chapter 3.2.

In EED simply the mean fluid temperature along depth of a BHE, $\overline{T}$, is supplied. In FRACTure modeling, the temperature evolution at every node in the FE mesh is available. For individual so-called monitor nodes, the temperature evolution can be written to an output file. When calculating $\overline{T}$, many monitor nodes must be set along the BHE pipes and the individual temperature evolutions are then averaged. It is commonly assumed that $\overline{T}$ corresponds to the mean value between the BHE outlet and inlet temperature, $(T_{out} + T_{in})/2$. Since it would be less time consuming to just monitor BHE outlet, T_{out}, and inlet temperature, T_{in}, and then calculate $(T_{out} + T_{in})/2$ as a substitute for $\overline{T}$, this assumption will be verified here by FRACTure modeling.

Simulations are shown for a single BHE and for the BHE field for the peak load case and $\overline{T}$ is compared to $(T_{out} + T_{in})/2$, for every month. For the BHE field, one central BHE with the highest mutual influence is analyzed. Due to the symmetry of the array the fluid temperatures in the four corner boreholes as well as in the two central boreholes are identical. Figure 3-13 shows that the fluid temperature decreases from September to January (~1 °C) and recovers again during the following period with lower heat extraction. For the period between September and January, the predicted

temperatures for the BHE field agree well with those for the single BHE. However, with further operation time, there is an increasing difference of ~1.5 K for the BHE field at the end of August. The cooling front of the BHE appears to need about five months to reach its BHE neighbors at 7.5 m distance. There is good agreement between the two mean fluid temperatures, whereby $(T_{out} + T_{in})/2$ is generally ~0.2 K lower than $\overline{T}$; homogenously distributed base loads would yield even smaller differences. We can conclude that $\overline{T}$ is well approximated by $(T_{out} + T_{in})/2$ and that for fast modeling, one can simply monitor the temperature evolution of T_{out} and T_{in}. Next, $\overline{T}$-values are used for comparison with EED. Additionally, also the minimum temperature calculated with FRACTure, T_{min} (corresponding to T_{in}), will be shown.

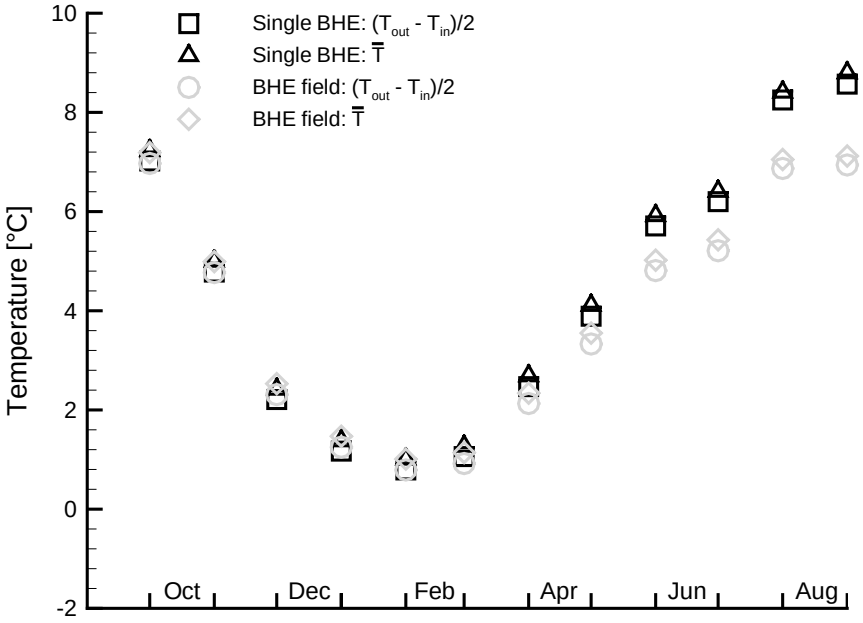

Figure 3-13: Using FRACTure, the mean fluid temperature between the BHE outlet and inlet, $(T_{out}+T_{in})/2$, is compared to the mean temperature along the BHE, $\overline{T}$, for the peak load case simulated. Temperatures are shown for the single BHE and the central BHE of BHE field. The two means compare well to each other.

3.3.3 COMPARISON OF SINGLE BHE MODELING

The FRACTure and EED simulations for the 100 m single BHE are now compared. Figure 3-14 shows the results for the base load simulation during the first and the 10th year of operation. The simulated $\overline{T}$-values are compared at the end of each month. In the first year of operation, the FRACTure temperatures vary from 12.7 °C in September to 5.7 °C in January and recover again up to 11.5 °C at the end of the first heating season in August. During the strongest heating period in winter T_{min} is ~0.7 K lower than $\overline{T}$. The EED results are always lower than the FRACTure $\overline{T}$-values, but higher than T_{min}. The difference is negligible during the summer period and <0.4 K in the winter months. For the 10th year, EED supplies only temperature values from January to December of the following year, and Figure 3-14 b compares the results for the 10th and 11th year. $\overline{T}$-values predicted by FRACTure are 4.9 °C in January and 11 °C in August, and about 0.5 to 0.8 K lower than in the first year. We recognize no noticeable decrease in production temperature after 10 years, and the thermal field near BHE systems apparently reaches a steady-state. The agreement of the two software tools is nearly perfect in the summer months, even after 10 years of operation. Also in the winter, the agreement is good with the FRACTure $\overline{T}$-values being only up to 0.4 K higher than the EED prediction. EED simulations seem to be more conservative in the wintertime and correlate here better with T_{min} of FRACTure.

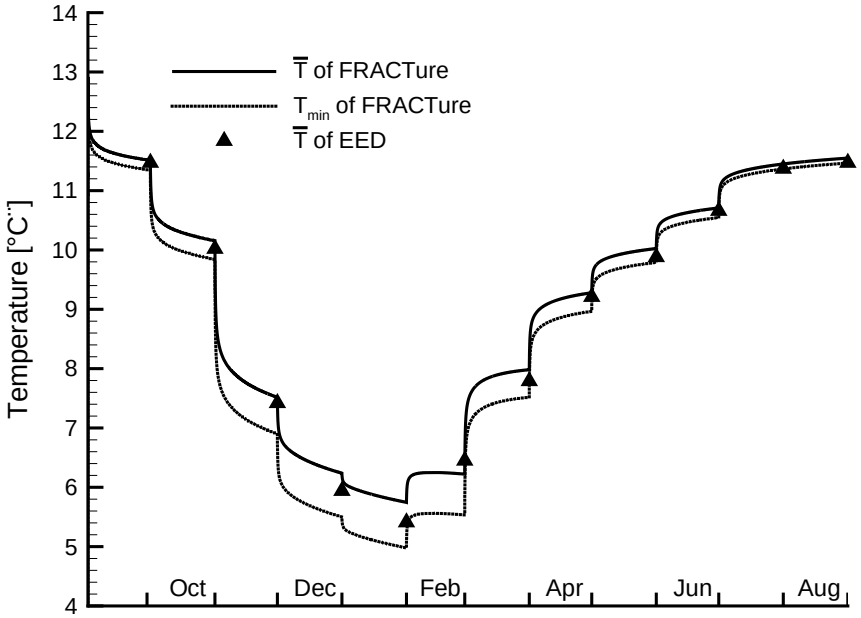

a)

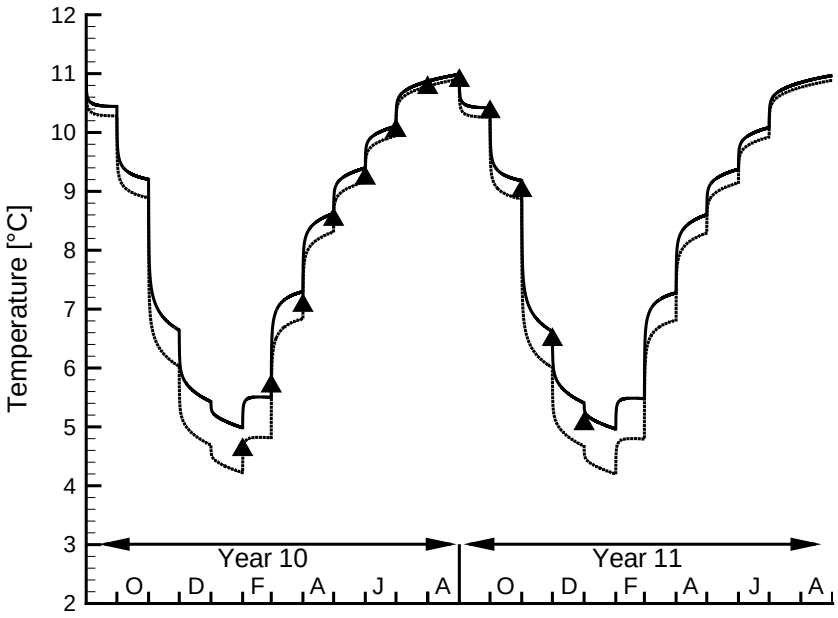

b)

Figure 3-14: Comparison of the mean temperature along the BHE, $\overline{T}$, for the 100 m single BHE simulated with EED and FRACTure for the base load case a) in the first year of operation and b) after 10 years. Additionally, for FRACTure also the minimum temperature, T_{min}, in the pipe system is also plotted.

Figure 3-15 shows the $\overline{T}$-values for the peak load case in the first year of operation. The comparison of the values is done at the end of the daily constant operation time for each month. The differences between FRACTure and EED are higher than for the base load case. EED $\overline{T}$-values lie generally between $\overline{T}$ and T_{min} calculated by FRACTure. In the winter months, $\overline{T}$ still correlates well with differences of ~0.5 K. But in summer, the bias rises up to nearly 2 K. During the summer months, with low heat extraction time, the EED temperatures correspond better to T_{min} of FRACTure. Here, EED results seem to be more conservative than the FRACTure simulations. On average the temperatures simulated by EED are 0.9 K lower than those by FRACTure. Considering the model input parameter in Table 3-1, this temperature difference can be expressed as a difference in thermal power of 780 W. In regard to the 5 kW thermal power applied during the peak load period, this means a ~15 % lower possible thermal power extraction by EED than for FRACTure. However, EED and FRACTure simulations show an overall good agreement for the peak load as well as for the base load case.

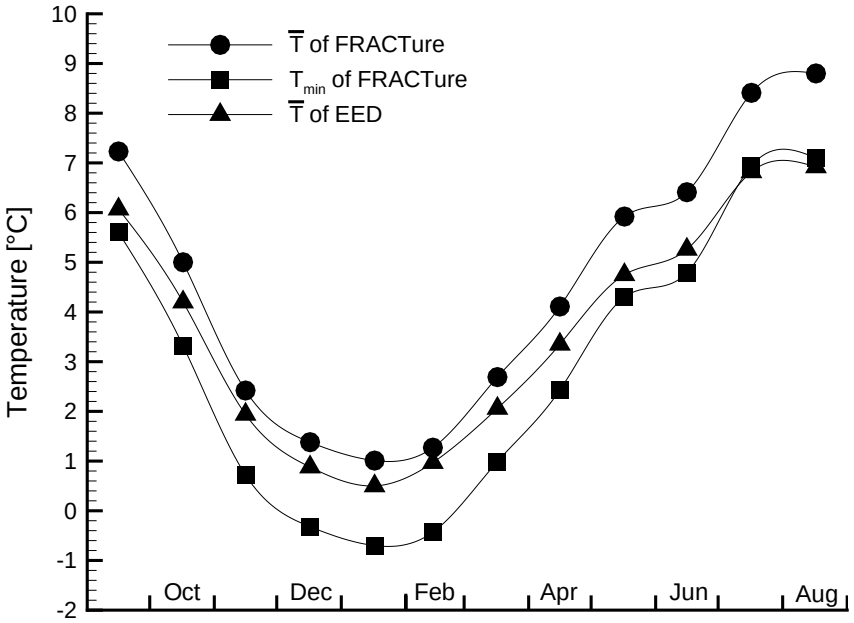

Figure 3-15: Comparison of the mean temperature along the BHE, $\overline{T}$, for the 100 m single BHE simulated with EED and FRACTure for the peak load case in the first year of operation. Additionally, for FRACTure also the minimum temperature, T_{min}, in the pipe system is also plotted.

3.3.4 COMPARISON OF BHE FIELD MODELING

In this section, the FRACTure and EED calculations for the BHE field in Figure 3-12 are compared. In Figure 3-16, the predicted $\overline{T}$-values are shown for the base load case in the 1st and 10th years. In EED only an average value of the fluid temperature over all six BHEs is given, in contrast to FRACTure where every BHE is monitored individually. Temperatures predicted by FRACTure are plotted for one central borehole (with the highest mutual influence) and one corner borehole. Additionally, T_{min} for the whole BHE field is also shown. The $\overline{T}$-values simulated by FRACTure vary from 12.7 °C in September to 5.7 °C in January and recover again up to 11 °C at the end of the first heating season in August. Until January the fluid temperature is comparable to the single BHE case (Figure 3-14 a). After January, the neighboring BHEs start interacting with each other and the difference between the corner and center borehole rises. At the end of August of the first operation year, temperatures in the corner borehole are ~0.3 K higher than in the central one. During the first year of operation, the EED and FRACTure values show a good agreement, with the EED $\overline{T}$-values being between the $\overline{T}$- and T_{min}-values of FRACTure. In January of the first year, the EED-temperature is ~0.4 K lower than the $\overline{T}$-values and ~0.4 K higher than T_{min} simulated by FRACTure. In August of the first year, the EED $\overline{T}$-value is in between the values of the corner and the center BHE.

The mutual influence gets more pronounced with further operation time. After 10 years of operation $\overline{T}$-values of the BHE field are ~2 K lower than for the single BHE (Figure 3-14 b). Now, the difference of $\overline{T}$ between the corner and center BHE is ~0.6 K. T_{min} is in January ~1.5 K lower than the temperature in the corner BHE. $\overline{T}$-values calculated by EED agree well with the FRACTure $\overline{T}$-values: during the winter month they match rather with $\overline{T}$ of the center BHE, whereas in summer - during the period of low heat extraction - with the $\overline{T}$-values of the corner BHE. Now, the temperature continues to drop even after the 10th year. A temperature drop of ~0.2 K is noticeable and the BHE field will not have yet reached steady-state conditions. This shows the importance of mutual influence which will be addressed later in Chapter 8.

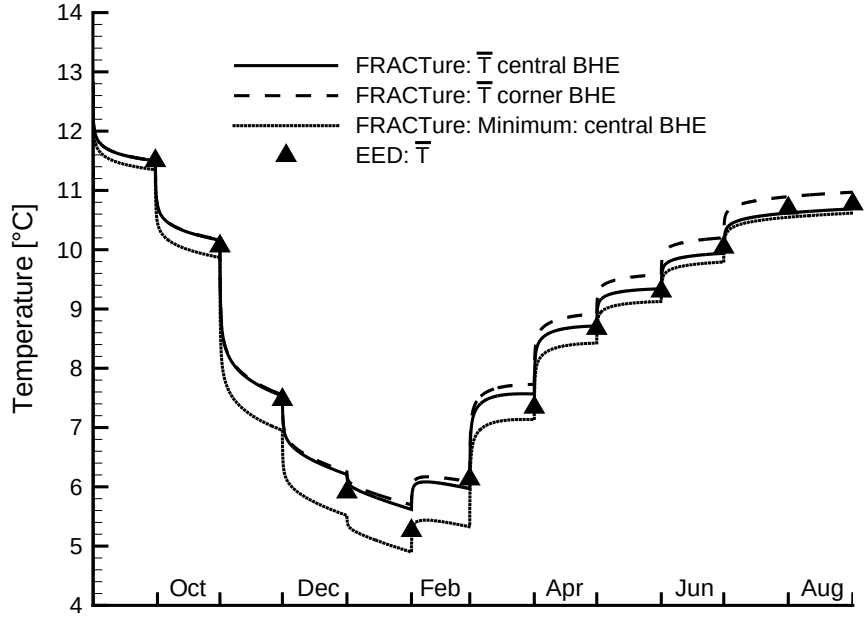

a)

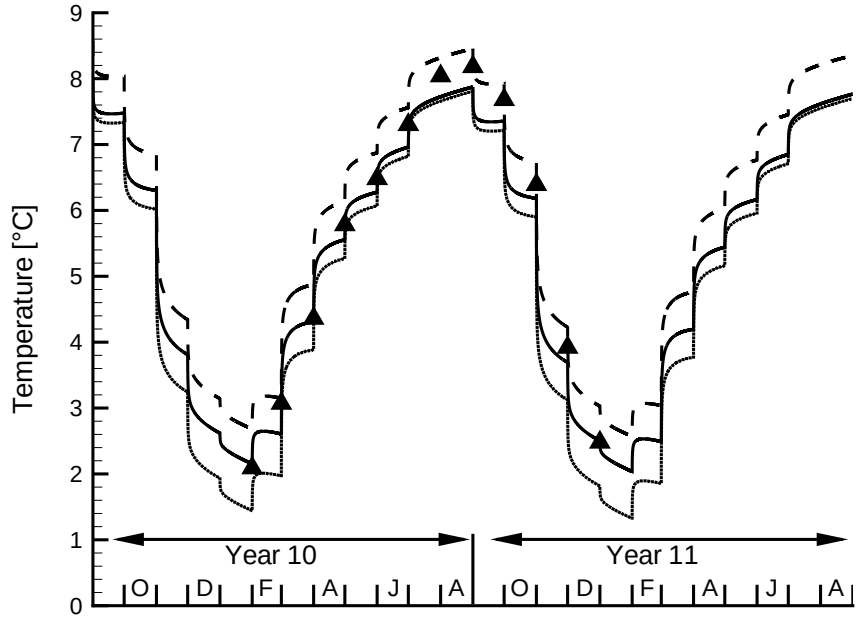

b)

Figure 3-16: Comparison of the mean temperature along the BHE, $\overline{T}$, for the BHE field simulated with EED and FRACTure for the base load case a) in the first year of operation and b) after 10 years. Additionally, for the FRACTure simulation also the minimum temperature in the pipe system is plotted.

Figure 3-17 illustrated the peak load case. Also here the mutual influence occurs in January. $\overline{T}$-values predicted by the two simulation tools agree generally well. The central and the corner BHE show an average difference of ~0.6 K to the EED-value. From the model parameter assumed (see Table 3-1), this can be expressed as a difference in possible thermal power extraction of 480 W between the EED and the FRACTure simulations. Compared to the applied 5 kW thermal power during the peak load period, this is a difference of ~10 %. Contrary to the single BHE case the agreement between EED and FRACTure is equally good for every month and T_{min} is generally 1 to 1.5 K lower than the $\overline{T}$-value calculated by EED.

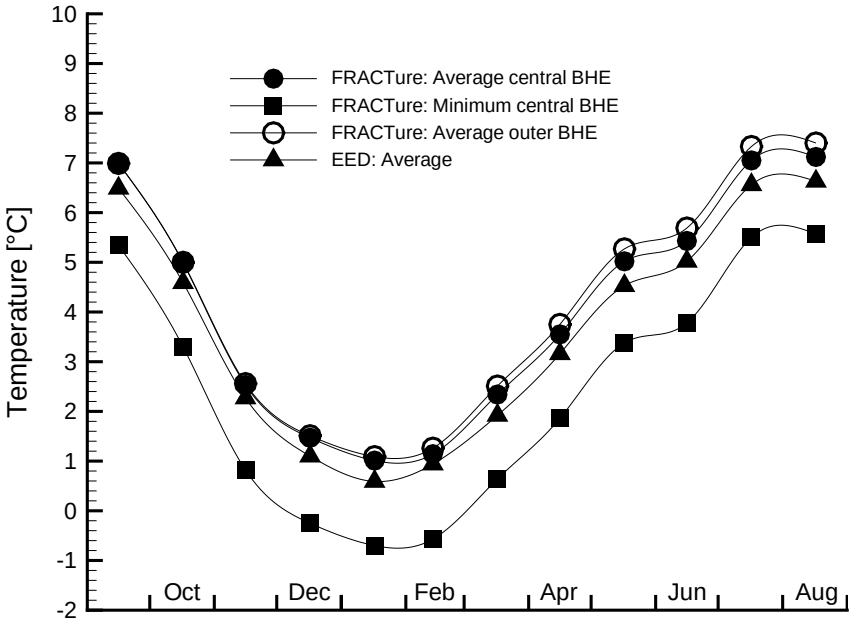

Figure 3-17: Comparison of the mean temperature along the BHE, $\overline{T}$, for BHE field simulated with EED and FRACTure for the peak load case in the first year of operation. Additionally, for the FRACTure simulation also the minimum temperature in the pipe system is plotted.

3.3.5 Discussion and Conclusions

Overall, the comparison of FRACTure and EED shows rather good agreement of the predicted average fluid temperature along a BHE. FRACTure and EED calculated similar $\overline{T}$ development for a single BHE as well as for a rectangular field consisting of 6 BHEs. However, a more detailed investigation of the results yields specific differences. EED generally predicts lower temperatures than FRACTure. The

differences are negligible for base load modeling and normally within a 1 K range for the peak load case. To accommodate the same temperature level as EED, FRACTure would forecast a 10 % higher production in the peak load case. It is important to note that the assumed peripheral pipe locations (see Figure 3-5) represent ideal conditions. Under real conditions, deviations in the pipe locations would cause lower productivity (see Chapter 4.2). When considering additionally effects such as imperfect backfilling, the productivity can even be lower. The uncertainty may be grater than to 10 %, and therefore, for dimensioning purposes, the more conservative simulations of EED are appropriate.

There is another difference between the two simulation tools which is important for dimensioning purposes. The minimum temperature, T_{min}, is critical and must not fall below a certain value in order not to run the risk that the subsurface freezes which leads to inefficient BHE systems and in the worst scenario to a shutdown of a plant. EED calculations do not provide T_{min}-values. Although, this is not critical in the case of a single BHE; T_{min} can be estimated from $\overline{T} \sim (T_{out} - T_{in})/2$ (see Chapter 3.3.2.) assuming the temperature difference of the BHE outlet and inlet according to the heat pump design figure (ΔT_{out-in}= ~ 3 - ~ 4 K). For BHE fields such a simple calculation for T_{min} is not possible. The mutual influence of neighboring BHEs is significant and the fluid temperature varies from one BHE to another BHE. The fluid temperature in the center BHEs of a BHE field is lower than at the border, as can be seen in Figure 3-16. The difference is more significant in larger BHE fields where the BHEs are surrounded by several BHEs. There is a risk that the subsurface around the center BHEs already freezes although one would not expect it due to the $\overline{T}$-values calculated by EED (the average of all BHEs involved). A thermal collapse may then occur. In this context it is clear that center BHEs provide generally less thermal power than BHE at the edge of a BHE fields. In FRACTure the temperature evolution in every BHE is calculated individually and special attention can be paid to the dimensioning of the center BHE. Simulations should be performed to quantify the efficiency of center BHEs. In some cases the contribution of a center borehole to the total production of a BHE field may be small. The BHE field may then be more efficiently operated by abandoning these boreholes and drilling the remaining BHEs deeper. This would additionally increase the spacing between the BHEs and make them more efficient.

The actual version of EED allows only a treatment of rectangular BHE fields with uniform borehole lengths. In practice, geometrical and structural considerations at the site usually determine the layout. In contrast FRACTure allows the simulation of any possible BHE field. However, since EED calculations are very fast (few minutes), it may be used to approximate the required size and layout for a BHE system before initiating more detailed analyses by a numerical model such as FRACTure. In future it is planned to optimize the mesh generation tool WinFra. The idea is to automate the mesh generation and set up a library with standard borehole configurations (standard 32 mm and 40 mm pipes in boreholes of different diameters). This would allow the easy insertion of a typical BHE configuration into arbitrary FE meshes and make FRACTure modeling much faster.

The comparative study between EED and FRACTure was performed only for the case of heating mode. However, nowadays there is an increasing demand for combined heating and cooling. It is highly important to optimize the different operation modes with each other. For this, especially, the short-time behavior is important. In EED, the definition of simple load profiles (base and peak loads) is rather rough and may not be sufficient. Therefore, also the thermal long-term behavior of BHE systems for combined heating and cooling should be investigated in detail. Since FRACTure allows simulating any load profile, it is also suitable for these kinds of investigations.

4. SHORT-TERM BEHAVIOR OF A BHE PLANT

In the previous chapter, the numerical model FRACTure was used for a qualitative simulation of BHE behavior. This chapter focuses on a quantitative interpretation of measured data. For this purpose, the first few hours of the very first operational cycles are treated. Starting the operation of a BHE system causes strong perturbations in the former undisturbed temperature field, which are strongest during the first operational cycle. Transient thermal processes in and around a BHE occur.

4.1 DATA SET "ROHNER"

From an extensive measurement project of the BHE plant "Rohner", situated in the village of Arnegg (Switzerland), a data set of the systematically measured outlet and inlet temperatures is available. The plant comprises a 265 m deep double U-type BHE and is operated with water as heat carrier fluid. The tubes consist of standard polyethylene material. The volumetric flow rate is estimated to be 3606 l h^{-1} corresponding to a flow velocity of 0.6 m s^{-1} in the pipe. However, the flow rate may vary due to the daily varying grid voltage. A detailed geological profile is available with thermal conductivity measurements on borehole cuttings (Signorelli et al., 2003). It comprises "Upper Freshwater Molasse" rocks, mainly sandstones and conglomerates with few intercalated marly layers. The average thermal conductivity of the different cutting probes is 2.88 W m^{-1} K^{-1}. Assuming a geometrical mean, the thermal conductivity of the rock matrix is calculated to be 2.65 W m^{-1} K^{-1} with a porosity of 5 %. The heat capacity is approximated from literature values by 2.52 MJ m^{-3} K^{-1} (Leu et al., 1999). Before the beginning of the initial operation a temperature profile was measured along the entire length of the BHE (see Figure 4-1). The measurements start at 10 m depth and are therefore only marginally effected by seasonal temperature variations. The zone down to ~50 m may be affected by global warming – a topic currently investigated within the framework of the ETH project "Determination of Short Term Climate History by Three-Dimensional Inversion of Borehole Temperature Data" at the Institute of Geophysics. From linear extrapolation the ground surface temperature (GST) is estimated to be 9.4 °C, which agrees well to 9.9 °C provided by the GST map of Switzerland (see Chapter 5). The

average temperature gradient along the BHE is 2.8 K per 100 m. The BHE design, material properties and boundary conditions are listed in Table 4-1.

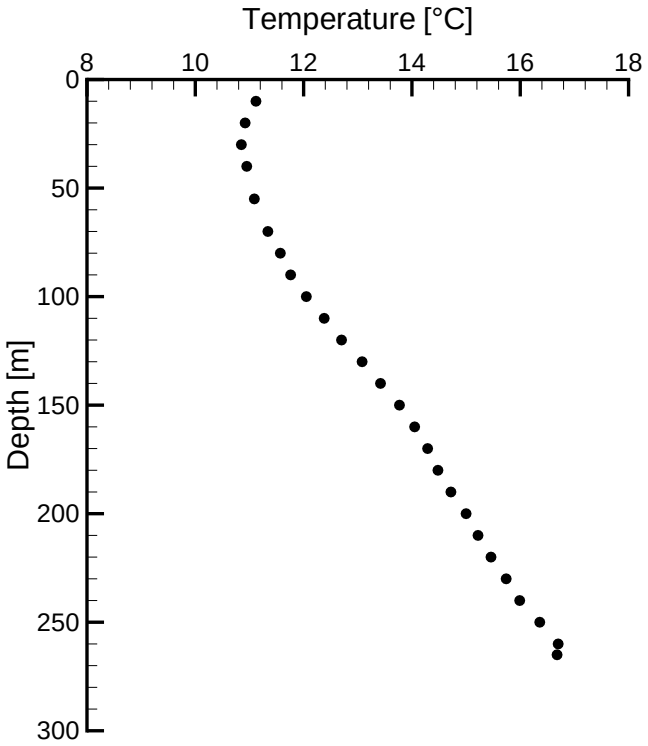

Figure 4-1: Initial temperature profile along the BHE plant “Rohner” (22 February 2002).

Table 4-1: BHE design, material properties, and boundary conditions for the “Rohner” BHE.

BHE design	Depth= 265 m		
	Pipe radius= 40 mm (inner), 32.6 mm (outer)		
	Borehole diameter = 135 mm		
Material properties		Thermal conductivity [W m^{-1} K^{-1}]	Heat capacity [MJ m^{-3} K^{-1}]
	Rock matrix	2.65	2.52
	Pipe	0.42	1.62
	Grouting	0.81	2.00
	Heat carrier fluid (Water)	0.6	4.19
Boundary conditions	Constant basal heat flow=		80 mW m^{-2}
	Constant ground surface temperature,		$\langle GST \rangle_a$= 9.4 °C
	Estimated average flow velocity in the pipe,		v_p= 0.6 m s^{-1}

After drilling the BHE, the operation start was postponed for several months, and thus, the temperatures recorded during the first operation cycle in spring 2002 represent the thermal conditions of the initial temperature field. Since then, the BHE outlet and inlet temperatures were continuously measured. The registration is done using a DL2 data logger from Delta-T Devices Ltd. Unfortunately the temperature could only be stored with one decimal place. Thus, the recorded temperature evolution shows steps (see Figure 4-2). Figure 4-2 shows the measured BHE outlet and inlet temperatures during the first operation cycle. The temperatures increase first due to the initially warm stagnant water column in the pipe and drop quickly to lower values once the water column has changed. This temperature peak is most clearly visible during the first operational cycle, and will show up at the start of every following operation cycle. The occurrence, however, depends on the length of the recovery period between two operation cycles. The highest production temperature is 13.6 °C, occurring between 9.5 and 13 min. As mentioned in Chapter 3.2.4, the peak is delayed and does not occur after the half circulation time (7.4 min). Figure 4-2 furthermore shows the difference between T_{out} and T_{in}, ΔT, ranging between 5 and 4 K. This results in an extremely high average thermal power extraction of ~19 kW (specific heat extraction rate of ~70 W m^{-1}) during the first 3 hrs of operation. It may be noted that this is an instantaneous value and the thermal power decreases during the subsequent operation. The average thermal power, which is extracted from the “Rohner” plant, is about 12 kW (corresponding to a specific heat extraction of ~45 W m^{-1}).

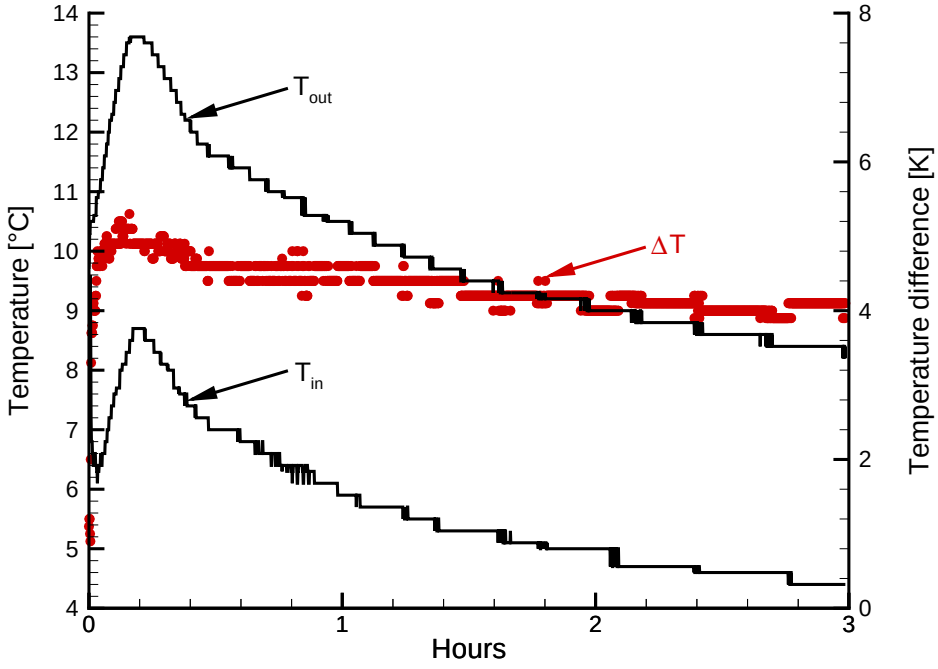

Figure 4-2: Outlet and inlet temperature, T_{out} and T_{in}, of the BHE plant "Rohner" during the initial operation cycle. The temperature difference between T_{out} and T_{in}, ΔT, is also plotted in red (right x – axis).

4.2 Numerical Simulation

To test FRACTure on a measured data set, the first operational cycle is simulated and the calculated temperature evolution is compared to the measurements. Therefore, the measured history of BHE activities is discretized into a numerical operation schedule by a load-time function (see Chapter 3.1). In each time step the measured temperature difference is subtracted from the simulated production temperature and the resulting temperature value is used as the new inlet temperature.

First the numerical mesh is generated according to the description in Chapter 3.2 and the BHE characteristics in Table 4-1. Except for the tube position inside the BHE, all modeling parameters are known. However, the tube position is an important factor for the simulation which defines the characteristics of the temperature curve. The closer the tubes are located to each other, the higher the mutual influence is (e.g. the cold downflow cools the warm upflow one). Additionally, the contact to the surrounding rock is also important. Best thermal contact between the heat carrier

fluid and the rock is achieved for a peripheral location with the tubes directly at the borehole wall. As at all other sites, the effective tube location in the “Rohner” BHE is not known and it must be expected that it even varies with depth. Therefore, three meshes are set up representing different tube positions (see Figure 4-3), which all are extreme situations: In A the tubes are peripherally arranged with maximum separation. Mesh B considers the tubes in the center of the borehole, touching each other. In C the tubes are again peripherally arranged, but close to each other on one side of the borehole. The comparison of these different model runs with the measurements also allows the interpretation of the possible tube location in the BHE.

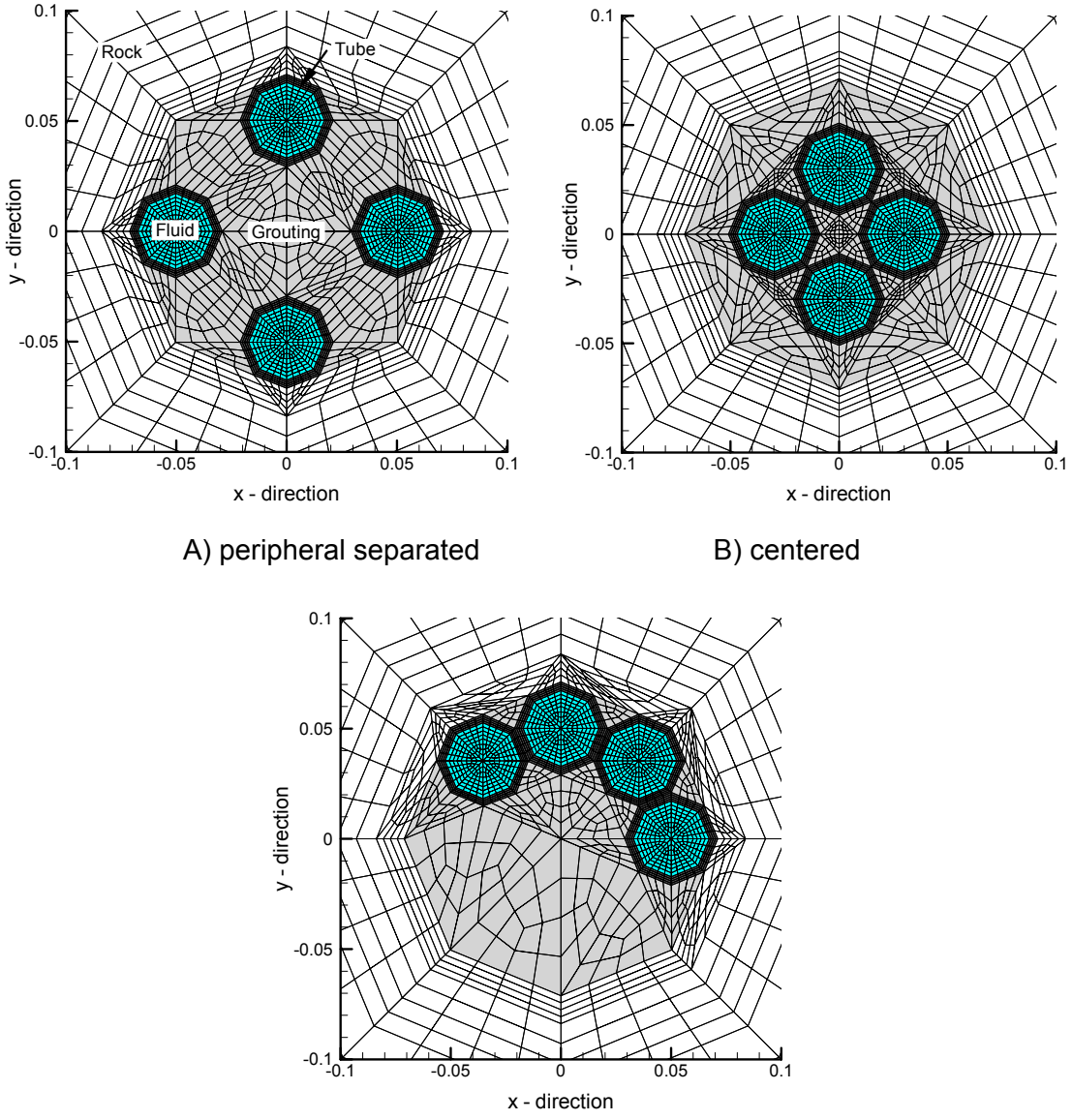

Figure 4-3: Three different numerical meshes, representing the extreme cases for the possible tube location.

The initial condition for the numerical simulation is the undisturbed subsurface temperature field. Therefore, in all three model runs the initial state of the FE mesh is adjusted to the measured temperature profile. Figure 4-4 shows this fit with a local heat flow of 80 mW m^{-2} and a GST-value of 9.4 °C. The misfit in the first 50 m can be neglected, since this region only influences the production temperature in the very first minutes and the later temperatures are mainly dominated by the temperature conditions at the bottom of the BHE.

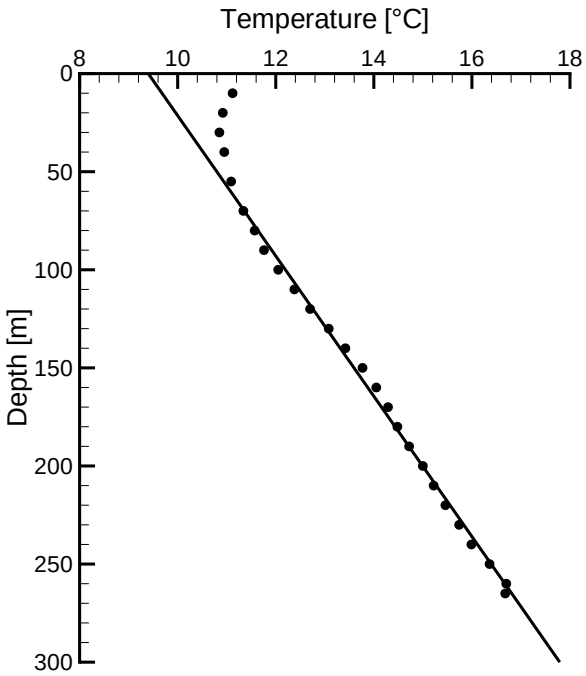

Figure 4-4: Adjustment of the initial model conditions (line) to the initial temperature profile measured along the BHE (dots).

Starting from this initial temperature field, simulations are performed for a 4 hour period. Thereby, the flow velocity and the difference between the outlet and inlet temperatures, ΔT, are fixed according to the measured data. Figure 4-5 shows the simulated production temperatures. The tube positions and the associated mutual influences impact the operation only in the long-term run. The overall highest production temperature is achieved for model run A, corresponding to the FE mesh in Figure 4-3 A). Here, the tubes are farthest apart and are in direct contact with the surrounding rock. The lowest temperatures develop for model run B, which is due to the tubes touching each other and to the insulating effect of the grouting material. Whereas the produced temperatures for model runs A and C seem slowly to

approach a constant value after 4 hrs, the temperatures in model runs B still clearly decrease. It may be noted that the tube position B is unrealistic in reality. When comparing the simulated temperatures to the “Rohner” measurements, a good agreement of the peaks in the short-term results with the simulated peaks being slightly higher. In the long-term behavior, the measured temperatures also stabilize and approach a constant value. The curve shape indicates a peripheral position of the tubes close to model run A.

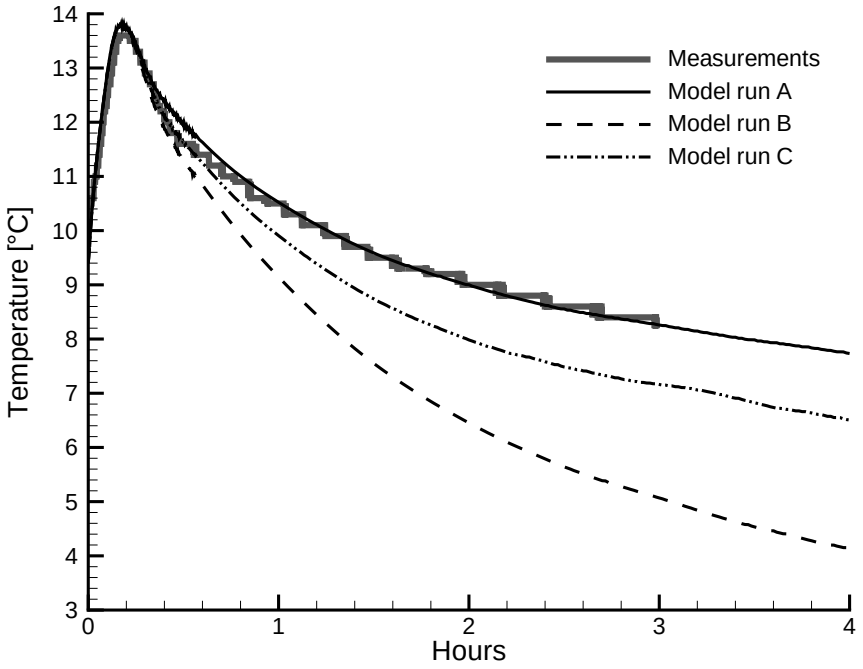

Figure 4-5: Comparison of the measurements and the simulated temperature evolution for the three different model runs from Figure 4-4 during the initial operation.

4.3 DISCUSSION

On the basis of measured data, the software FRACTure could be validated for the simulation of BHE systems. Three different model runs were performed, which all represent extreme tube locations, and the thermal behavior of the real location can be expected between these three locations. The comparison of measurements and simulated temperatures shows good agreement. At short-time the temperature peak is well reproduced by all model runs. The long-term temperature evolution characterizes the borehole conditions for a specific BHE plant. For the “Rohner” plant, it indicates a peripheral location of the tubes which may generally be expected

for BHE systems. Pipes are wound up on a decoiler and when installed into borehole, outwardly directed forces push the tubes towards the borehole wall and tube locations may vary between the pipe locations described by models A and C in Figure 4-3. To prove this assumption, modeling of other data sets should be performed. For this purpose, measurements must be recorded in short time intervals as for the “Rohner” plant. Temperatures should be measured to 0.01 K. Such data sets are normally not available in practice, since they are only recorded for scientific projects (Signorelli et al, 2003).

The simulations show that the production temperature depends on the tube position. The possible location inside the borehole can be estimated, when the measured temperature response is used as an indicator for the location. For this purpose, numerical models such as FRACTure are particularly suitable, since they allow a detailed representation of the conditions inside the borehole due to flexible mesh generation. Every tube can be separately accounted for. Furthermore, the possibility to define load-time functions in FRACTure allows a detailed consideration of the operational cycle. This all makes FRACTure a sophisticated simulation tool.

5. DATA ANALYSES I: GROUND SURFACE TEMPERATURE

This chapter addresses the data analyses of ground surface temperature (GST) data in Switzerland and summarizes the results published by Signorelli and Kohl (2004). Already Stadler et al. (1995) emphasized the importance of GST for the dimensioning of BHE systems. High variability in GST due to topographical effects can significantly affect the output from a BHE. The temperature field along the depth of a BHE strongly determines the heat content of the subsurface. In this, the GST represents an additive constant. At higher altitudes BHEs must be drilled deeper due to lower GSTs and temperature gradients.

Therefore, a regional GST distribution should be determined. Our intent is to obtain a practical method which would neglect local, small-scale effects. We focus on main population areas of Switzerland characterized by modestly undulating topography. First, we systematically analyze Swiss GST data for signs of recent climatic change and annual variations. Secondly, we investigate the GST dependence on altitude and insolation, as well as the relation between GST and surface air temperature (SAT) and, from the latter, develop a pragmatic approach to producing a GST map. Finally, the results are compared to extrapolated GST values from boreholes. However, the evaluation of GST not only represents a common aspect of applied but also of general geothermal research like paleoclimatic studies.

Besides altitude and solar radiation, GST depends on factors like ground moisture, wind speed, and vegetation cover and vegetation height. In Signorelli and Kohl (2004), a method to estimate GST described by Pikul (1991), which accounts for all these influences, was described in details. His approach is based on the “resistance method” to estimate surface heat flux described by Berkowicz and Prahm (1982) considering individual resistances of the heat transfer between ground surface or vegetation and atmosphere. Pikul’s approach has proven to be accurate in determining GST for meadows, but only for SAT > 0 °C and when there is no snow cover or freezing SAT. Because of the extensive data record required, it is not suitable for calculating input parameters for BHE models. Furthermore, it is unlikely that this method can be extended in its present state to other locations such as urban areas. Therefore, we focus here only on the dependence on altitude and solar

radiation. However, Pikul's approach illustrates well the complexity and limitation of estimating GST from meteorological data.

5.1 INTRODUCTION

As a first approximation GST depends linearly on altitude (Bendel, 1948; Powell et al., 1988) where the lapse rate corresponds approximately to the atmospheric lapse rate. However, the GST is 1 to 4 K higher than SAT. The magnitude of this difference is caused by the combined effect of snow cover insulating the ground and ground moisture's latent heat to buffer GST at the freezing point (Lewis and Wang, 1992). GST also depends on surface exposure to insolation, which itself depends on slope angle and orientation (Blackwell et al., 1980; Šafanda, 1999). One expects north-facing slopes to be cooler by some degrees than south-facing slopes due to the former's lower insolation.

Other important factors in GST are vegetation (Lewis, 1998, Lewis and Wang, 1998), and rock surface structure. Kappelmayer and Haenel (1974) found temperatures in forests at a depth of 1 m to be about 1 K lower than under adjacent meadows. Not only are the surface conditions extremely variable but the microclimate as well, especially in mountainous regions. Blackwell et al. (1980) observed GST differences of up to 4 K at neighboring boreholes.

5.2 METEOROLOGICAL DATA

5.2.1 GENERAL

The Swiss Meteorological Institute (SMI) operates a dense network of meteorological stations. In addition to common meteorological parameters like SAT, solar radiation, precipitation, wind speed, and degree of cloudiness, temperature measurements at different soil depths are also taken at 28 stations.

Since 1981 recording at these stations has been automated. Measurements recorded before 1981 are difficult to interpret due to non-standardized registration. First analyses of these data were performed by Rybach and Pfister (1994) and Busslinger und Rybach (1999). Here we analyzed only measurements from the automated stations between 1981 and 1999 (date of last publication), for the first time systematically.

The meteorological stations are mostly located within undisturbed meadow environments at some distance from buildings. SMI data ensure that the conditions around a measurement site are representative for a broader area. At all stations GSTs are recorded with close to no interruption every 10 minutes at depths of 5 cm, 10 cm, 20 cm, 50 cm and 100 cm by identical, horizontally-placed resistance thermometers (Defila and Brändli, 1989). Hereafter, the measurements at 5 cm depth will be referred to as GST. The values of other parameters, like SAT or global radiation, which we also require for the following investigations, are measured at an altitude of 2 m above the surface (= screen height z_s).

Table 5-1 lists selected measurement parameters for all 29 stations with GST records. $<GST>_a$ and $<SAT>_a$ values represent the annual mean averaged over the whole measurement interval. The global radiation values are taken from Z'graggen (2001). The spatial distribution of the stations is shown later in Figure 5-5. Nearly all stations are located in the Swiss Alpine Foreland in the densely populated area between 200 and 1000 m a.s.l.. Here we find the highest density of BHE systems (see Figure 1-2) and it is the area of our major interest. In the complete data set, the lowest $<GST>_a$ of 5.27 °C is measured in Samedan (Station-no. 28; 1705 m a.s.l.) located in the Alpine mountain area and the highest $<GST>_a$ (13.29 °C) is observed in Locarno-Monti (Station-no. 4; 366 m a.s.l.) in southern Switzerland. Only one site is situated in a heavily populated area (Station-no. 14, Zurich - SMA). The station shows no evidence of a temperature behavior different from that of other stations in the same altitude range (see Table 5-1). In contrast with earlier considerations (Rybach and Pfister, 1994), we do not split the data into northern and southern Alpine zones because we have few southern stations (Station-no. 1, 3, 4, and 19) and no persistently different GST behavior.

Table 5-1: Meteorological stations and their annual mean values of GST ($<GST>_a$), and SAT ($<SAT>_a$), averaged over the measurement interval.

L) lowland, E) elevation, S) south-facing slope, C) canyon-type valley, EA) east-facing slope and D) depression

No.	Station	Longitude	Latitude	Exposure	Altitude [m a.s.l.]	$<GST>_a$ [°C]	$<SAT>_a$ [°C]	Global radiation [W m^{-2}]
1	Locarno-Magadino	8° 52' 40.71"	46° 9' 50.97"	L	197	13.03	11.50	136.6
2	Basel-Binningen	7° 34' 57.88"	47° 32' 28.38"	E	316	11.96	10.27	121.0
3	Stabio	8° 55' 56.1"	45° 50' 36.35"	L	353	11.78	10.59	131.6
4	Locarno-Montì	8° 47' 14.7"	46° 10' 21.23"	S	366	13.30	12.14	158.7
5	Aigle	6° 55' 14.93"	46° 19' 24.42"	L	381	11.87	10.00	140.8
6	Buchs-Aarau	8° 4' 46.55"	47° 23' 4.09"	L	387	11.53	9.49	120.8
7	Changins	6° 13' 58.92"	46° 23' 50.93"	E	430	11.99	10.23	136.6
8	Guettingen	9° 16' 46.28"	47° 36' 5.84"	E	440	11.45	9.02	125.8
9	Reckenholz	8° 31' 3.06"	47° 25' 39.78"	L	443	11.10	9.16	127.8
10	Vaduz	9° 31' 2.17"	47° 7' 38.95"	L	460	10.87	9.90	139.7
11	Pully	6° 40' 3.11"	46° 30' 43.87"	S	461	12.00	10.76	146.5
12	Waedenswil	8° 40' 36.06"	47° 13' 16.66"	EA	463	10.85	9.31	118.7
13	Sion	7° 20' 15.19"	46° 13' 8.49"	L	482	10.55	9.84	153.4
14	Payerne	6° 56' 33.72"	46° 48' 49.58"	E	490	11.30	9.22	134.4
15	Taenikon	8° 54' 16.87"	47° 28' 47.49"	L	536	10.67	8.47	125.4
16	Chur-Ems	9° 31' 49.55"	46° 52' 13.89"	L	555	10.98	9.39	138.0
17	Zürich-SMA	8° 33' 57.03"	47° 22' 41.31"	S	556	11.10	9.19	130.7

Continuing Table 5-1

No.	Station	Longitude	Latitude	Exposure	Altitude [m a.s.l.]	<GST>$_a$ [°C]	<SAT>$_a$ [°C]	Global radiation [W m^{-2}]
18	Bern-Liebefeld	7° 25' 13.39''	46° 55' 41.96''	L	565	10.84	8.92	122.3
19	Comprovasco	8° 56' 8.35''	46° 27' 33.9''	C	575	11.31	10.28	127.9
20	Fahy	6° 56' 28.08''	47° 25' 24.9''	L	596	10.52	8.76	125.4
21	Visp	7° 50' 34.62''	46° 18' 10.31''	C	640	9.41	9.20	148.8
22	St.Gallen	9° 23' 58.25''	47° 25' 32.05''	C	779	9.30	8.08	123.3
23	La Chaux-de-Fonds	6° 47' 49.8''	47° 5' 8.04''	D	1018	7.91	6.36	132.5
24	Robbia	10° 3' 40.07''	46° 20' 47.92''	C	1078	7.63	6.93	150.4
25	La Frêtaz	6° 34' 35.16''	46° 50' 26.19''	S	1202	7.61	5.90	147.8
26	Adelboden	7° 33' 39.85''	46° 29' 31.28''	EA	1320	8.36	5.99	131.8
27	Davos	9° 50' 39.71''	46° 48' 47.32''	E	1590	6.78	3.41	158.4
28	Samedan	9° 52' 41.88''	46° 31' 46.09''	L	1705	5.29	1.62	159.9
29	Rietholzbach	8° 59' 38.38''	47° 22' 48.84''	L	752	10.19	8.07	129.6

5.2.2 CLIMATE INDUCED GST VARIATION

Global SAT measurements indicate a temperature increase of 0.3 to 0.6 K over the last 100 years, with the 1990s being the warmest decade of the last century (IPCC, 2001). A similar trend must be expected for the GST data. In this chapter we therefore investigate from the last two decades possible transient effects in our data set. This short recording interval can be strongly biased by single annual events. Moreover, due to the highest SAT variability of the last century in the study period, GST data interpretation can be biased when the results are extrapolated over 100 years.

Both annual GST and monthly GST (= GST_m) data were used to calculate the transient behavior. Using a sinusoidal linearization of the form of Eq. 5-1, the trend of the recent climate history was determined by calculating the deviation of GST_m data from a uniform annual variation, ΔGST_m:

Eq. 5-1 $$\Delta GST_m = GST_m(t) - \left[< GST >_a + A_{dom} \sin(\omega t + \varphi)\right]$$

where $<GST>_a$ is the mean GST over the measurement interval, t the time, A_{dom} the dominant GST – amplitude, ω is 2π/year, and, φ the phase.

The analysis shows a high variability at the individual stations Figure 5-1a and b. Generally, stations in the Alpine Foreland and in southern Switzerland (in total 23 stations) show a smaller increase (average linear trend of 0.6 K per 20 years) than do Alpine stations (1.3 K per 20 years, in total 6 stations). However, as we expected, small annual events can strongly influence these data: the Foreland stations 1, 11, and 14 show no increase and station 15 has an identical increase to that in the Alpine environment.

By using $<GST>_a$, the average over the 20 years of recording, we might underestimate actual $<GST>_a$ values due to observed climatically induced behavior. Alpine stations would result in a 0.65 K (50 % of total variation) and Foreland stations in a 0.3 K higher $<GST>_a$ value.

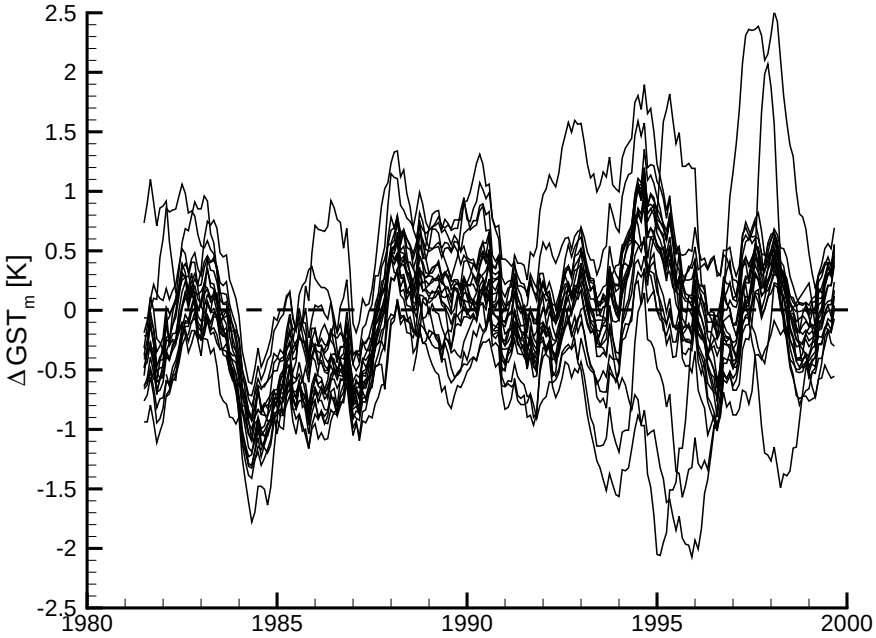

a)

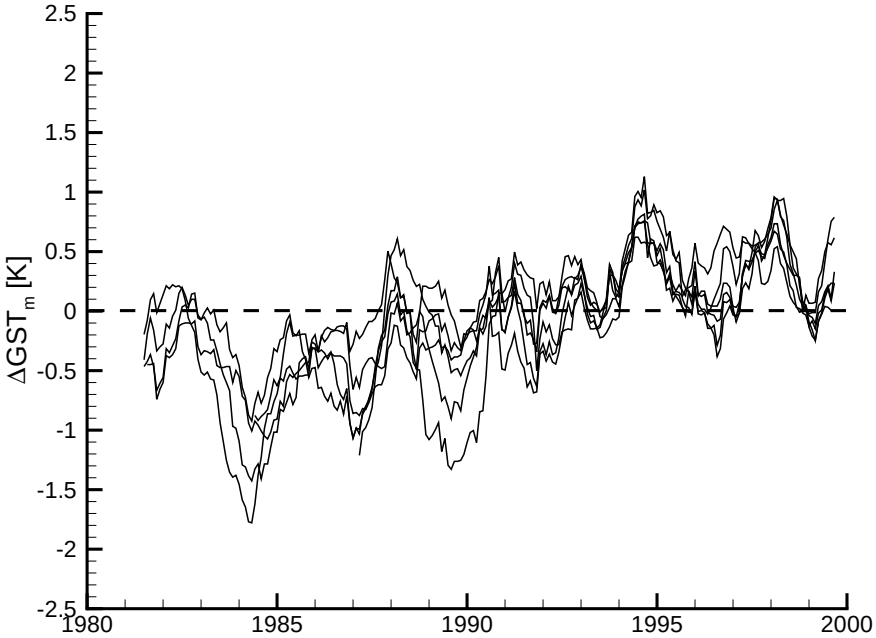

b)

Figure 5-1: Variation of monthly GST (GST_m) relative to the corresponding uniform sinusoidal GST variation as a moving average over 1 year, showing cooling and warming in the Alpine Foreland and southern Switzerland (a), and the Alps (b) during the last two decades.

5.2.3 ANNUAL GST AND SAT VARIATION

In Figure 5-2 the mean monthly GST (= $\langle GST \rangle_m$) and SAT (= $\langle SAT \rangle_m$) are compared for Zurich-SMA (station-no. 17) and Davos (station-no. 27). At Zurich-SMA, a typical station for the Swiss Alpine Foreland, $\langle SAT \rangle_m$ generally just approaches 0 °C in winter (see Figure 5-2a) and $\langle GST \rangle_m$ has nearly a constant offset. However, Davos, at its high elevation in an Alpine environment, is characterized by long winter seasons and here $\langle SAT \rangle_m$ goes strongly below zero, but $\langle GST \rangle_m$ remains above the freezing point (Figure 5-2b). Both snow cover insulating the ground from the cold air and the latent heat of ground moisture prevent the ground from freezing even during long sub-zero $\langle SAT \rangle_m$ periods. This conforms to observations by Lewis and Wang (1992).

The phenomenon of $\langle GST \rangle_m$ remaining above the freezing point can be observed at five more meteorological stations which all are located above 1000 m a.s.l. (Station-no. 23, 24, 25, 26, and 28). The duration of sub-zero SAT period is longer the higher the station is located and the effects of insulating snow cover and of the latent heat of ground moisture become more and more important (see also later Figure 5-3). At Davos, this phenomenon lasts from December to March (see Figure 5-2b). Thus, for the annual variation of $\langle GST \rangle_m$ regions of different behaviors can be observed.

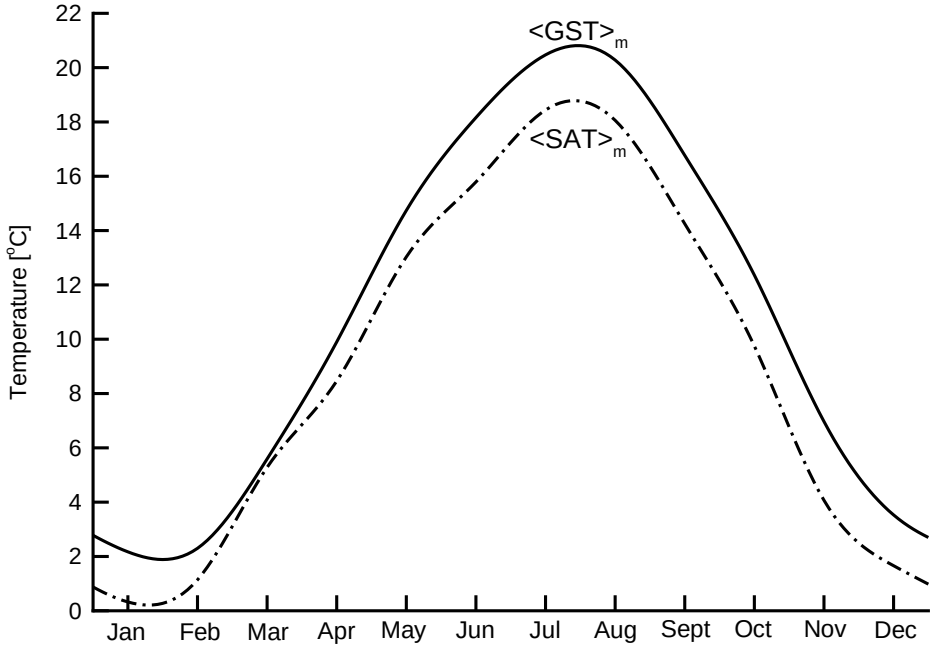

a)

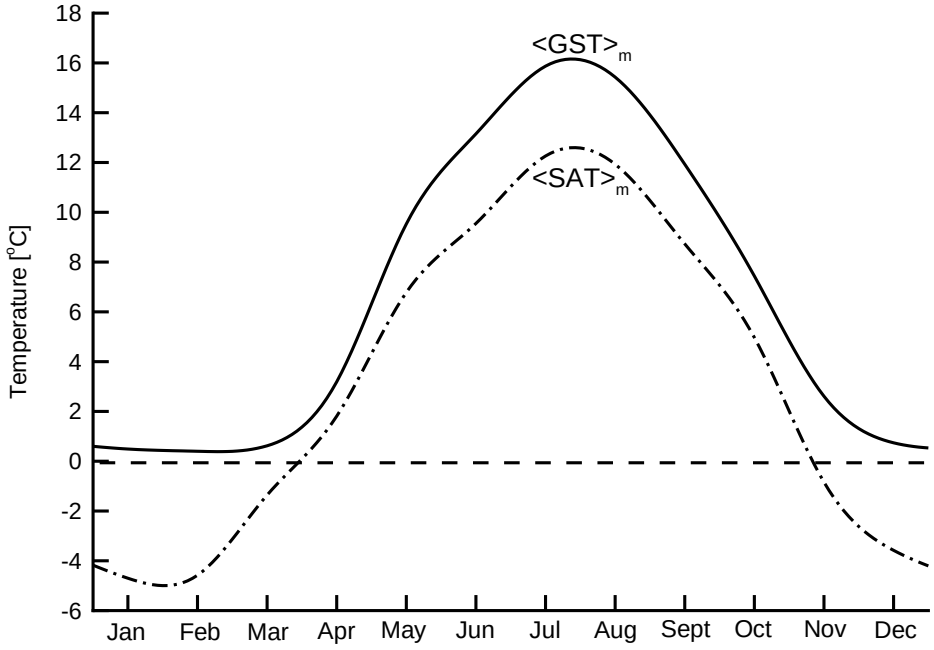

b)

Figure 5-2: Annual variation of mean monthly GST ($<GST>_m$) and SAT ($<SAT>_m$) values averaged over the last two decades at the meteorological stations of Zurich-SMA (a) and Davos (b). Snow cover and latent heat of ground moisture buffer GST at 0 °C even during long periods of freezing $<SAT>_m$.

5.2.4 ALTITUDE DEPENDENCE

At least two regions with different physical conditions exist in Switzerland:

- A region below ~1000 m a.s.l. where no significant period of freezing $<SAT>_m$ and snow cover occurs
- A region above ~1000 m a.s.l. where GST is increasingly characterized by a complex interplay of insulating snow cover and the latent heat of ground moisture preventing the ground from freezing even when $<SAT>_m$ goes strongly below zero combined with strong topographical effects

As a first approximation, it is intended to linearize both conditions individually accounting for a smooth transition between the two domains. The altitude range of the transition zone corresponds to the present altitude of snow-reliability (at least 100 days of snow height usable for skiing activities between mid December and mid April) which lies at ~1200 m a.s.l. (Abegg, 1996).

The altitude dependence of GST below ~1000 m a.s.l. can generally be expressed by a linear regression line. GST decreases with altitude corresponding to the adiabatic air temperature gradient (Bendel, 1948; Powell et al., 1988), although, locally, GST values may differ from the linear trend due to surface exposure or vegetation. Analyzing our data set in the altitude range up to ~1000 m a.s.l. the following linear relationship between $<GST>_a$ / $<SAT>_a$ and absolute Z [m a.s.l.] is found:

Eq. 5-2 $$< \mathrm{GST} >_a = 13.68 - 0.005 \cdot Z$$

Eq. 5-3 $$< \mathrm{SAT} >_a = 12.13 - 0.0051 \cdot Z$$

The lapse rate for $<GST>_a$ and $<SAT>_a$ in the altitude range up to ~1000 m a.s.l. are nearly equal with an almost constant offset of ~1.6 K. Busslinger und Rybach (1999) investigated this linear dependence for Switzerland using 43 GST records (0.5 m depth) measured between 1951 and 1985. They determined a lapse rate of 4.8 K km^{-1} and a GST at sea level of 13.50 °C. This agrees well with the lapse rate as well as the GST at sea level (T_0= 13.68 °C) found in Eq. 5-2. For the Czech Republic, Šafanda (1999) reported a similar lapse rate of 4.7 K km^{-1} based on GST values extrapolated from 7 boreholes over an altitude range of 800 to 1000 m a.s.l..

Powell et al. (1988) carried out analogous work in Central Utah (USA) based on GST extrapolated from 40 boreholes. Under the climatic conditions of Utah, a much higher gradient of 7.0 K km^{-1} was found.

In contrast, the influence of snow cover and the latent heat of ground moisture is extremely complex and the temperature – altitude relationship for altitudes over 1000 m a.s.l. cannot be described by a simple linear function and requires much more sophisticated analyses (Guber et al, 2004). Although, the physical behavior is highly non-linear, we simplify this behavior for the temperature data over ~1000 m a.s.l. by a linear regression:

Eq. 5-4 $$< GST >_a = 11.42 - 0.0032 \cdot Z$$

Eq. 5-5 $$< SAT >_a = 14.34 - 0.0071 \cdot Z$$

The lapse rates for $<GST>_a$ and $<SAT>_a$ for the altitude range above 1000 m a.s.l. differ significantly from those below (Eq. 5-2 and Eq. 5-3). $<GST>_a$ above 1000 m a.s.l. decrease considerably slower with altitude than $<SAT>_a$.

For our further data treatment, a single representation is preferred. By introducing a simple 3rd order polynomial the $<GST>_a$ and $<SAT>_a$ behavior with altitude can be described by:

Eq. 5-6 $$T = a_0 + a_1 \cdot Z + a_2 \cdot Z^2 + a_3 \cdot Z^3$$

The smallest residuum values for $<GST>_a$ are found for coefficients of a_0= 15.23, a_1= $-1.08 \cdot 10^{-2}$, a_2= $+5.61 \cdot 10^{-6}$, and a_3= $-1.50 \cdot 10^{-9}$, with a standard deviation of $\pm$ 0.43 K (maximum difference of 1.34 K) and a correlation coefficient of 0.93. For the $<SAT>_a$ data (a_0= 13.47, a_1= $-1.07 \cdot 10^{-2}$, a_2= $+6.88 \cdot 10^{-6}$, and a_3= $-2.60 \cdot 10^{-9}$) a standard deviation of $\pm$ 0.44 K (maximum difference of 1.80 K) and a correlation coefficient of 0.89 were found (see Figure 5-3). The scattering of the measured data around the polynomial fit is not astonishing given local effects such as surface exposure. A 95 % confidence interval illustrates the accuracy. The increasing uncertainty with altitude results from the lower density of measurements. Clearly, similar data fits could be achieved by intersecting the above mentioned linear regression lines (Eq. 5-2 - Eq. 5-5). However, given the uncertainties from soil, vegetation an insolation the 3rd polynomial offers a more flexible representation.

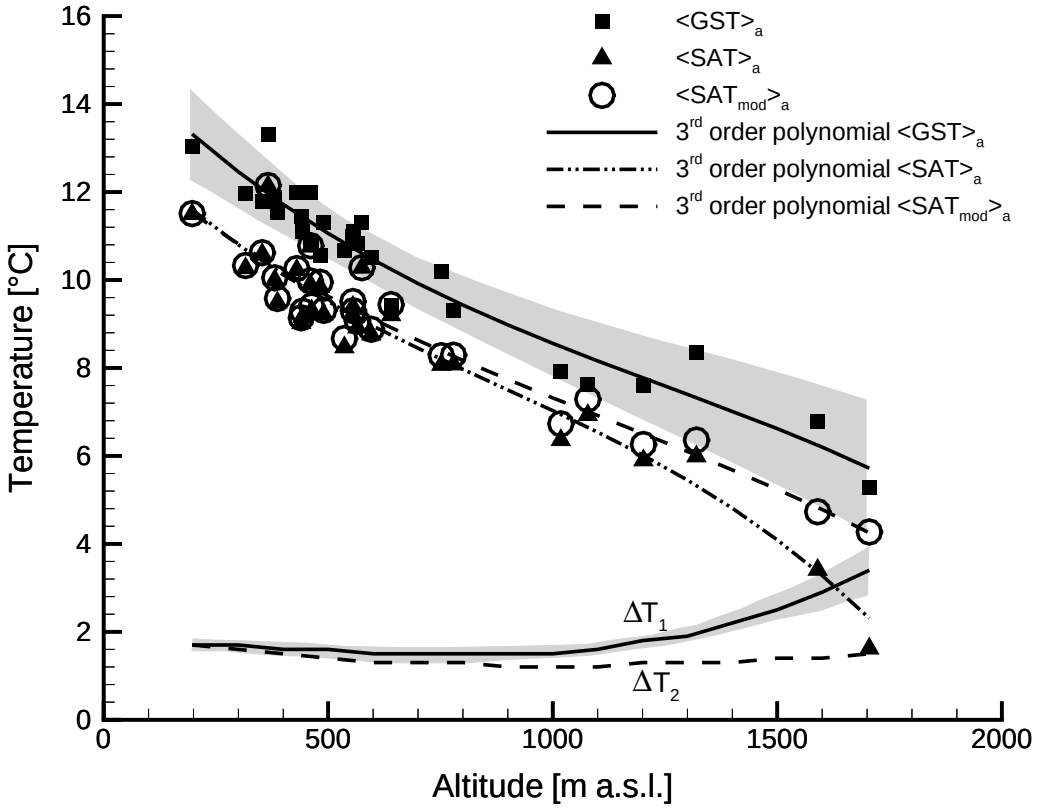

Figure 5-3: Averaged mean annual GST (<GST>$_a$ as squares), SAT (<SAT>$_a$ as triangles) and modified SATs (<SAT$_{mod}$>$_a$ as circles) values are fitted by 3rd order polynomial approaches. <GST>$_a$ and <SAT$_{mod}$>$_a$ show close to a constant offset (ΔT_1), whereas differences between <GST>$_a$ and <SAT>$_a$ (ΔT_2) increase with altitude. In addition, the 95 % confidence interval is shown in gray.

Figure 5-3 shows an increasing difference between <GST>$_a$ and <SAT>$_a$ with altitude (ΔT_1-curve). In the area below Z= 1000 m a.s.l. where most BHEs are installed nearly a constant offset between <GST>$_a$ and <SAT>$_a$ exists. Above 1000 m a.s.l. the difference becomes increasingly altitude dependent. The small (>0.1 K) oscillation between 200 and 1000 m a.s.l. which results from the differences between 3rd order polynomials can be neglected for our purposes. The 95 % confidence interval shows the decreasing accuracy with altitude, due to fewer records at higher altitudes. Between 1000 – 1500 m a.s.l., the uncertainty is <0.2 K, above, it rises to nearly 0.6 K.

As demonstrated for $<GST>_m$ and $<SAT>_m$ values before, difference between $<GST>_a$ and $<SAT>_a$ can be caused by snow cover and latent heat in the ground. To investigate the altitudes of different physical conditions more finely, a modified annual mean SAT, $<SAT_{mod}>_a$, was calculated that ignores these effects:

Eq. 5-7
$$< SAT_{mod} >= \frac{\sum_{max}(0, < SAT >_m)}{n}$$

where n is the number of measurements.

$<SAT_{mod}>_a$ is plotted in Figure 5-3 and a best fit is obtained using the coefficients a_0= 13.06, a_1= -8.56·10^{-2}, a_2= +4.01·10^{-6}, and a_3= -1.18·10^{-9}. At lower altitudes, no significant difference between $<SAT>_a$ and $<SAT_{mod}>_a$ can be established. Above 1000 m a.s.l., a difference becomes increasingly prominent due to increasing numbers of $<SAT>_m$ below 0 °C. Before correcting SAT-values the difference between $<GST>_a$ and $<SAT>_a$ shows clearly non-linear behavior (see ΔT_2-curve in Figure 5-3) above 1000 m a.s.l.. But now, the difference between $<SAT_{mod}>_a$ and $<GST>_a$ becomes nearly constant with $\Delta T_2 \approx$ 1.4 K. The $<SAT_{mod}>_a$ values eliminate successfully the effect of latent heat and possible snow cover during periods of sub-zero SATs in winter. This finding supports the observations by Lewis and Wang (1992) as mentioned in Chapter 5.2.3.

Later, in Chapter 5.3, ΔT_1-curve in Figure 5-3 will be used to calculate $<GST>_a$ from $<SAT>_a$, the latter being available for most potential locations of BHE systems. Due to low data at high altitudes, the further data treatment is restricted to the altitude range 200 – 1500 m.

5.2.5 Radiation and Effects of Surface Exposure

The dominating factor causing the scattering around the GST polynomial fit in Figure 5-3 is surface exposure. It is characterized by the amount of solar radiation received by a specific location. South-facing slopes are expected to receive the most solar radiation of all, and therefore, be the warmest. Several studies (Blackwell et al., 1980, Šafanda, 1999) have shown that the difference between measured GST and the generally considered linear, altitude-dependent fit, ΔT, is proportional to the

deviation of the local solar radiation from the annual mean radiation in any region, ΔR:

Eq. 5-8 $$\Delta T = \text{const} \cdot \Delta R$$

where const is a constant.

In this chapter we apply the concept of Eq. 5-8 to investigate $<GST>_a$ scattering from polynomial fit in regard to insolation. If a relationship between $<GST>_a$ and local sun exposure can be found, a better fitting method can be developed by using the ΔT - ΔR correlation in the polynomial approach.

Total radiation depends on direct (i.e. slope angle and orientation) and indirect (i.e. diffusive) radiation. As a first approximation, the diffusive radiation is not dependent on slope orientation, but on slope angle only (Šafanda, 1999). On cloudy days, diffusive radiation accounts for large parts of insolation. Due to the degree of cloudiness in Switzerland, annual mean diffusive radiation here is on the same order of magnitude as direct radiation (Z'graggen, 2001). For this reason we use global radiation, R, the sum of direct and diffusive radiation, for our study. From the SMI data, Z'graggen (2001) calculated global radiation as a function of the altitude dependence of direct and diffusive radiation. Moreover, he considered exposure, slope angle, horizon (as an indicator of sunshine duration) and the annual variation of Albedo (as an indicator of snow cover).

The values of global radiation at the GST stations are between 118.7 und 159.9 W m^{-2}, having a mean value of 136.2 W m^{-2} (see Table 5-1) showing the expected increase with altitude. To compare the individual stations, their global radiation values are reduced by the mean constant gradient of 1.5 W m^{-2} per 100 m (derived from the global radiation at all 72 automatic meteorological stations of Switzerland) to a reference altitude of 500 m a.s.l.. From these reduced values, we calculated the annual mean radiation and determined the local deviation for every meteorological station, ΔR.

The surface exposure to insolation (Table 5-1) is taken from Defila and Brändli (1989) and is representative for the stations and their broader surroundings. Nearly 50 % of the stations are located in lowlands (13) (see Table 5-1). The remaining stations are situated in depressions (1), on east-facing slopes (2), in canyon-type valleys (4), on south-facing slopes (4), and on local elevations (5). Unfortunately, no

measurements on north-facing slopes exist, but behavior analogous to that measured in the canyon-type valleys can be expected. Since none of the meteorological stations represents a steep exposure, but rather a locally flat terrain in a pronounced topographic setting, no conclusions can be made for extreme south- and north-facing slopes. However, the stations reflect common locations for possible BHEs.

Figure 5-4 shows the deviation of the annual mean values from the 3rd order polynomial trend, ΔT, as a function of the deviation of local solar radiation from annual mean radiation, ΔR. Theoretically, all locations with the same exposure should be found in the same quadrant. Thus, south-facing slopes should have a higher global radiation resulting in higher GST values than expected from the polynomial trend. In Figure 5-4 two south-facing slopes show the expected correlation, but two others behave differently. Despite increased radiation, one location has a slightly negative temperature deviation, and the global radiation at the fourth location is even smaller than the expected average. An analogous result is observed for the four stations situated in a canyon-type valley. Because of the high horizon, we expected in these valleys a shorter sunshine duration, which should result in lower radiation and temperature values. However, only one station shows the expected correlation. Two locations have clearly higher global radiation than the expected average. Generally a low ΔT–ΔR-correlation (correlation coefficient of 0.08) is shown by the fact that all four quadrants are occupied by ΔT data points and three quadrants with nearly equal density.

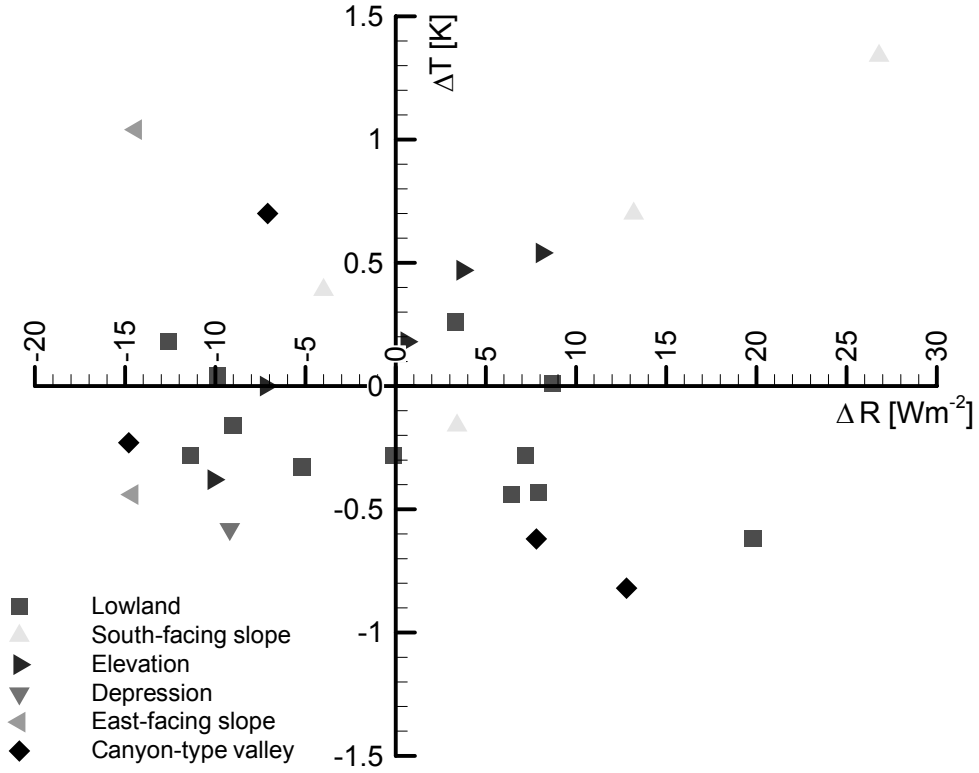

Figure 5-4: The difference of $<GST>_a$ to the polynomial trend, ΔT, is plotted as a function of the deviation of local solar radiation from the annual mean radiation, ΔR, for all meteorological stations. There exists no dependence on surface exposure.

We could not establish a general correlation between GST and solar radiation. A reason for the missing correlation might be spatially fast-varying meteorological conditions like degrees of cloudiness which result in no simple linear relationship. A south-facing slope does not inevitably receive much more global radiation and therefore does not always have a higher GST than other locations. For example, the reduced global radiation on a south-facing slope (Station-no. 17) can be 13 % lower than in a canyon-type valley (Station no. 21). Because of the relatively high number of cloudy days on the south-facing slope compared to the canyon-type valley (Station-no. 17 had 67 and Station-no. 21 had 55 days), global radiation is lower there than in the valley.

The current data base does not allow a more sophisticated study. Long term measurements at various exposures would be especially helpful. For our purposes, a standard deviation of <0.5 K achieved by the $<GST>_a$ polynomial fit (see above) is sufficient. Moreover, the uncertainties documented by the 95 % confidence interval

(Figure 5-3) sufficiently include the influences of various local effects, such as surface exposure.

5.3 RELATIONSHIP BETWEEN GST AND SAT

For accurate modeling of BHE systems, a regional map of GST distribution is necessary but the available data are insufficient for much detail. At higher altitudes especially, the density of stations is low. SAT measurements, however, are more frequent and generalized SAT models have already been generated (Meteotest, 1995, Zimmermann and Kienast, 1995, Z'graggen, 2001). Using the earlier derived relationship between $<GST>_a$ and $<SAT>_a$ (see Chapter 5.2.4), we generated a regional $<GST>_a$ map from the $<SAT>_a$ distribution and present verification from independent data.

5.3.1 GST MAP OF SWITZERLAND

Based on both averaged annual mean SAT values measured at all the meteorological stations (112 stations) from 1984 to 1994 and local atmospheric lapse rates, Z'graggen (2001) calculated $<SAT>_a$ on a 250 m grid covering Switzerland. The $<SAT>_a$ at the meteorological stations was reduced on to a level of 1000 m a.s.l. using the respective lapse rate. Then, $<SAT>_a$ for every grid point was calculated by the 2D-Kriging-method and corrected for original altitude. Finally, surface exposure and isolated "cold-air lakes" in the Alpine environment were taken into account. For 90 % of all stations the difference between the measured and calculated $<SAT>_a$ is clearly <1 K: sufficient for analyzing regional phenomena. However, small-scale analysis would require more local climate stations. The $<SAT>_a$ map is available as a digital data set and can be processed by GIS-programs.

Applying the relationship between $<GST>_a$ and $<SAT>_a$ defined by Eq. 5-6 and the coefficients at the top of page 77, we converted the $<SAT>_a$ map into a $<GST>_a$ map. Due to the decreasing accuracy of that relationship with altitude (see 95 % confidence interval in Figure 5-3) and the different impact of recent warming at higher altitudes (see Chapter 5.2.2), we limit the $<GST>_a$ map to regions below 1500 m a.s.l.. This choice is reasonable as it is the most populated area with modestly undulated topography. Figure 5-5 shows the first GST map of Switzerland.

It represents a regional distribution and does not account for local effects. Because both the relationship between $<GST>_a$ and $<SAT>_a$ and the $<SAT>_a$ map itself are based on SMI data, we verified our $<GST>_a$ map using independent GST values extrapolated from boreholes.

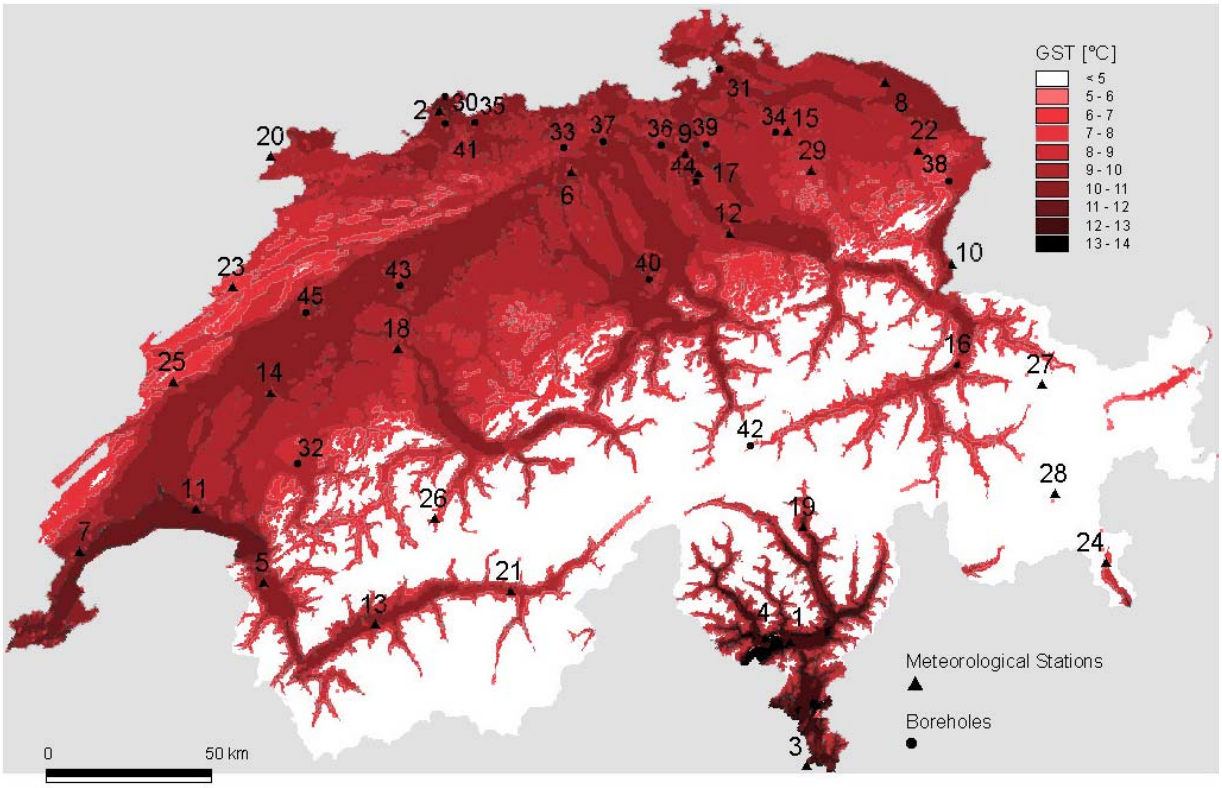

Figure 5-5: First $<GST>_a$ map of Switzerland generated from the $<SAT>_a$ map of Z'graggen (2001) using the relationship between $<GST>_a$ and $<SAT>_a$ developed in Chapter 5.2.4. Areas above 1500 m a.s.l. appear in white. The notation corresponds to that in Table 5-1 and Table 5-2.

5.3.2 Determining GST with Borehole Data

Schärli and Kohl (2002) compiled data from 167 boreholes in Switzerland and neighboring areas. Continuous temperature measurements were taken in about 30 boreholes, mostly for geothermal purposes. We explicitly intended to treat all borehole logs by extrapolating the mean annual GST using linear regression. For our investigation, data sets obviously influenced by ground water circulation were excluded for this extrapolation. The remaining 16 borehole logs have sufficient resolution within the upper 100 m. The boreholes are listed in Table 5-2, and their areal distribution is shown in Figure 5-5. Most are located in northeast Switzerland between 300 and 1000 m a.s.l..

To eliminate transient daily and annual effects that may influence the linear extrapolation, the upper 20 m are ignored. From steady-state diffusive considerations, the uncertainty in the extrapolated temperature along this depth range can be estimated to be a maximum of 0.2 K, assuming variations in thermal conductivities of 2.0 W m^{-1} K^{-1} in the top 0.5 m soil layer. Note that this upper part influences the operation of a BHE only marginally, and partly negative effects in winter are eliminated by insulation.

A further source of transient effects is global warming. The GST map represents the averaged annual mean temperature ($<GST>_a$) distribution from 1981 to 1999, but borehole data may be measured at a different period. To elucidate how transient GST variation affects our borehole data treatment, a 1 K temperature interval was stipulated to occur instantaneously 100 years ago. Using the 1D solution after Carslaw and Jaeger (1959), the temperature perturbation is calculated as:

Eq. 5-9
$$T = A_0 \cdot \mathrm{erfc}\left(\frac{z}{2\sqrt{\kappa \cdot t_i}}\right)$$

with A_0 representing the amplitude of GST change, z the depth, κ the thermal diffusivity and t_i the period of the GST change. Figure 5-6 shows that a linear regression from data below 20 m would result in a maximum 0.1 K deviation from the effective value. The assumed 1 K step function somewhat overestimates the error since climatic warming occurs rather linearly. Summing up all transient effects, we expect the accumulated error to be about 0.3 K.

Table 5-2 lists the $<GST>_a$ values derived from each temperature log and summarizes the relevant borehole parameters. The temperature gradients, ∇T, are between 21.7 and 53.6 K km^{-1} and correspond well to the heat flow map of Switzerland (Medici and Rybach, 1995). The high values at borehole no. 33 (Densbueren) and borehole no. 37 (Hausen), for example, correlate with the heat flow anomaly in the northwest of Switzerland (Pfister and Rybach, 1996). In Figure 5-7 the extrapolated values are illustrated, using a temperature notation reduced by the corresponding temperature gradient, ∇T. The minimum $<GST>_a$ value is 6.6 °C at the Alpine station of Rueras (borehole no. 42). In the Alpine

Foreland the values are between 7.9 °C and 12.3 °C and lie within the range measured at the meteorological stations (see Table 5-1).

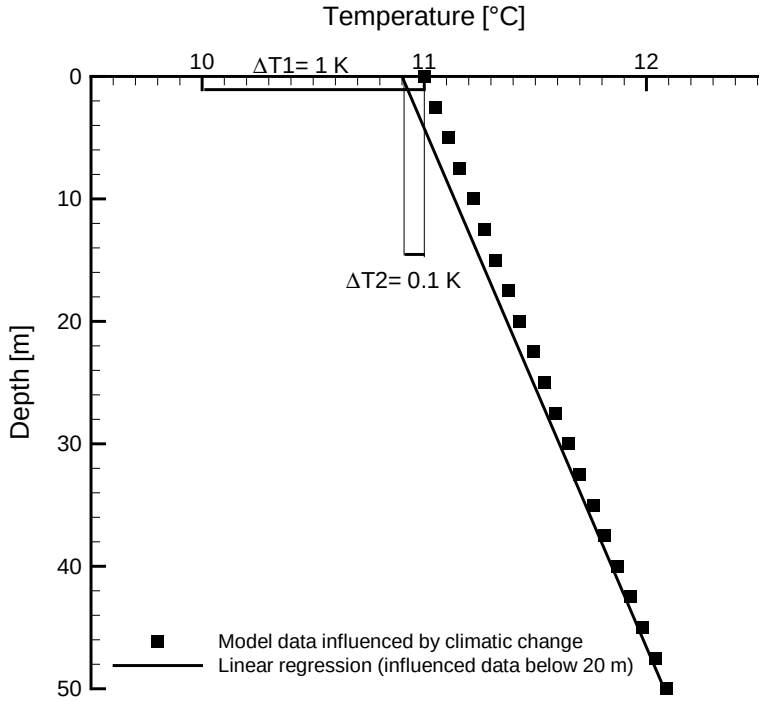

Figure 5-6: Model of the temperature distribution in the subsurface 100 years after a GST increase of ΔT_1= 1 K. The $<GST>_a$ extrapolated from the model data down to 100 m by ignoring the first 20 m is ΔT_2= 0.1 K lower than the effective value.

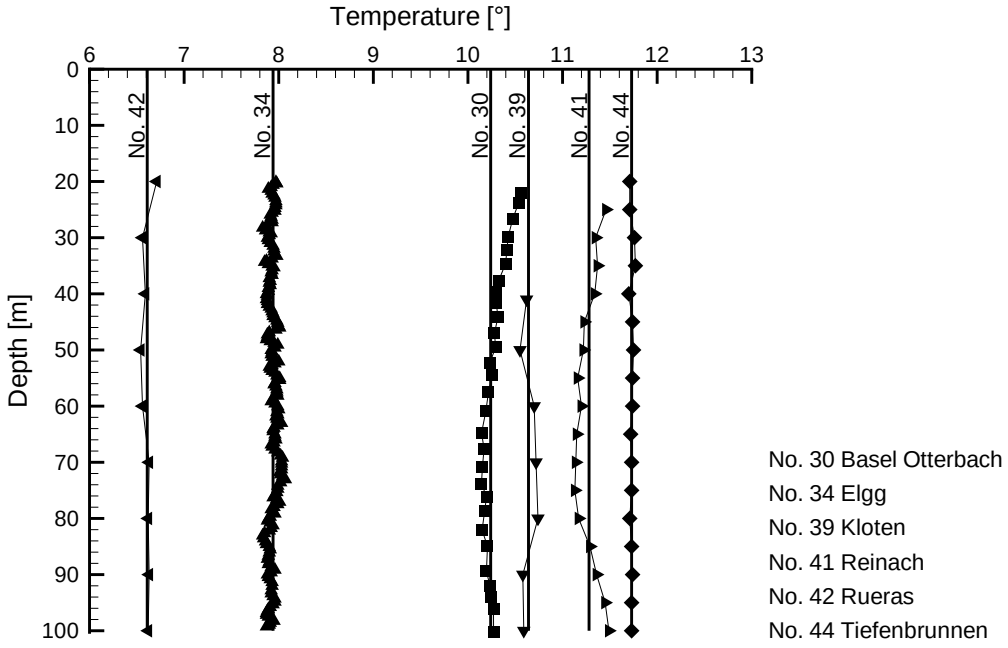

a)

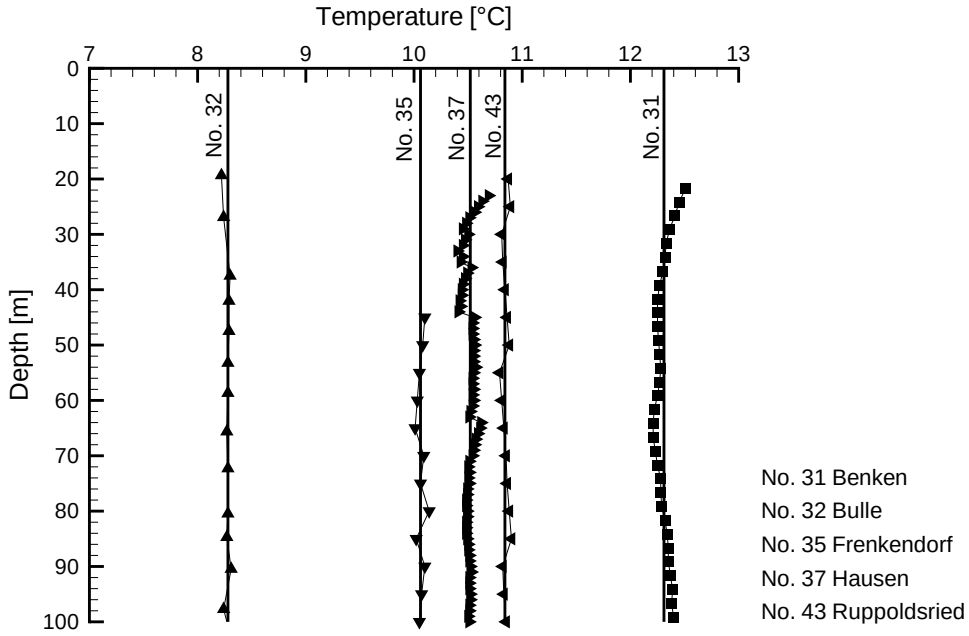

b)

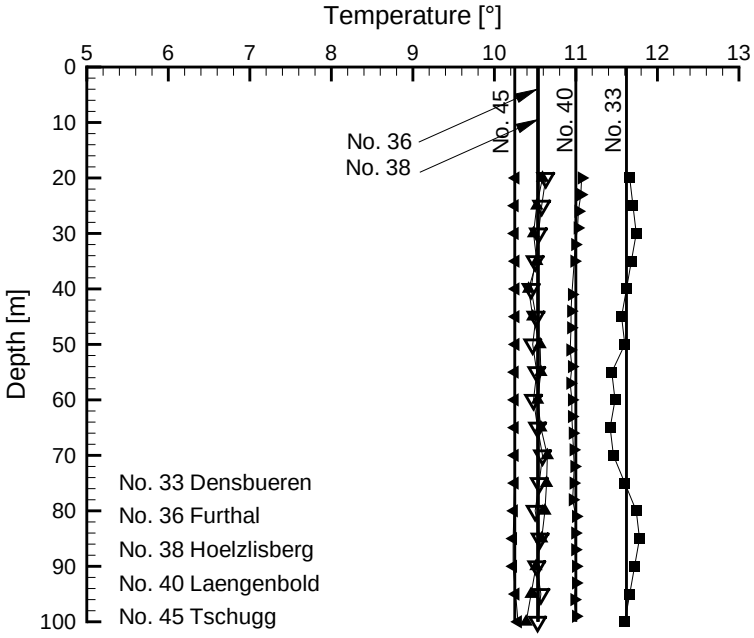

c)

Figure 5-7: Borehole data and the corresponding extrapolated <GST>$_a$ values. The borehole data are reduced with the corresponding local temperature gradient (T_{red}= T(z) – $\nabla T \cdot z$). The notation corresponds to that in Table 5-2.

Table 5-2: Comparison of extrapolated $<GST>_a$ from boreholes and the calculated $<GST>_a$ from the $<GST>_a$ map. Additionally, altitude, interval of measurement, coefficient of correlation, and temperature gradient ∇T are listed. The spatial distribution is shown in Figure 5-5.

No.	Borehole	Altitude	Interval of extrapolation	Interval of measurement	Data fit (R^2)	Gradient ∇T	Extrapolated $<GST>_a$	$<GST>_a$ from GST map	Difference ΔT_b
		[m a.s.l.]	[m]	[m]	[-]	[K km^{-1}]	[°C]	[°C]	[K]
30	Basel Otterbach	253	20 - 100	2.2	0.996	45.0	10.2	11.5	1.3
31	Benken	404	22 - 100	3	0.989	29.2	12.3	10.7	-1.6
32	Bulle	765	27 - 100	6	0.999	34.0	8.3	10.2	1.9
33	Densbueren	516	20 - 100	5	0.993	52.7	11.6	10.3	-1.3
34	Elgg	620	20 - 100	0.4	0.998	39.9	7.9	10.0	2.1
35	Frenkendorf	305	45 - 100	5	0.998	44.5	10.1	11.3	1.2
36	Furthtal	420	20 - 100	5	0.993	34.8	10.5	10.8	0.3
37	Hausen	380	23 - 100	1	0.998	53.6	10.5	10.8	0.3
38	Hoelzlisberg	573	20 - 100	5	0.996	29.6	10.5	10.6	0.1
39	Kloten	444	41 - 100	10	0.981	25.5	10.6	10.6	0.0
40	Laengenbold	418	20 - 100	3	0.989	21.7	11.0	10.9	-0.1
41	Reinach	292	25 - 100	5	0.947	22.7	11.3	11.4	0.1
42	Rueras	1412	20 - 100	10	0.997	33.3	6.6	7.3	0.7
43	Ruppoldsried	480	20 - 100	5	0.999	36.9	10.8	10.7	-0.1
44	Tiefenbrunnen	408	20 - 100	5	0.999	22.2	11.7	10.8	-0.9
45	Tschugg	465	20 - 100	5	1.000	36.1	10.3	10.7	0.4
								Standard deviation	$\pm$ 1.0

To validate the new $<GST>_a$ map, the value of each borehole location was compared to the corresponding map value. The differences between the $<GST>_a$ map and the extrapolated $<GST>_a$, $\Delta T_{b\_<GST>a}$, are shown in Table 5-2. The standard deviation is ± 1.0 K, with $\Delta T_{b\_<GST>a}$ generally below 1 K and in the range of the $<SAT>_a$ map itself. This result strongly confirms our procedure since independent $<GST>_a$ values are well approximated by the $<GST>_a$ map. Only two locations show deviations of about 2 K (borehole no. 33, Bulle, and borehole no. 34, Elgg).

We then considered the differing quality of the borehole data sets. The vertical resolution (based on the interval of measurement; see Table 5-2) and the quality of the measurements (based on the regression line's coefficient of correlation; see Table 5-2) were individually weighted with no impact on the above results.

5.3.3 Influence of Extrapolated GST on Determining GST with Meteorological Data

As shown in Figure 5-5 the 16 boreholes are mainly located in northeastern Switzerland and thus do not give a larger regional coverage. Therefore, combining analysis of the $<GST>_a$ values from the meteorological stations and the extrapolated $<GST>_a$ values cannot generate a regional map like that for $<SAT>_a$. However, to estimate altitude dependence more exactly, we analyzed the extrapolated $<GST>_a$ values with the SMI data. All 45 values are plotted in Figure 5-8 as a function of altitude. Besides the polynomial fit for all data and its confidence interval, we also show the polynomial trend of the meteorological data. The coefficients of the polynomial fit for all data are $a_0 = 12.05$, $a_1 = 3.69 \cdot 10^{-4}$, $a_2 = -6.18 \cdot 10^{-6}$, and $a_3 = 2.30 \cdot 10^{-9}$. The use of a 3rd order polynomial causes artificial inflection points at lower and higher altitudes.

Compared to the polynomial of the meteorological data, the fit of all $<GST>_a$ values is clearly poorer within the altitude range of 200 to 500 m a.s.l. and its trend is flatter. Otherwise the fit of all data corresponds to that of the meteorological data. The newly calculated standard deviation is ± 0.81 K and the correlation coefficient of 0.82. As shown by the 95 % confidence interval, the uncertainty of the trend remains at higher altitudes.

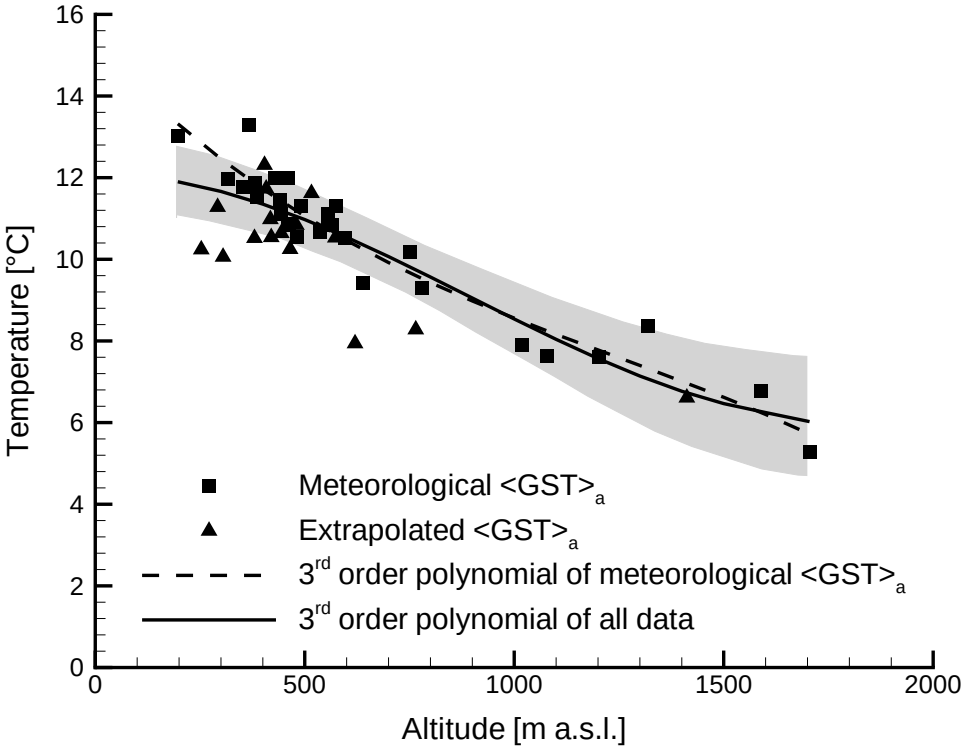

Figure 5-8: Determination of the altitude dependence considering all available meteorological $<GST>_a$ (squares) and extrapolated $<GST>_a$ from boreholes (triangles) values. Additionally, the 95 % confidence interval is shown in gray.

5.4 CONCLUSIONS

A productivity analysis of low enthalpy resources requires the prediction of GST distribution. For that purpose, two different methods using meteorological data have been applied to Switzerland's most populated area, one characterized by modest undulation. The available data set allows no prediction for areas of extreme surface exposure and rough topography.

It is generally considered that surface exposure to insolation at any location strongly influences GST distribution. Contrary to previous publications (Blackwell et al., 1980, Šafanda, 1999), our analysis of SMI's 29 high-precision measurement records shows no correlation between GST and surface exposure. Apparently, the Blackwell et al. (1980) approach doesn't fit Swiss locations due to strongly varying meteorological conditions over short distances. These statements are based on ground covered by vegetation, mainly in the Alpine Foreland, and ignore conditions at extremely exposed locations and uncovered rocks in high Alpine areas.

After our data analysis, we established differences in the recent GST history of the Alpine Foreland and truly Alpine environment. The latter seems to be more strongly influenced by global warming. The partly missing snow in the winter may cause a more pronounced change of the climatic conditions in the Alps than in the Alpine Foreland.

Based on a non-linear fit, we formulated a new relationship by comparing annual mean values of GST and SAT at meteorological stations. We have found three zones of different $<GST>_a$ -$<SAT>_a$ dependencies: In the altitude range between 200 and ~1000 m a.s.l., the difference between $<GST>_a$ and $<SAT>_a$ is nearly constant (~1.6 K). Above that interval, this difference increases. This effect could be related to the influence of sub-zero $<SAT>_a$.

Using this new formulation we converted an existing SAT map into the first $<GST>_a$ map of Switzerland. Verifying this new map with $<GST>_a$ values extrapolated from boreholes demonstrated a high reliability: the $<GST>_a$ map estimates $<GST>_a$ values up to an altitude of 1500 m a.s.l. very well. We found a standard deviation of ± 1.0 K, with a maximum deviation of 2 K. This is in the range of the SAT map itself; however, small-scale phenomena cannot be resolved without more GST measurement stations.

As long as the density of GST stations is too low for regional extrapolation, a country-wide GST map can be derived only from analyzing an extensive SAT data set. However, the presented $<GST>_a$ map of Switzerland, by which $<GST>_a$ can easily be determined in practice, helps us to design BHE systems better.

6. DATA ANALYSES II: THERMAL RESPONSE TESTS

Beside the GST, the ground thermal conductivity largely determines the dimensions of the BHE installation. Usually, estimated values are sufficient for single house applications and dimensioning is done by experience. For large systems (>10 BHEs) however, knowledge the thermal conductivity constrains the numbers of BHEs, and therefore costs, required for the energy needs of the building.

Focusing on different influences on the analysis of thermal responses tests such as test duration, BHE length, stratified subsurface and groundwater flow, analytical and 3D numerical models will be compared (Signorelli et al., submitted to Geothermics). The general procedure is to use the 3D numerical model to calculate various test cases and then utilize the temperature response as synthetic data for the more conventional analytical thermal response analysis. This comparison should quantify the error introduced by the generally applied line source analysis. Finally, a numerical assessment of a real data set will be present with a comparison to a line source model.

6.1 INTRODUCTION

The principle of thermal response tests was first proposed by Morgensen (1983) and is based on an infinite line source model. In 1995, the first mobile measurement devices were introduced in Sweden (Eklöf and Gehlin, 1996) and in the USA (Austin, 1998); since then, the method has developed and spread to several other countries (Gehlin, 2002). This experimental methodology (e.g.: Gehlin 2002, Austin et al. 2000, Eugster and Laloui, 2002) attempts to constantly heat a fluid circulated through a BHE ready to operate and to measure the BHE inlet and outlet temperature response. By evaluating the recorded temperatures versus time, an estimation of the average thermal conductivity in the vicinity of the BHE is obtained. To estimate in-situ thermal conductivity, the temperature evolution during the recovery period after the response test is sometimes also measured and evaluated (Fujii et al., 2002). These data are less noisy than the data measured during the test. However, additionally measuring of the slowly recovering thermal field would strongly increase the cost of such a response test. The thermal response test set-up is illustrated in Figure 6-1.

The advantage of response tests is the integration of the underground thermal properties along the whole length of a BHE, including groundwater and backfilling material, providing therefore a so called “effective” and not the “real” thermal conductivity defined under strict heat-conduction assumptions. Laboratory measurements alone may lead to different values since they cannot correctly take into account groundwater flow and water filled cracks and pores. However, to use this estimated “effective” thermal conductivity as the representative value for dimensioning purposes may be dangerous in some cases, especially in advective dominated areas. As Eq. 2-14 shows, advective and conductive processes are considered by two different physical terms. If the subsurface regime is advectively dominated, these tow processes cannot simply be described by one single parameter.

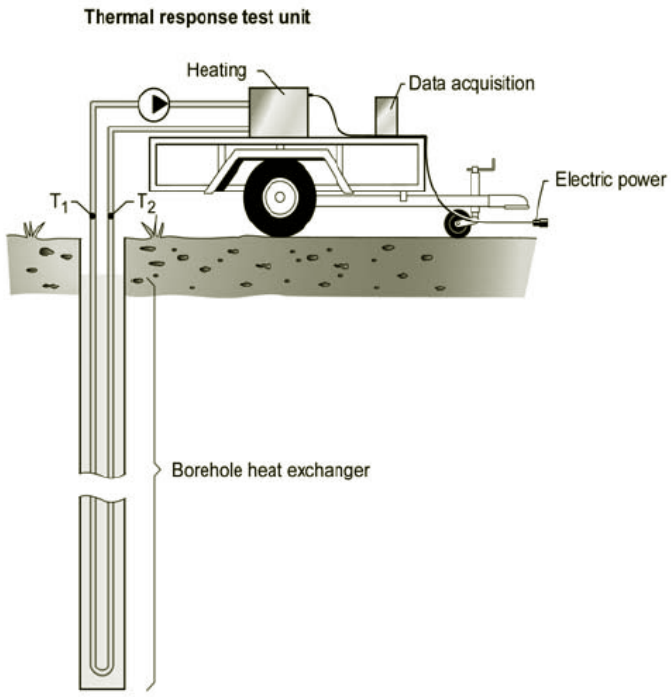

Figure 6-1: Thermal response test set-up (Gehlin, 2002).

Several mathematical models have been proposed to calculate the thermal conductivity from the measured temperature response, either with analytical or numerical solutions of the heat conduction equation. Analytical models, such as the line source or the cylindrical model, are based on simple assumptions regarding the geometry of the borehole and heat exchanger and are therefore fast and easy to handle. Recently, numerical techniques (e.g. Yavuzturk et al. 1999, Shonder and

Beck, 1999) have become more common because they can account for time-varying effects such as variations in heat injection and specific borehole geometries. However, the additional model parameters make the interpretation more complex and time-consuming. While the analytical line source model is a simplification of the actual test, it is the most applied in practice and its accuracy in determining in-situ thermal conductivity is generally accepted (Schärli and Rybach, 2002). This study will show that a high accuracy is only possible under specific conditions.

The accuracy of the thermal response test depends largely on the duration of the testing interval, since the initial data may represent the response of the BHE itself. The optimum duration is a topic of on-going discussion (Austin, 1998, Gehlin, 1998, Smith and Perry, 1999), because test length is related to test cost. Furthermore, complex geology and hydrology can influence the evaluation. In most evaluations of a thermal response test one assumes the underground to be homogenous with a constant heat transfer rate along a BHE. However, in reality, the heat transfer from the fluid to the ground might be highest near the surface due to the natural temperature gradient and in the cases of geologic heterogeneities a specific layer may dominate. An additional possible factor is the influence of groundwater flow on the thermal response test. Groundwater flow generally improves the efficiency of heating systems; however, it can lead to significant heat loss in subsurface heat storage systems. These different factors will be investigated in the following chapters.

6.2 METHODS OF ANALYSIS

Here, we describe the analytical and numerical procedures which will be used in the analyses, comprising both synthetic and real data.

6.2.1 ANALYTICAL MODEL

The most widely used analytical analysis procedure is the line source model. It is based on Kelvin's line-source theory and has been applied to simulated BHEs (Ingersoll and Plass, 1948; Sanner, 1992) for decades. Mogensen (1983) proposed this method to evaluate thermal response tests. The approach adopts the analytical solution for the response to an infinite constant line source within a homogeneous, isotropic infinite medium. Assuming negligible vertical heat flow along the BHE and

constant lateral heat flow, the temperature field around the BHE is only dependent on time, t, and radial distance, r, from the borehole axis. This corresponds to the approach used in EED (see Chapter 3.3). However, a different equation for the temperature field is chosen using the so-called exponential integral E_1 (Carslaw and Jaeger, 1959):

Eq. 6-1
$$T(r,t) - T_0 = \frac{q_{spez}}{4\pi \cdot \lambda} \int_{\frac{r^2}{4\kappa t}}^{\infty} \frac{e^{-u}}{u} du = \frac{q_{spez}}{4\pi \cdot \lambda} E_1\left[\frac{r^2}{4\kappa t}\right]$$

T_0 is the undisturbed ground temperature, q_{spez} the specific heat injection rate, λ the thermal conductivity, κ denotes the thermal diffusivity of the ground.

E_1 can be approximated if the radius of the thermal front has penetrated the surrounding rock beyond the borehole wall and the effects of the BHE can be neglected. This simplified E_1 is defined as:

Eq. 6-2
$$E_1\left[\frac{r^2}{4\kappa t}\right] = -\gamma - \ln\left[\frac{r^2}{4\kappa t}\right] - \sum_{n=1}^{\infty} (-1)^n \frac{(\frac{r^2}{4\kappa t})^n}{n \cdot n!} \cong \ln\left[\frac{4\kappa t}{r^2}\right] - \gamma$$

where γ represents the Euler constant [0.5772…]. The maximum error of this simplification is less than 10 % for the time criterion $t_c \geq \frac{5 \cdot r^2}{\kappa}$.

Thus, the temperature at the borehole wall ($r=r_b$) can be defined by:

Eq. 6-3
$$T(r = r_b, t) = \frac{q_{spez}}{4\pi \cdot \lambda}\left[\ln\left(\frac{4\kappa t}{r_b^2}\right) - \gamma\right] + T_0 \qquad \text{with } t_c \geq \frac{5 \cdot r_b^2}{\kappa}$$

Introducing a thermal borehole resistance between the fluid and the borehole wall, R_b, the average fluid temperature of the circulation fluid, $\overline{T}$, as a function of time can be written as:

Eq. 6-4
$$\overline{T}(t) = T(r = r_b, t) + q_{spez} \cdot R_b = \frac{q_{spez}}{4\pi \cdot \lambda} \ln(t) + q_{spez} \cdot \left[R_b + \frac{1}{4\pi \cdot \lambda}\left(\ln\left(\frac{4 \cdot \kappa}{r_b^2}\right) - \gamma\right)\right] + T_0$$

For constant q_{spez}, the last two terms become constant and Eq. 6-4 can be defined as a simple linear relation:

Eq. 6-5 $$\overline{T}(t) = \text{const} \cdot \ln(t) + m$$

where const and m are constants, with $\text{const} = \frac{q_{spez}}{4\pi \cdot \lambda}$ and $m = q_{spez} \cdot \left[R_b + \frac{1}{4\pi \cdot \lambda} \left(\ln\left(\frac{4 \cdot \kappa}{r_b^2} \right) - \gamma \right) \right] + T_0$.

As shown in Chapter 3.3.2, $\overline{T}$ can be assumed to correspond to the average between the inlet (T_{in}) and outlet temperature (T_{out}) of the circulating fluid:

Eq. 6-6 $$\overline{T} = \frac{T_{in} + T_{out}}{2}$$

Now, if the evolution of the mean temperature $\overline{T}$ is plotted versus the natural logarithm of the time curve, the line source model delivers the thermal conductivity, λ_{LS}, by:

Eq. 6-7 $$\lambda_{LS} = \frac{q_{spez}}{4\pi} \cdot \frac{\ln(t_2) - \ln(t_1)}{\overline{T}(t_2) - \overline{T}(t_1)}$$

For the following analytical evaluation, λ_{LS} is not only estimated from t_1 and t_2, but all temperature points between t_1 and t_2 are used to calculate the regression. q_{spez} is realized during a field test with an electric heater of a few kW power. The higher the energy loss in the subsurface is, the higher is λ_{LS}. All the following λ_{LS} are calculated from the simulated temperature response of a numerical model with a specific thermal conductivity, λ_{num}.

6.2.2 NUMERICAL MODEL

Numerical models of thermal response tests allow a more detailed representation of the borehole (geometry and thermal properties) and can account for variation in the heat transfer rate. The most commonly used numerical models are based on parameter estimation techniques with 1D finite difference borehole models (Shonder

and Beck, 1999) and with 2D numerical finite volume models (Yavuzturk et al., 1999, Spitler et al., 1999, Austin et al., 2000).

For the first time FRACTure will be used to analyze thermal response tests. To this end, we apply parameter estimation on a single independent variable: the subsurface thermal conductivity, λ. This requires that all other input parameters are specified in advance. The geometry of the BHE and the thermal properties of the grout are generally known. However, the tube locations inside the borehole are normally not known, the borehole geometry must be assumed and may differ from the actual one, but Austin et al (2000) and Bassetti (2003) show that even significant variation in the U-tube shank spacing only yields small changes in the thermal conductivity prediction. The general procedure is to minimize the difference between the measured records and the simulated results by systematic variation of thermal conductivity from which a best estimate of the thermal conductivity may then be found. The objective function for this optimization, the sum of the squares of the errors (SSE) between the experimental and the simulated results, is given by:

Eq. 6-8
$$SSE = \sum_{n=1}^{N} (T_{meas} - T_{sim})^2$$

where N is the total number of measured data points, T_{meas} the measured and T_{sim} the simulated temperatures. It is customary to minimize the square difference SSE.

6.3 SENSITIVITY ANALYSIS

Before investigation an experimental in Chapter 6.4, sensitivity analysis based on synthetic data will be discussed in this chapter. First the used FE mesh and the method applied for generating the synthetic data is described. Note that the same FE mesh will be used in evaluating the experimental data in Chapter 6.4. These synthetic data are used to determine the sensitivity of the line source model to test duration, borehole length and heterogeneous subsurface.

6.3.1 BOREHOLE GEOMETRY AND NUMERICAL DISCRETIZATION

The FE mesh generation procedure follows the findings in Chapter 3.2. The mesh is generated according to the test performed in a 160 m deep borehole (see Table 6-1). Here, the BHE is equipped with spacer-separated 40 mm pipes. Figure 6-2 shows

the implementation of this BHE geometry with the four separated tubes grouted in the center of the borehole. The complete mesh is constructed from 34 horizontal layers and consists of ~86'000 nodes. The spatial resolution used corresponds to that of model run M_2 in Chapter 3.2.4 and the time step length is dt= 1 hour.

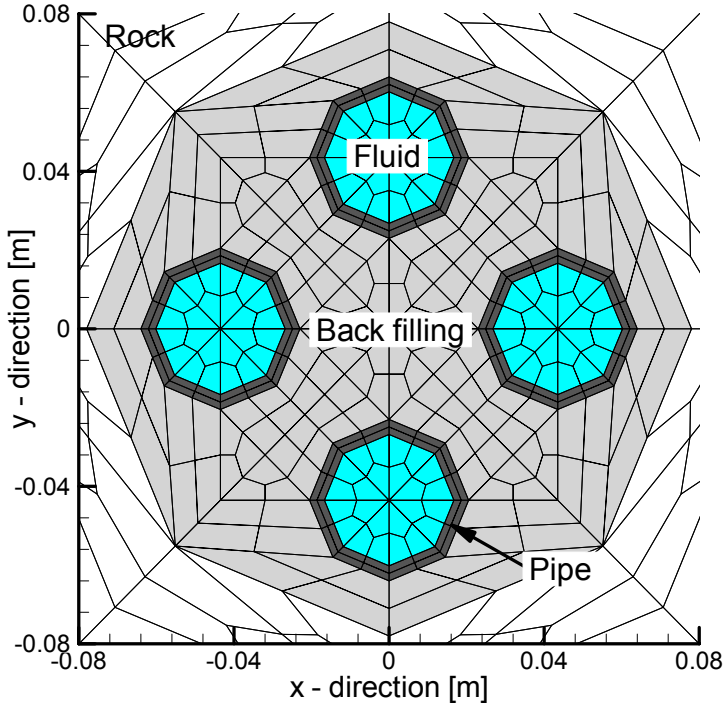

Figure 6-2: Discretization of the BHE with the four pipes in the center of the BHE and the backfilling.

For the following simulations, constant surface temperature of 10 °C and basal heat flow of 90 mW m^{-2} are assumed, resulting in a temperature gradient along the BHE. The presence of a temperature gradient along the BHE violates the line source assumptions. As input parameters, the thermal conductivity, λ, and the heat capacity, ρc_p, of the tubing wall are typical values for polyethylene (λ_{Pipe}= 0.4 W m^{-1} K^{-1}, ρc_{pPipe}= 1.62 MJ m^{-3} K^{-1}) and for the grout material values for standard bentonite mixture are assumed (λ_{Grout}= 0.8 W m^{-1} K^{-1}, $\rho c_{p\ Grout}$= 2.0 MJ m^{-3} K^{-1}). For all following sensitivity analyses, the thermal conductivity of rock matrix in the numerical model, λ_{num}, is set 3 W m^{-1} K^{-1}, and the heat capacity, $\rho c_{p\ num}$ is assumed to be 2.5*10^6 MJ m^{-3} K^{-1}.

Based on these model conditions, the response of the mean fluid temperature is then simulated by FRACTure assuming a test duration of 200 hrs and a constant heating power of 9 kW. From these synthetic temperature data, the thermal

conductivity, λ_{LS}, is evaluated by applying the line source model for different data intervals according to Eq. 6-7: λ_{LS}, the thermal conductivity calculated by the line source approach, is determined either for fixed end time, t_E (= end of the considered time period), and variable starting time, t_0 (= start of the considered time period), or for fixed t_0 and continuously increasing t_E (i.e. increasing length of the data interval analyzed). Except in Figure 6-3, we illustrate our results according to the second method (generally applied method in practice) with t_0= 10 hrs (~t_c) and continuously increasing end time from t_E= 11 hrs to t_E= 200 hrs. Thus, the first point in a figure is the estimation for the data interval between 10 - 11 hrs, and the last one is the value for the interval between 10 - 200 hrs.

6.3.2 Testing the Line Source Approach

Two facts in our general numerical model setup violate the line source assumption: The temperature gradient along the BHE and the finite length of the BHE in contrast to an infinite line source. These two facts also characterize the real test conditions. However, first the reliability of the line source approach is tested. Therefore, a model run is set up, which fulfills the requirement of the line source model, by ignoring the boundary conditions at surface and at bottom of the FE mesh – imposing no temperature stratification - and by extending the FE mesh only over the depth range of a BHE - ignoring the finite source length. The response test is then performed for 200 hrs and λ_{LS} is estimated for fixed t_E= 200 hrs and t_0 varying continuously from t_0= 1 hrs to t_0= 199 hrs. Thus, the first point in Figure 6-3 is the estimation for the data interval between 1 and 200 hrs, and the last one is the value for the interval between 199 and 200 hrs. This evaluation method progressively reduces the influence of the borehole. Figure 6-3 illustrates that the effect of the borehole itself is clearly visible in the first hours, resulting in too low values. After ~30 hrs, the evaluation progressively approaches a constant value. This analysis of synthetic data shows that under ideal conditions the line source approach can yield the proper thermal conductivity.

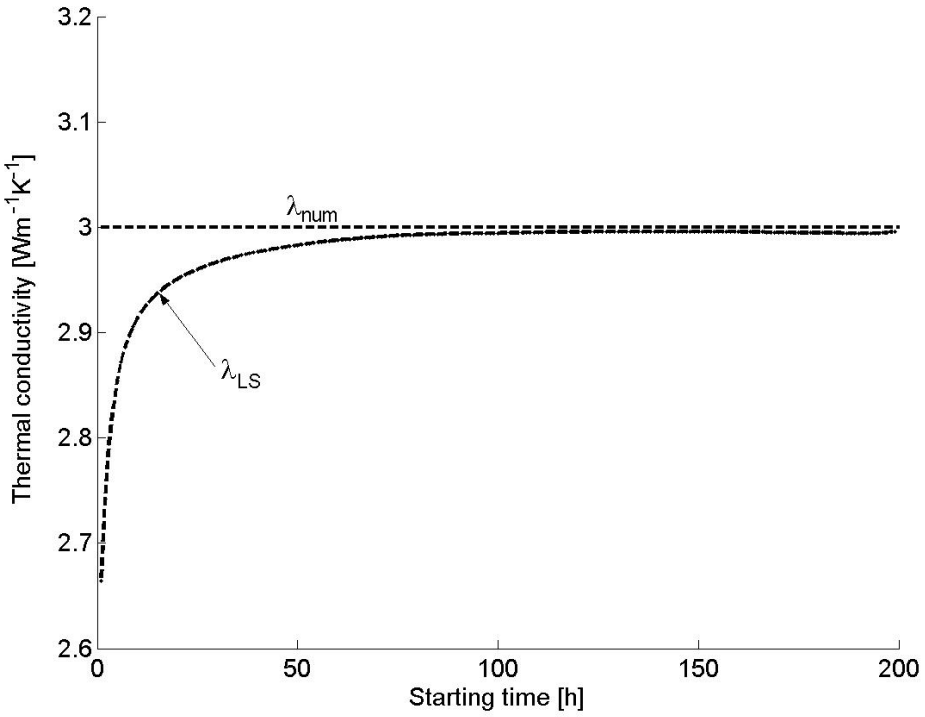

Figure 6-3: Thermal conductivity evaluated by the line source model, λ_{LS}, for the FE mesh used. The end point of the different evaluated data intervals is fixed at t_E= 200 hrs and the starting point is varied from t_0= 1 hr up to 199 hr which is shown on the x - axis. The influence of the borehole itself progressively reduces for later starting points of evaluation.

6.3.3 DURATION OF MEASUREMENT

The measurement duration of a thermal response test is an on-going discussion. In literature the suggested duration varies between 60 (Gehlin, 1998), 50 (Austin et al., 2000) and 12 – 20 hrs (Smith and Perry, 1999). Since the evaluation by line source model is extremely sensitive to single data points, Gehlin and Hellström (2003) recommend avoiding the evaluation of data intervals shorter than 30 hrs. However, it is difficult to define the data interval needed for an accurate evaluation from experimental data. Austin (1998) and Witte et al. (2002) show that small temperature variations, often caused by unstable power supplies or diurnal air temperature changes, can lead to highly varying results when different data ranges are evaluated, even for long data intervals.

This investigation will concentrate especially on the influence of starting time for the line source evaluation, t_0, and the required length of the data interval for evaluation. A 10 % deviation in the thermal conductivity is expected after the time criterion, t_c,

has been reached. This is the maximum error allowed for a thermal response test in practice (Eugster, 2002). The sensitivity analysis is performed under the line source requirements as considered in the previous chapter. However, it can be expected that further factors such as the borehole length, boundary conditions and unstable data could lead to further effects.

For the λ_{LS}-evaluation the numerical temperature response is treated differently, as explained in Figure 6-3. The simulated 200 hrs test is evaluated for increasing length of data interval with different fixed starting times between 10 hr (~ t_c) ≤ t_0 ≤ 60 hr and end times between $t_0 < t_E \leq 200$ hr. t_E, the end time of evaluated interval, corresponds to the respective test duration. Figure 6-4 shows the accuracy for t_0= 10, t_0= 20, t_0= 40 and t_0= 60 hr and continuously increasing t_E in comparison to the numerically set thermal conductivity, λ_{num} (3 W m^{-1} K^{-1}). It can be clearly recognized that at early t_0, λ_{LS} is lower than λ_{num}, suggesting an influence of the borehole itself, due to the lower thermal conductivity of the grouting material. At later starting and/or longer ending times, the accuracy of the line source estimation improves. The line source estimation shows a general underestimation with a negligible overestimation for late t_0 and t_E. Changes in t_0 have a stronger effect on the accuracy than those in t_E. For t_0= 10 hr (~t_c), the test duration must at least be 30 hrs to achieve a deviation of less than 10 %, whereas at t_0= 60 hrs the deviation is close to zero, irrespective of the evaluated interval length. Starting the evaluation at t_0~ 20 hrs (i.e. 3 times t_c), the deviation can always be expected to be less than 10 %.

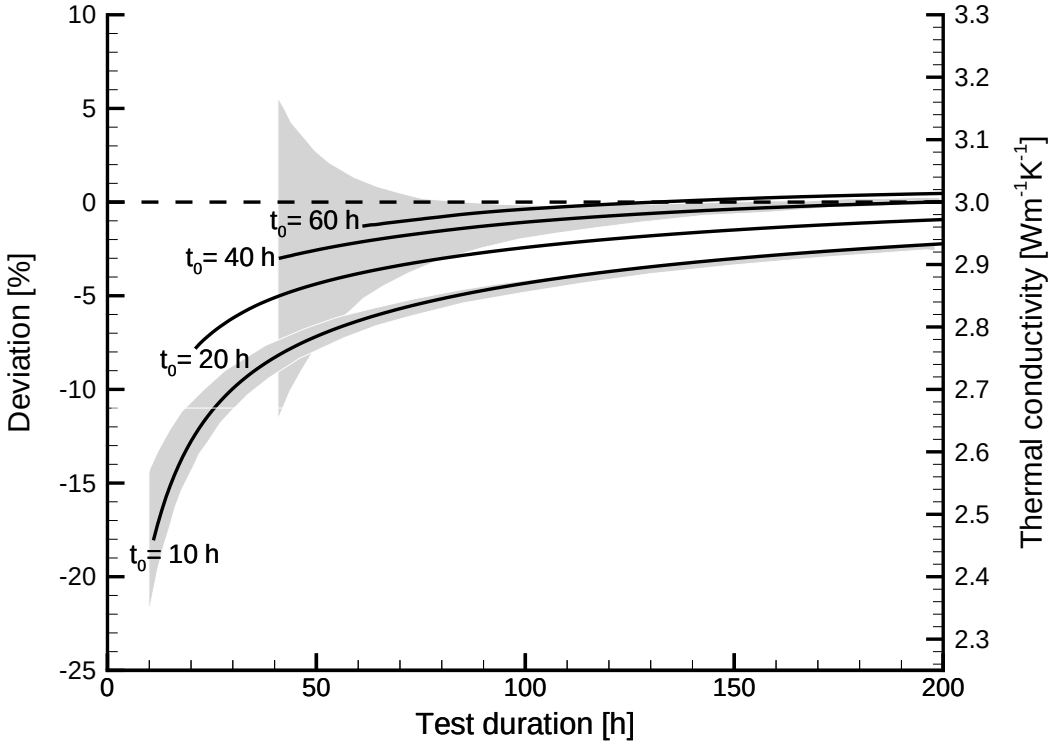

Figure 6-4: Investigation of the necessary test duration for 10 % deviation of the line source model. The deviation is plotted as the difference to the numerical implemented thermal conductivity λ_{num}. The end point of the different evaluated data intervals is fixed at t_E= 200 hrs and the starting point is varied from t_0= 1 hr up to 199 hrs which is shown on the x - axis. Shading: 95 % confidence interval, when 0.1 K white noise is superimposed on the synthetic thermal response.

These statements are true for synthetic data (constant heating and circulation, perfect measurements). However, if actual temperature measurement errors are considered, these deviations will change. Witte et al. (2002) show that a temperature disturbance of only ~0.15 K affects the estimate of thermal conductivity significantly. The effect of a maximum 0.1 K white noise (the general temperature measurement accuracy), which is superimposed on the synthetic thermal response, has been calculated. When applying the λ_{LS}-evaluation to these data, a time dependent interval of λ_{LS} variation can be defined. For the case of t_0= 40 hrs the 95 % confidence interval is shown as a shaded area in Figure 6-4. It demonstrates that for small intervals (t_E slightly higher than t_0) the accuracy is compromised. The deviation from λ_{num} ranges between 0 and >10 % compared to the <4 % under ideal conditions, although this temperature effect vanishes at later t_E. Additionally, we studied this effect for $t_{0=}$ 10 hr. Clearly, due to the strong temperature increase at

early t_0, a smaller confidence interval results. But, at larger t_0, this effect can become dominant. Nonetheless, it may be mentioned that 0.1 K is hardly achieved in practice, and stronger variations must be expected for real response tests.

It can be concluded that a simple definition of t_0 and t_E is not possible. Small values of t_0 tend to underestimate the subsurface thermal conductivity, but show small sensitivity to data perturbation. In contrast, high values of t_0 approximate the subsurface thermal conductivity well, but they are highly influenced by temperature variations. λ_{LS} generally underestimates the thermal conductivity value, but significant data perturbation may also imply a too optimistic design of BHE fields. It needs to be kept in mind that these results are achieved with a model that is adapted to the requirements of the line source model (assuming only a radial temperature field) and that a different model setup considering a temperature gradient and the finiteness of borehole could lead to different results. Thus, BHE length can become important.

6.3.4 Effect of Borehole Length

In this chapter, thermal response tests are simulated for “real” temperature fields. The effect of borehole length is investigated using the model assumptions from Chapter 6.3.3. But, now the boundary conditions for constant temperature at the surface and constant basal heat flow at the bottom of the model are considered.

Under test conditions, the subsurface in a certain volume around the BHE is heated up resulting in an upside down temperature funnel in the subsurface, as illustrated in Figure 6-5 for the 160 m model run. Since thermal response tests can cause a continuous heat flux from the borehole realm to the surface, the isotherms are strongly curved near the surface whereas the temperature field is nearly radial at the bottom of the BHE. The temperature field gets more cylinder-radial with deeper boreholes. The 40 m case will be more affected by surface conditions than the 400 m case and the continuous heat transfer to the surface will result in too high thermal conductivities. Also, the temperature differences between the tubes in the grouting material at the same depth will show dependence on borehole length: Deeper boreholes have more pronounced ΔT due to higher subsurface temperatures than shorter boreholes. This causes an internal flux from one tube to the other and the heat will not be transferred to the ground resulting in too low thermal

conductivities. This will be more significant for the 400 m than for the 40 m case. The interplay of the thermal field around a BHE is determined by both, the radial funnel around the BHE and the internal fluid temperature exchange. It becomes even more complex by the fact that these two processes show transient behavior. So, only if the two effects offset, the analytical analyses of the temperature response will achieve λ_{num}.

Here, borehole depths of 40, 80, 160, 320 and 400 m are simulated. The results are illustrated in Figure 6-6 for fixed t_0= 10 hrs and continuously increasing t_E (analogous to Figure 6-4). The highest λ_{LS}-value is achieved for the shallow 40 m borehole. Furthermore the transient behavior is indicated by the fact that the λ_{num}-value is not achieved for every borehole length at the same time. Whereas in the 40 m case the λ_{num} is achieved after test duration of ~160 hrs, the deeper boreholes still do not after 200 hrs. Figure 6-6 also shows that evaluated λ_{LS} still has not reached a constant value and that, with continuing test duration, shallow boreholes will rather overestimate the thermal conductivity by a certain amount whereas deep boreholes will underestimate it. However, comparing the 160 m model run to the results in Figure 6-4, including “real” boundary conditions results in a λ_{LS}-value 2% higher and the deviation from the implemented numerical thermal conductivity is still generally negative. Furthermore, for test durations of over 50 hrs, the evaluated λ_{LS} generally fits λ_{num} for all model runs within 10 %. Therefore, independent of their depth, BHEs seem not to differ much from the line source assumption and accurate results can be achieved even though the temperature field around the BHE resulting under “real” conditions does not fulfill the line source model requirements.

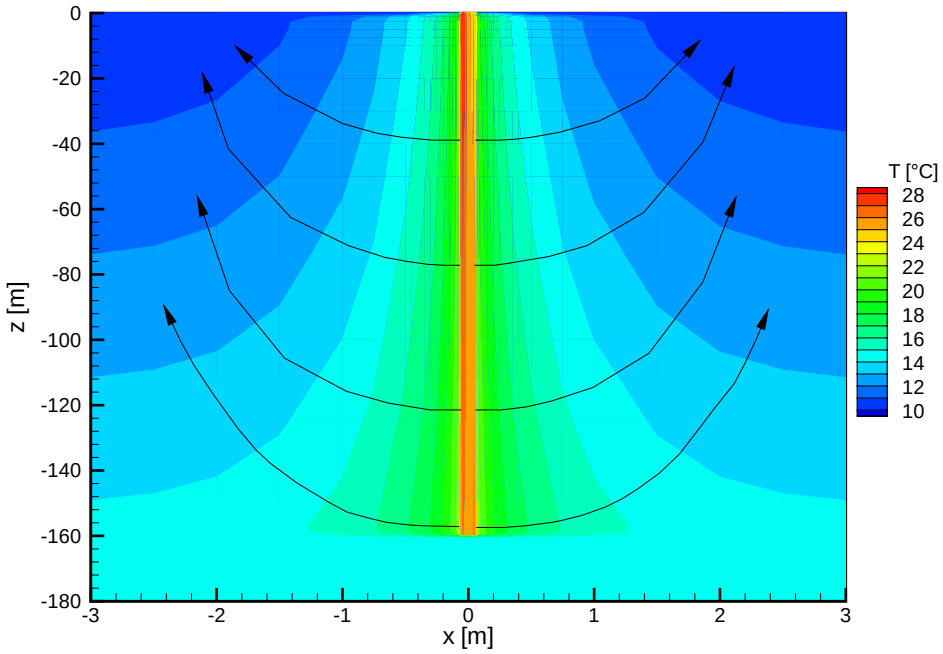

Figure 6-5: Temperature field around the 160 m deep borehole at the end of the response test. The direction of the heat flux is schematically indicated by arrows. Note the different scaling for the x - and the z - axis.

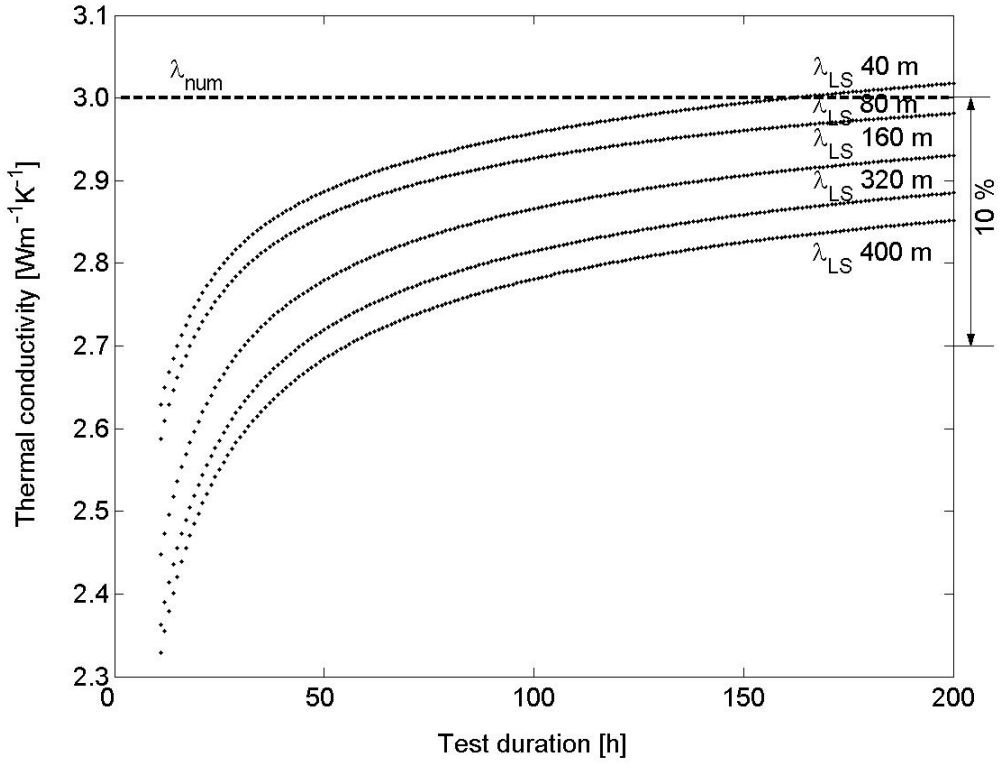

Figure 6-6: λ_{LS} for different borehole lengths, where the first point of the evaluated data interval is fixed at the respective t_0 and the end point is shown on the x - axis.

6.3.5 STRATIFIED SUBSURFACE AND GROUNDWATER FLOW

The line source theory generally assumes that the ground along the BHE is homogenous and the analysis of thermal response tests is expected to yield the average thermal conductivity. However, in a more detailed view, the heat flow between BHE and surrounding rock is determined according to the Fourier law by the temperature gradient and the thermal conductivity. Therefore, heat flow may vary along a BHE due to the changing difference between fluid temperature and ground and when the subsurface is stratified. The evaluation of the thermal conductivity may then be dominated by a specific layer. Eskilson (1987) showed that the effect of a top-soil layer (< 10 m) on the performance of a BHE can be neglected. In this context, it may also be considered that thermal response tests are mostly performed by applying heat injection. In contrast, in Switzerland a BHE is mostly operated under heat extraction conditions (BHEs operated under heat rejection conditions become more and more popular for the cooling of commercial buildings). During heat injection tests the highest temperature difference between fluid temperature and ground occurs in the uppermost part of a BHE. Therefore different layers are stimulated here than under extraction conditions and the estimated “effective” thermal conductivity may not correspond to the thermal conductivity relevant for the operational mode where heat is extracted from the subsurface.

Here, we examine the influence of vertical heterogeneities along the whole length of a BHE for specific, simple cases. For this purpose, we set up two new heterogeneous test cases where the borehole length in the homogenous model from Chapter 6.3.1 is divided into two 80 m units of different thermal conductivity: In model run $M_{4\text{-}2}$ the upper layer has a thermal conductivity of 4 $Wm^{-1}K^{-1}$ and the lower layer has one of 2 $W\,m^{-1}\,K^{-1}$, and model run $M_{2\text{-}4}$ has an inverse profile (In shallow subsurface, thermal conductivity often increases with depth). The mean thermal conductivity (3 $W\,m^{-1}\,K^{-1}$) corresponds to the homogenous 160 m case in Chapter 6.3.4. For these model runs, 200 hrs response tests are performed applying both heat injection and heat extraction.

Figure 6-7 summarizes the results of the assumed specific model cases for fixed t_0= 10 h. In the case of a homogenous subsurface the evaluated λ_{LS} is nearly identical, independent of the applied test method, with a general underestimation. The stratified test cases generally show lower thermal conductivity than the

homogenous cases and the layer with lower thermal conductivity seems to dominate slightly. It is interesting that in the stratified cases depending on the applied test scenario, different results are achieved. As shown in Figure 6-7, the λ_{LS}–values for $M_{2\text{-}4}$ are on average 3 % higher for heat extraction than for heat injection response test. The reason for the different results is that in heat extraction tests the highest temperature difference between fluid and surrounding rocks exist in the deeper part of the BHE. More energy is dissipated into the lower layers with the higher thermal conductivity than the upper showing up as higher overall λ_{LS}–values. In the assumed test case, when performing heat injection tests for future heating applications (i.e. corresponding to a heat extraction test), the generally performed heat injection test would provide ~3 % lower values than the effective thermal conductivity and the BHE plant would be slightly overestimated. But, for $M_{4\text{-}2}$ with the high conductive upper layer, the effects are reversed and the BHE may slightly be undersized. However, the analytical evaluated thermal conductivity for the stratified test cases shows only a small difference from that of the homogenous case. All model runs fit λ_{num} within 10 %.

Clearly, in reality the undisturbed ground temperature along a BHE and the thermal conductivity will not have a linear profile and the heat flow along the BHE will be much more heterogeneous. However, it could be shown that even under the simple model conditions, layers are differently stimulated depending on the test scenario. Besides, Witte (2001) showed in his experiment that heat injection and heat extraction tests yield different results under saturated conditions. The thermal conductivity estimated with heat injection resulted in values 10 % - 15 % too high. These conductivity values are apparently not representative of the subsurface conditions and cannot directly be used for BHE design. In contrast, his experiments showed comparable conductivities when no groundwater flow occurs. This underlines our results from Figure 6-7 that, for a stratified subsurface, λ_{LS} shows only a small difference from that of the homogenous model run. However, heterogeneous subsurface may become important in cases of groundwater flow. These circumstances require appropriate test setups for heating or cooling (heat storage) purpose.

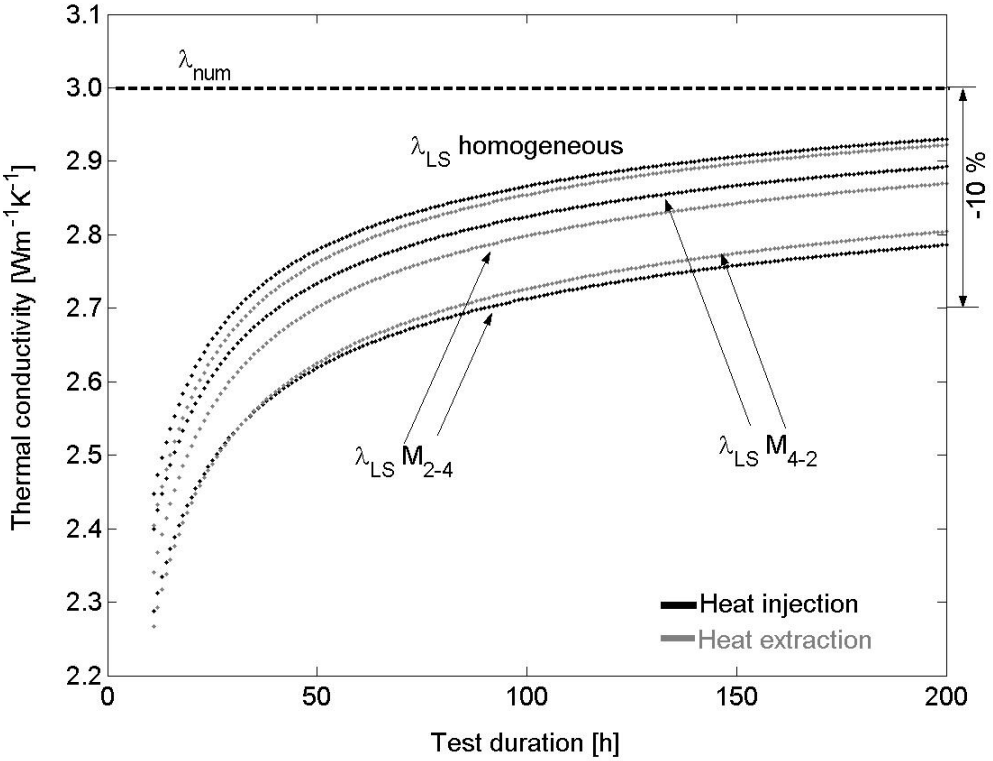

Figure 6-7: λ_{LS} - evaluation for the heterogeneous model runs $M_{2\text{-}4}$ and $M_{4\text{-}2}$ compared to the homogeneous model M_2 with the same average numerical thermal conductivity. The first point of the evaluated data interval is fixed at the t_0= 10 hr and the end point is shown on the x - axis.

In a next step, we investigate the influence of groundwater flow on the conductive estimated “effective” thermal conductivity. Presence of groundwater generally increases the possible heat extraction from a BHE (Signorelli et al, 2002, Wagner and Clauser, 2002). Basically, conductive and advective processes underlay different physical conductions and must be treated differently. In cases of no significant groundwater flow, the two processes may be approximated by one single thermal conductivity, but this assumption is not valid in areas of high groundwater movement (Pe >1). However, the line source evaluation cannot separate between the two processes and results only an average thermal conductivity.

The groundwater influences on thermal response tests have been observed in several field observations (e.g.: Gehlin, 1998, Sanner at al., 2000, Witte, 2002). Different theoretical studies (Claesson and Hellström, 2000, Chiasson et al., 2000, Gehlin and Hellström, 2003) have shown that temperature effect of moving groundwater flow becomes increasingly important in rocks of high hydraulic conductivity.

The FE code FRACTure allows us to investigate this problem in 3D. For this purpose, a single, 10 m thick horizontal zone is introduced at 80 m depth surrounded by impermeable zones in the homogenous 160 m model. The thermal conductivity of the aquifer is calculated assuming a 20 % effective porosity and a rock of a thermal conductivity of 3 W m^{-1} K^{-1}, all other input parameters are kept as described in Chapter 6.3.1. The flow inside this zone is assumed to be fully saturated and unidirectional and is described by Darcy's law, with the Darcy flow velocity, v_D, defined from hydraulic conductivity and hydraulic pressure gradient. v_D varies between 0.1, 0.5, 1, and 2 m per day (Model runs $M_{VD=0.1}$, $M_{VD=0.5}$, $M_{VD=1}$ and $M_{VD=2}$). Larger flow velocities could also be investigated, but the selected range represents the most interesting cases. Faster flow would extend the range of calculated λ_{LS}. Due to the temperature-dependence of the hydraulic conductivity the effect of groundwater flow is also temperature-dependent. In the context of BHE operation, it can be expected that the temperature of groundwater below 20 m remains constant throughout the year and that cooling will only affect a small area near the BHE. For simplicity reasons the temperature dependence is therefore ignored here. However, the temperature dependence of viscosity may be considered for BHE fields in areas of significant groundwater movement, which affect a much larger groundwater volume.

In Figure 6-8, λ_{LS} for the different simulation runs is compared to the purely diffusive case called here M_{diff}, again for t_0= 10 h. Considering the characteristic flow length ΔL as the BHE diameter, the Peclet Number, Pe, for 0.1 m per day or lower is significantly <1 (see Eq. 2-18). The thermal regime is conductively dominated and no influence of moving groundwater must be expected; a fact that confirms the results of Chiasson et al. (2000). The effect of groundwater movement is already clearly visible in model run $M_{VD=0.5}$ for 0.5 m per day (Pe ~1.7). Comparing evaluated λ_{LS} for the 10 – 200 hrs data interval, the thermal conductivity for $M_{VD=0.5}$ (λ_{LS}= 3.1 W m^{-1} K^{-1}) is 7 % higher than for M_{diff} (λ_{LS}= 2.9 W m^{-1} K^{-1}). The increase grows with each further doubling of flow velocity from 3.2 W m^{-1} K^{-1} for $M_{VD=1}$ (Pe ~3.4) up to 3.4 W m^{-1} K^{-1} for $M_{VD=2}$ (Pe ~6.8). However, the impact of groundwater movement not only depends on the magnitude of flow velocity, but also on the water volume (i.e. mass flow rate) involved. Therefore, two additional models for aquifer thicknesses of 1 and 20 m and a constant flow velocity of 1 m per day are

calculated: $M_{VD=1A}$ and $M_{VD=1B}$. Due to its 10 times smaller aquifer thickness, the mass flow in $M_{VD=1A}$ is identical to $M_{VD=0.1}$. The mass flow of $M_{VD=1B}$ corresponds to that in $M_{VD=2}$. Figure 6-8 compares the model runs. $M_{VD=1A}$ shows nearly no impact of groundwater flow and λ_{LS} corresponds well to those of the zero flow model M_{diff} and $M_{VD=0.1}$. In $M_{VD=1B}$ the influence of groundwater flow results in a 24 % higher value for the 10 – 200 hrs interval than M_{diff}. Compared to $M_{VD=2}$, the groundwater flow results here in significantly higher values (λ_{LS}= 3.6 $Wm^{-1}K^{-1}$). Even though, the mass flow is identical, its impact in $M_{VD=1B}$ is higher due to the larger area of heat exchange.

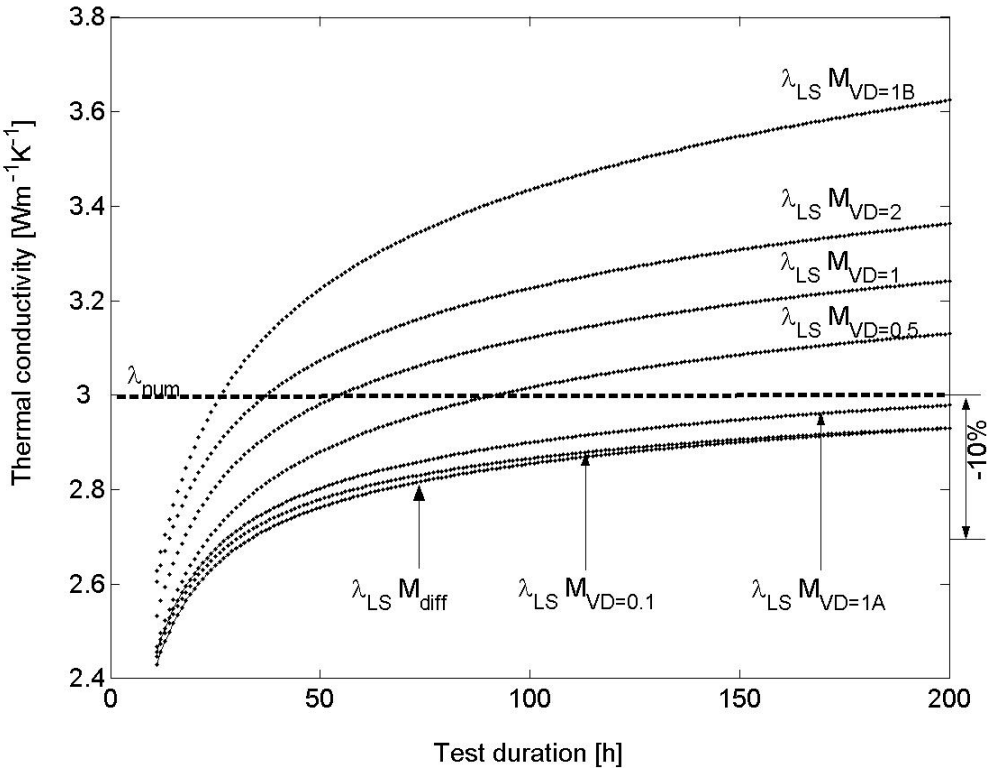

Figure 6-8: λ_{LS} - evaluation for different groundwater flow models compared to the no-flow model M_{diff}, where the first point of the evaluated data interval is fixed at the t_0= 10 hr and the end point is shown on the x - axis. For all groundwater models λ_{LS} continuously increases. For the curve parameters see text.

The three-dimensionality of the problem is shown in Figure 6-9 for $M_{VD=1}$ illustrating the disturbance of the temperature field by groundwater movement. During a heat injection response test, flowing groundwater removes heat from the ground near the BHE and reduces the temperature of the heat courier fluid. The thermal energy loss can clearly be seen on the downstream directed plume.

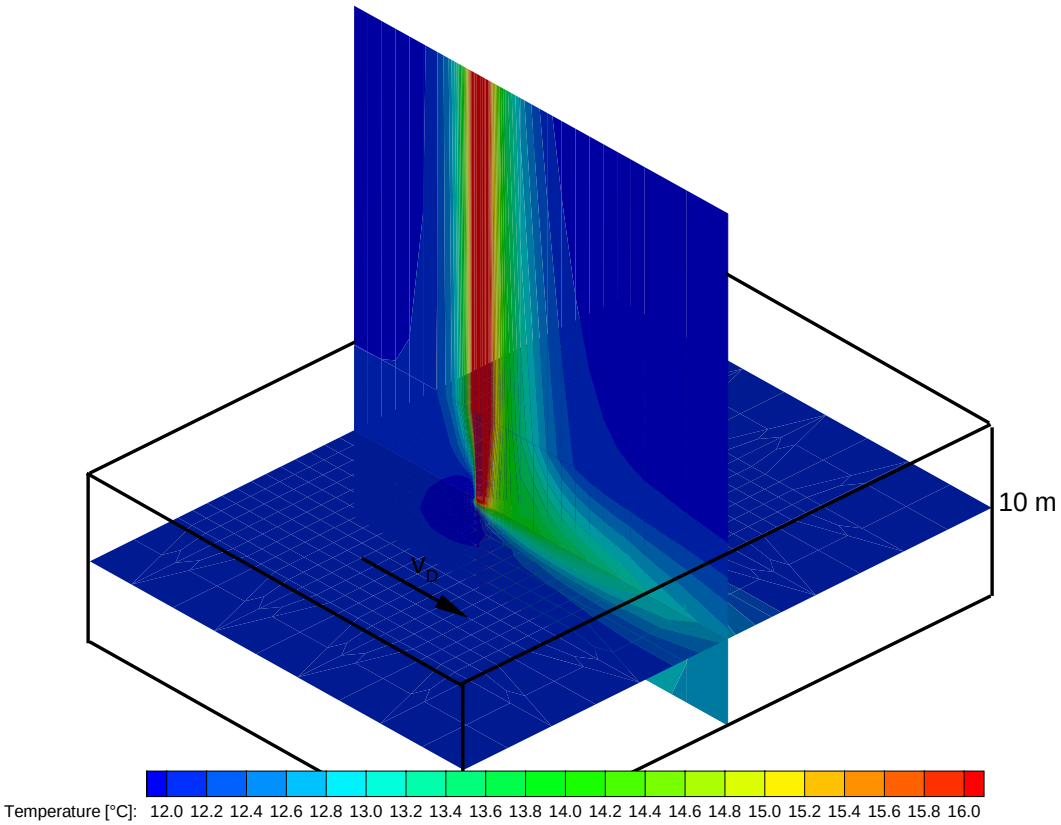

Figure 6-9: Horizontal and vertical cross sections illustrate the temperature field of $M_{DV=1}$ after a thermal response test of 200 hr. The thermal plume downstream can clearly be seen.

Typical for all groundwater simulations λ_{LS} becomes progressively higher with time (see Figure 6-8). Analogous behavior was observed by Witte (2001) in a field experiment. In a real field case, a thermal response test cannot evaluate the true thermal conductivity without further analysis. A first study concerning this topic by Chaisson et al. (2000) shows that values derived from short tests (50 h) are more reliable for designing heating systems than those from long tests (168 h), with a general BHE overdesign (i.e. deeper boreholes than necessary). This clearly shows that in areas with groundwater flow, thermal response test requires analysis models accounting for groundwater movement.

In this context, response tests could be used for hydrogeological applications. The idea is to apply the temperature response as a tracer for groundwater flow. Generally, borehole cuttings are available, and from laboratory measurements the thermal conductivity can be measured. From drilling data, the thickness of the aquifer can be derived. Implementing all this available subsurface information into a numerical model, the hydraulic properties and conditions might be acquired by fitting

the temperature data of a thermal response test applying parameter estimation techniques. Using FE code FRACTure for such a purpose would have the advantage that three-dimensionality of the subsurface structure can be accounted for and that Darcy flow, the effective flow velocity, could be obtained.

6.4 EVALUATION OF THE SUVA RESPONSE TEST

6.4.1 DATA SET

In the design of the SUVA building at Gisikon, Switzerland, ground heat storage was integrated in the energy concept of the building (Pahud, 2001). This required the knowledge of the thermal properties of the ground. Therefore, a thermal response test was carried out to determine in-situ the thermal conductivity of a 160 m BHE equipped with a double U-pipe. The tubes are separated by spacers and quartz sand based cement was used as grouting material (thermal conductivity= 1.5 W m^{-1} K^{-1}, heat capacity= 2 MJ m^{-3} K^{-1}). The volume of injected backfilling was measured and corresponds to the volume to fill. The BHE is operated with water as circulation fluid. The characteristic of the BHE is summarized in Table 6-1.

Table 6-1: Characteristic of the SUVA borehole.

Depth	160 m
Diameter	0.152 m
Pipe material	Polyethylene
Outer pipe diameter	40 mm
Pipe thickness	3.7 mm
Spacer (shank spacing)	7.8 cm
Grouting material	Quartz sand
Heat carrier fluid	Water
Test flow rate	810 l h^{-1} *)

*) During BHE operation the circulated volumetric flow rate is 1200 l/h

At a short distance from the BHE, a borehole was drilled to extract ground samples. The geology consists of unconsolidated rocks at the surface and of conglomerates and mainly sandstone below. The rocks belong lithologically to the Upper Marine Molasse characterized by relatively high thermal conductivities. The laboratory measurements yield a geometric average thermal conductivity over the 160 m BHE

length of 3.6 W m^{-1} K^{-1}, the individual values vary between 2.92 and 4.73 W m^{-1} K^{-1} with lower values in the upper than in the lower part of the BHE (Schärli and Rybach, 1999). The average heat capacity is 2.3 MJ m^{-3} K^{-1}. Both boreholes were dry, meaning no obvious ground water flow occurred, and under these conditions, based on the results from Chapter 6.3.5, one can expect that the line source approximation will provide an average thermal conductivity.

The applied response test device was developed at the LASEN / EPFL (Laloui et al., 1998). The electric power can be set to 3, 6 or 9 kW. The test device with the electric heater and the connecting pipes to the BHE (~2 m length) are insulated. The inlet and outlet temperature, the air temperature inside and outside the test device, the fluid flow velocity and the electric consumption (heater and pump) are measured every minute by a data logger and stored as 10 minute averages. The inlet and outlet fluid temperatures are measured with a precision of +/- 0.05 °K, with the purpose to recalculate the injected thermal power into the borehole from the actual flow rate. The flow rate is measured with a precision of 1 %. The flow rate applied during the test was rather low (see Table 6-1), mainly due to the large pressure drop of the flow meter and the relatively small pump (electric consumption of 60 W).

Figure 6-10 illustrates the measured temperature data and the calculated heat injection. Using a 17 hr circulation test before starting the response test, the initial average ground temperature can be determined. Since the circulated fluid did not have the same temperature as the ground initially, the test had to be run until the temperature stabilizes. The influence of the pump heating effect should be less than 55 W. According to Bassetti (2003) the change of fluid temperature in this particular application is ~0.05 K. The initial average temperature can be defined as 12.4 °C +/-0.1 K. After the circulation test the response test itself was started with an average of 6.2 kW heat injection for 122 hr. According to Figure 6-4, the test duration should be about this length to achieve good results. As Figure 6-10 shows, the thermal heat injection varies about 5 % from the average value. These variations are attributed to the daily varying grid voltage. The measured temperature evolution approaches a nearly constant value with test duration, but, the variations in injection rate introduce perturbations into the temperature measurements. These perturbations affect the thermal conductivity estimation (see also Chapter 6.3.3).

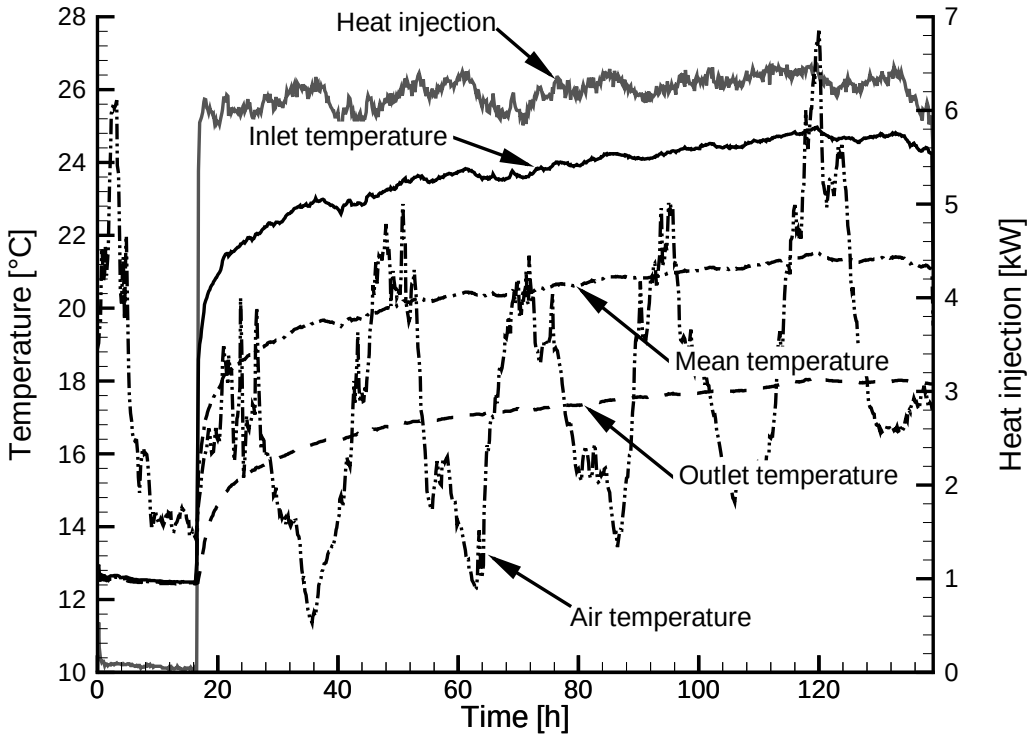

Figure 6-10: Data set of the SUVA thermal response test.

6.4.2 LINE SOURCE MODEL

As shown in Figure 6-4, the line source approach depends on the data length used for the analysis, and is sensitive to small temperature disturbances (e.g. Witte et al., 2002). The SUVA data set was evaluated applying the typical analysis procedure for thermal response tests (Pahud, 2001). Different data measurement intervals are evaluated for a fixed starting time, t_0= 5 hrs (~t_c), and continuously increasing interval length in steps of 10 min from t_E=t_0 up to t_E= 122 h. The estimated λ_{LS} - values are given in Figure 6-11, where the test duration on the x - axis corresponds to each ending time of the individual evaluated data interval. The results show unstable solution for the thermal conductivity, especially for short data intervals. For the evaluation of data intervals longer than 40 h, this effect decreases and the thermal conductivity approaches 3.0 W m^{-1} K^{-1}. This is a -20 % difference to the average laboratory value. Later, it will be investigated if this difference can be explained by the variation of injection rate. A closer look at the heat injection rate reveals variations on a daily scale, maybe due to the unstable power supply. Assuming the average power supply to be constant over one day, the heat injection should also be

constant during one day. Therefore the evaluated λ_{LS} for 24 hr blocks are compared. In Figure 6-12 these values are marked. The values still become lower with time. The last day was a Sunday and the heat injection was slightly higher due to the fact that the grid voltage is linked to the industrial activity and thus is somewhat higher during weekends. However, the average thermal conductivity for the other test days of 3.2 W m^{-1} K^{-1} is still about 15 % lower than the laboratory measurements. Even though the line source model is highly sensitive to variations in the heat injection rate, the measured variation can not explain this difference.

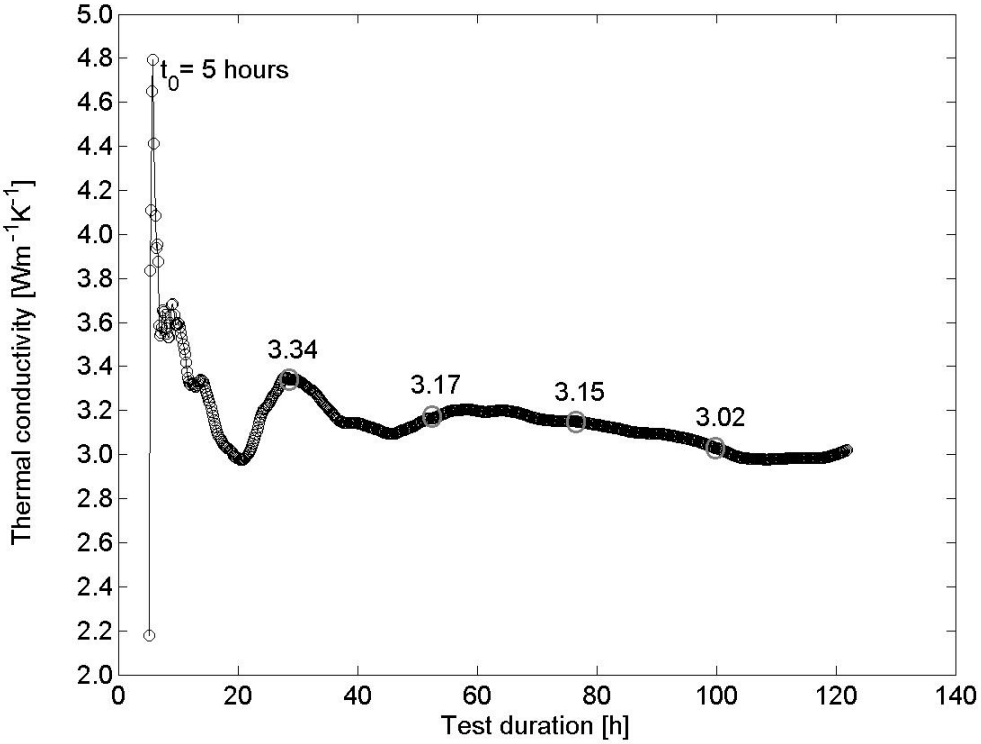

Figure 6-11: λ_{LS} - evaluation of the SUVA dataset by line source model. The first point of the evaluated data interval is fixed at the t_0= 10 hrs and the end point is shown on the x - axis.

6.4.3 NUMERICAL MODEL

Next, the SUVA data set is evaluated using FRACTure to handle variations in heat injection rate with the parameter estimation procedure (See Chapter 6.2.2). The necessary input parameters such as the thermal properties of the grout and the borehole layout are available (see Table 6-1). The heat capacity of the subsurface is known from the laboratory measurements (see Chapter 6.4.1). The FE mesh used for the evaluation is that described in Chapter 6.3.1. Through several model runs it is

intended to identify the average thermal conductivity and to compare the results to the line source evaluation.

During each model run the FE mesh was initialized with the same steady-state temperature field. This initial temperature field is constrained by the ground surface temperature of 10.5 °C (Signorelli and Kohl, 2003; see Chapter 5) and by the average fluid temperature in the borehole of 12.5 °C, derived from the circulation test before the thermal response test started (Pahud, 2001). The average temperature can be assumed to corresponding to the half depth of 80 m, and thus a gradient of 2.5 K per 100 m is assumed. For model runs with different thermal conductivities, the basal heat flow is adjusted to achieve the identical initial temperature field.

Starting from this initial temperature field, the simulation begins with the 17 hrs circulation test period. This procedure replicates the initial state of the FE mesh to the actual SUVA data set. Afterwards, the thermal response test is modeled with the injection rate being varied every 10 minutes corresponding to the heat injection rate measurements. Simulations are performed for different numerical thermal conductivity values whereby the particular temperature response is compared to the measured outlet temperatures. The model run with the smallest residuum from the measurements represents the effective thermal conductivity of the subsurface (see Chapter 6.2.2). Beside the thermal conductivity, the relative position of the four tubes inside the borehole is the only unknown parameter. For thermal response test applications, Bassetti (2003) could demonstrate that the relative location of spacer-separated pipes does only have minimal effects on the evaluation.

Figure 6-12 illustrates the results of the different model runs. For readability only the temperature response for λ_{num} of 3.5, 3.7 and 3.9 $Wm^{-1}K^{-1}$ are shown in comparison to the measurements. This plot illustrates how precisely the temperature variation can be modeled. The thermal conductivity with the smallest residuum is 3.7 $Wm^{-1}K^{-1}$, a value that is closer to the laboratory measurements of 3.6 $Wm^{-1}K^{-1}$ than the value of the line source evaluation (see Chapter 6.4.2).

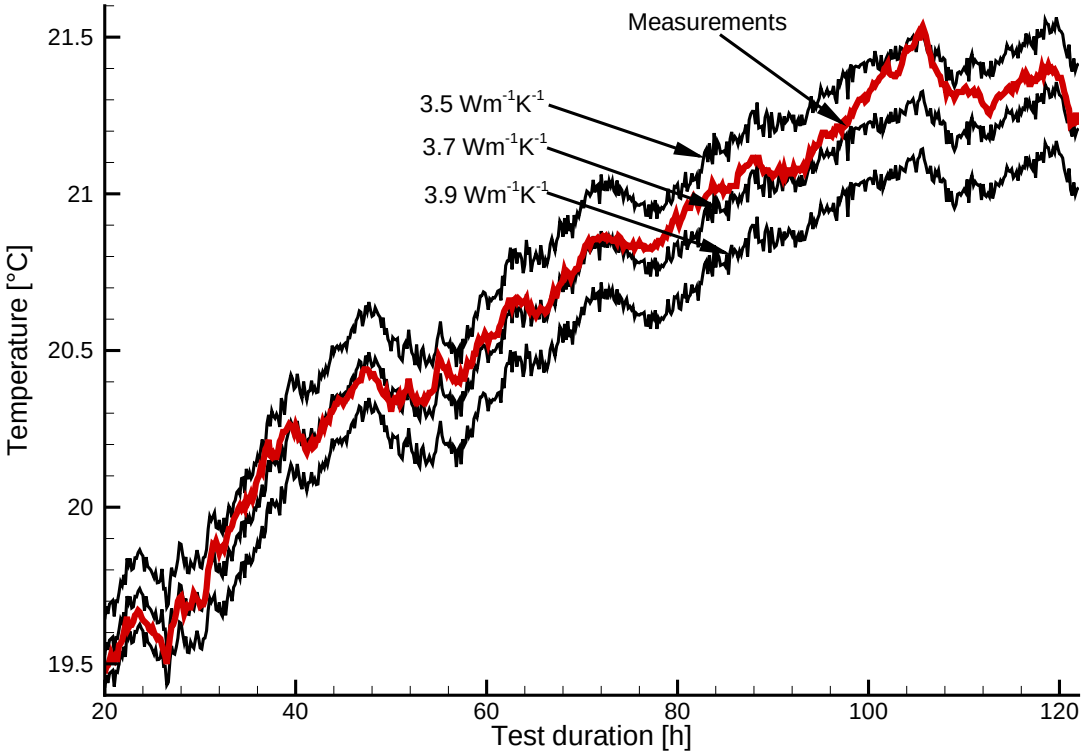

Figure 6-12: λ_{num} - evaluation of the SUVA dataset. The simulated temperatures are compared to the measured outlet temperatures.

6.4.4 Discussion

The most obvious reason for a ~10 % difference between λ_{LS} and λ_{num} is the unstable heat injection rate. But when reviewing Figure 6-12, even though the numerical simulation accounts for time-varying heat injection, time-dependent effects still can be recognized, indicating other influences. Therefore, the best fit values were calculated for every 10 minutes and plotted as a smoothed curve in Figure 6-13. λ_{num} varies between 3.9 $Wm^{-1}K^{-1}$ and 3.5 $Wm^{-1}K^{-1}$ and becomes lower with time. This trend is overlapped by shorter cycles where λ_{num} seems to vary between locally lower and higher values on a daily scale. Daily variations in power supply can not be the reason for this variation since they are considered by the λ_{num} evaluation. But, the additionally plotted difference ΔT between the air and fluid temperature shows the clear correlation with the variation in λ_{num}. If the air temperature is higher than the average fluid temperature, heat energy seems to be added to the fluid. This increases the injected amount of heat, and the temperature seems to increase with a higher rate, hence, a lower thermal conductivity results. The inverse effect occurs when the air temperature is lower than the fluid

temperature (e.g. thermal energy losses yield to higher thermal conductivity). This seems to result from insufficient insulation of the test device and of the connection pipes to the BHE tubes. Only if the air temperature corresponds to that of the fluid, no external influences exist. The average of λ_{num}–values where the temperature difference ΔT is 0 K amounts to 3.6 $Wm^{-1}K^{-1}$, which corresponds exactly to the laboratory measurements.

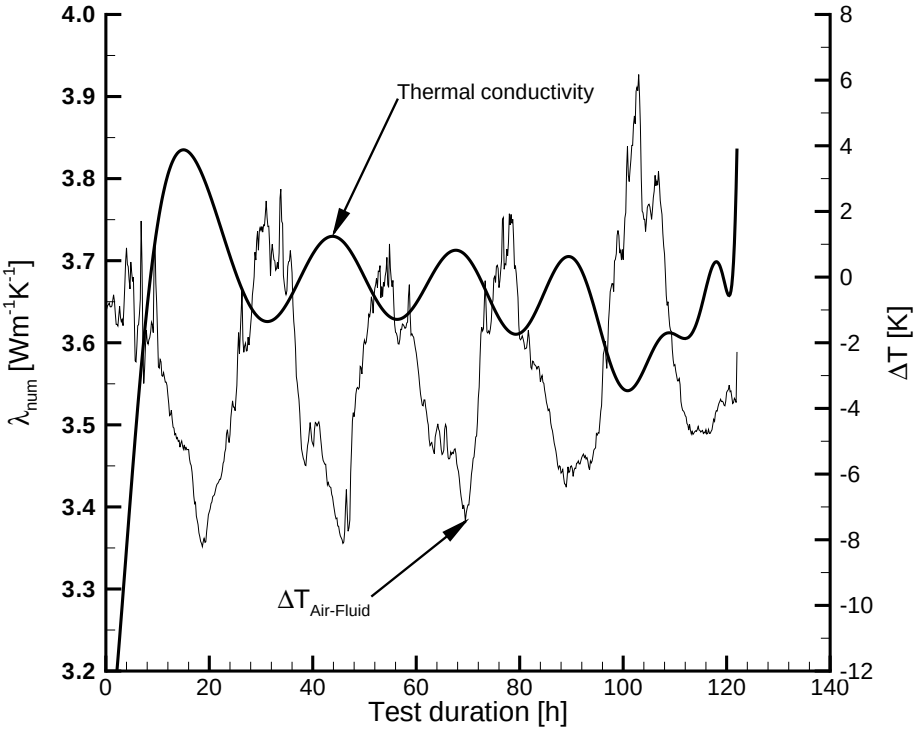

Figure 6-13: Further treatment of the SUVA dataset showing the correlation between λ_{num} – evaluation and the diurnal air temperature variation.

The line source model is an easily applicable and fast evaluation method, but the estimation of the ground thermal conductivity is sensitive to the test conditions (principally the stability of the heating power and the influence of the weather conditions on the heat injection rate). An advantage of the FRACTure model over the analytical method is that varying heat injection rates can be accurately accommodated on any time scale. This allows a time dependent evaluation of the temperature records where any data point can be fitted individually. So possible influences of the ambient temperature can become visible and a more sophisticated data interpretation can be performed. Furthermore, an exact treatment of the borehole geometry and of the surroundings is possible.

6.5 CONCLUSIONS

For the first time, 3D FE numerical model was utilized to investigate thermal response tests. In the first part of this chapter, temperature responses derived from FRACTure models were evaluated by the analytical line source model as if they were experimental records. This procedure provided an estimate of the accuracy of general thermal response test interpretation and information about the necessary testing duration. The influence of borehole length, heterogeneous subsurface conditions, groundwater movement, and of variable data quality on the line source evaluation was presented. In total, more than 30 model runs were simulated.

The investigations showed that under simulated ideal test conductions, the line source analysis generally provides good results. However, the superposition of different errors can easily reach ~10% from the model parameter and corresponds to the intended accuracy. Also the layering of subsurface lithologies results in differences between operational conditions (when the subsurface is cooled) and testing conditions (when the subsurface is heated). Although, the analytical evaluated thermal conductivity shows only a small difference from that of the homogenous case, heterogeneous subsurface may become important in cases of groundwater flow. Therefore, for heating purposes, an extraction test may then achieve more reliable results. However, most effects, except groundwater movement, yield in an underestimation of in-situ thermal conductivity resulting in an over-dimensioning.

The experimental SUVA thermal response test was evaluated in the second part of this chapter. The reported thermal conductivity values derived from the line source model vary by over 20 % from available laboratory measurements what is largely above the intended accuracy. This may put into question the reliability of the results. The numerical evaluation could explain the difference and close the gap between laboratory and in-situ measurements. It could be illustrated from the SUVA data set that FRACTure can provide for a sophisticated understanding of disturbed data sets. In contrast to analytical models, FRACTure accurately treats the borehole geometry and variation in heat injections and is therefore well-suited to a detailed evaluation of response tests. The thermal conductivity can be resolved on any time scale and thus, time-variant ambient temperature effects in the SUVA data set could be identified. The identified influence of air temperature suggests an insufficient

insulation of the test device and of the connecting pipes between the device and the BHE. Currently the testing device measures the BHE inlet and outlet temperature inside the test device. Gehlin (2002) suggested placing the sensors into the tube below the subsurface to improve the accuracy of the test.

The possibility of identifying various effects like time-dependent heat injection rate or the influence of air temperature leads to a better interpretation of the experimental data. However, this requires more time consuming numerical simulations compared to analytical models. Therefore, a first order estimation of subsurface thermal conditions by fast, conventional methods is advised. However, depending on the fluctuation and importance of the results for the planning purpose of a building, a reevaluation by numerical methods should be targeted. More reliable evaluations would allow a more accurate dimensioning of BHE fields, which could even reduce the cost of the total project. In the future numerical modeling may become much faster, particularly with automated mesh generation. To promote this development, the reliability of this technique has to be proven on other data sets.

7. STRUCTURAL INFLUENCE ON THE BHE BEHAVIOR

Increasing use of BHEs will be based on customer confidence in this relatively new product; and this only comes from reliable long-term performance of BHE systems. Ultimately, the performance depends upon proper design. An under-designed plant can lead to significant problems during operation, including too high operational costs, and possible structural damage, and even cases where a plant closure is necessary. Over-design of the plant leads to high installation costs and makes the BHE system uneconomical.

Therefore, investigations of BHEs must balance engineering costs with precise geothermal and scientific understanding. The foremost question is how much thermal power can be extracted from a specific subsurface. When answering this question the thermal conductivity turns out to be a key parameter, which defines the possible heat extraction for a given geological subsurface condition. Based on experience the VDI guidelines (2001) list average heat extraction rates for different geological layers. The thermal heat extraction strongly varies from ~20 W m^{-1} for dry gravel to >100 W m^{-1} for subsurface of high groundwater flow with a mean of ~50 W m^{-1}. These values are only valid for simple BHE systems (single BHES in the heating mode and with annual runtimes of maximally 1800 h; VDI guidelines, 2001), and should not be used for complex systems with several BHEs in an array.

It is not only the subsurface thermal conditions which play a role in determining the thermal power, but also the topographical elevation. On the one hand, the topographical elevation defines the heating energy demand for a specific building (this aspect is generally covered by heating engineers). On the other hand, topography has a strong influence on the subsurface temperature field, which determines the heat content in the subsurface. The topographical influence consists of two separate effects: the morphological condition and the GST. The isotherm surfaces tend to follow the broad trends of the morphology, rising under peaks and falling under valleys. Thus, the vertical temperature gradient under a peak is lower than under a valley (Kohl, 1999). The situation is complicated by the fact that the GST depends upon altitude so that the ground surface is not an isotherm. Kurmann (2003) showed that for modestly undulating areas as in the Alpine Foreland where most BHEs are installed (see Figure 1-2) morphological effects can be neglected.

Therefore topography is to be considered only for the Alpine regions, and not the lower Alpine Foreland.

Proper design means the ability to correctly adopt the BHE system to these site-specific conditions. This requires a proper knowledge of the thermal conductivity and the GST. Thermal conductivity values can be estimated for the Swiss Alpine Foreland from SwEWS (Leu et al, 1999) or for large projects from a thermal response test (see Chapter 6). GST-values are available for the Swiss Alpine Foreland from the new GST map in Figure 5-5.

Stalder et al. (1995) developed a nomogramm (see Figure 7-1) to dimensioning BHEs in a simple way accounting for altitude as a substitute for GST and thermal conductivity. At the beginning stands a building with a certain heating power and energy demand. Depending on altitude, the COP which should be achieved and the subsurface thermal conductivity the required BHE length can be estimated.

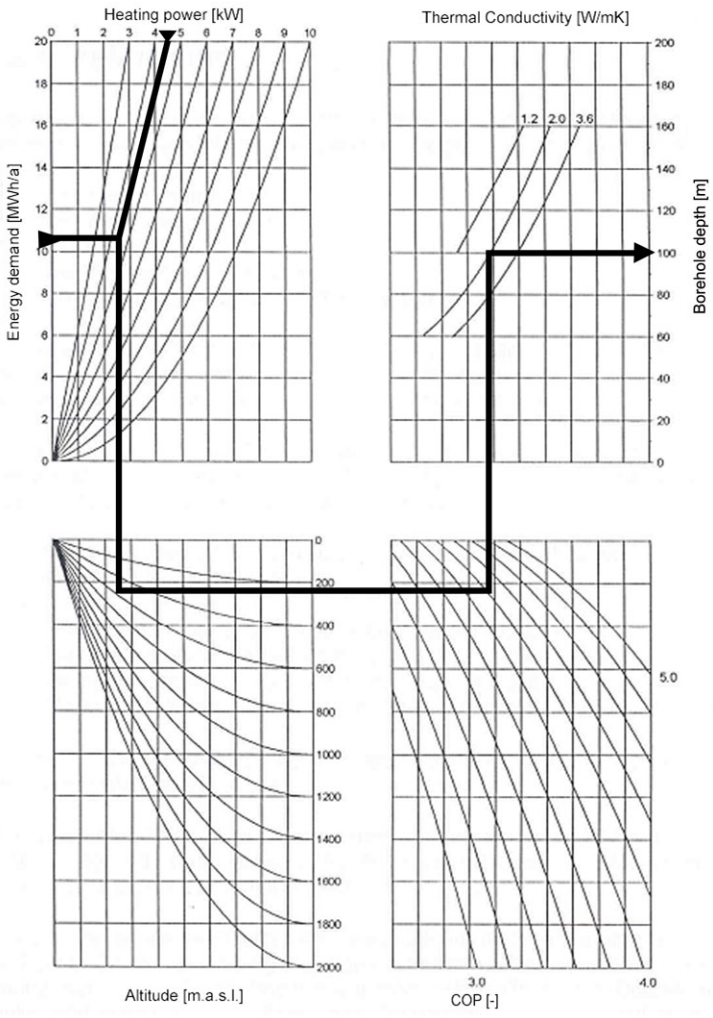

Figure 7-1: Nomogramm for the dimensioning of BHEs (after Stalder et al., 1995).

This chapter primarily focuses on the influence of the thermal conductivity and the GST on the thermal power of a BHE. The investigation uses thermal parameters suitable for Switzerland, and results are displayed visually for different locations in Switzerland Groundwater flow, although important as a heat transfer mechanism, is not discussed here.

7.1 GENERAL PROCEDURE

Various simulations are carried with a range of thermal conductivity and GST-values to determine their influence on the thermal power production of a BHE system. First, a reference model run is set up to benchmark all the different simulations. The FE mesh for the reference model is described in Chapter 3.2.4, with the exception of a BHE depth of 150 m. Except for this parameter, all model conditions are equal to those in Table 3-1. This reference model is consistent with the site conditions at the Swiss Meteorological Institute in Zürich which represents an average location in the Swiss Alpine Foreland.

The possible heat extraction from this reference BHE is estimated and then compared to the thermal power output from the other model runs. For that purpose, the BHE inlet temperature is constantly set to T_{in}= 1 °C and power is calculated from the outlet temperature. The total runtime of 1800 hrs per year is simulated, subdivided into the different monthly runtimes listed in Table 3-4. The load is distributed according to the “single peak load” case as described in Chapter 3.2.7, assuming a constant operation period at the beginning of every month followed by a recovery period during the rest of the month. This provides a conservative thermal power estimation, because the simulated loading of the subsurface temperature is stronger than a realistic load profile. Pure diffusive simulations are performed over one year and the presented results reflect this first operational year. For the reference model with $<GST>_a$= 11.1°C and thermal conductivity= 2.44 W $m^{-1}K^{-1}$, an average thermal power of 6.4 kW is obtained.

The simulations to determine the influence of thermal conductivity and GST are carried out and the extracted thermal power is compared to the reference model. This same procedure is applied to a 160 m deep BHE model. The difference in thermal power between these two model runs corresponds to the increase in thermal power when drilling 10 m deeper at the specific local setting. When assuming a

linear relationship between the thermal power and drilling depth along this 10 m depth interval, the BHE length to add or to shorten can be interpolated which is necessary to achieve the same thermal power as under the reference model site conditions.

7.2 INFLUENCE OF GEOLOGY

To illustrate the influence of the thermal conductivity on thermal power, the value is varied between 1 and 3.8 W m^{-1} K^{-1}, representing more or less the value range in the Alpine Foreland (Leu et al., 1999). Figure 7-2 shows the thermal power for the different thermal conductivity values as well as for the reference BHE. The results represent the conditions after one operational year. For the 150 m deep BHE the extracted thermal power rises from 5.2 kW (35 W per meter of specific heat extraction) at 1 W $m^{-1}K^{-1}$ to 7.3 kW (48 W per meter) at 3.8 W $m^{-1}K^{-1}$. This is an average gain of ΔP= ~140 W per $\Delta\lambda$= 0.2 W $m^{-1}K^{-1}$. For the 160 m deep BHE the increase runs almost parallel, with higher power of ~390 W higher power. This difference represents the thermal power gain per 10 m additional BHE depth. Now, it can be estimated by how much the BHE must be extended or can be shortened to achieve the same thermal power as the reference BHE at 2.44 W $m^{-1}K^{-1}$ during the first year of operation. The adjustment of thermal power can be expressed in drilling meters as is shown in Figure 7-3. For constant energy demand, the change in thermal conductivity may be compensated by a change in drilling meters, Δz_{BHE}, expressed by the following 2nd order polynomial:

Eq. 7-1 $$\Delta z_{BHE} = 1.9 \cdot \lambda^2 - 27.6 \cdot \lambda + 56.7$$

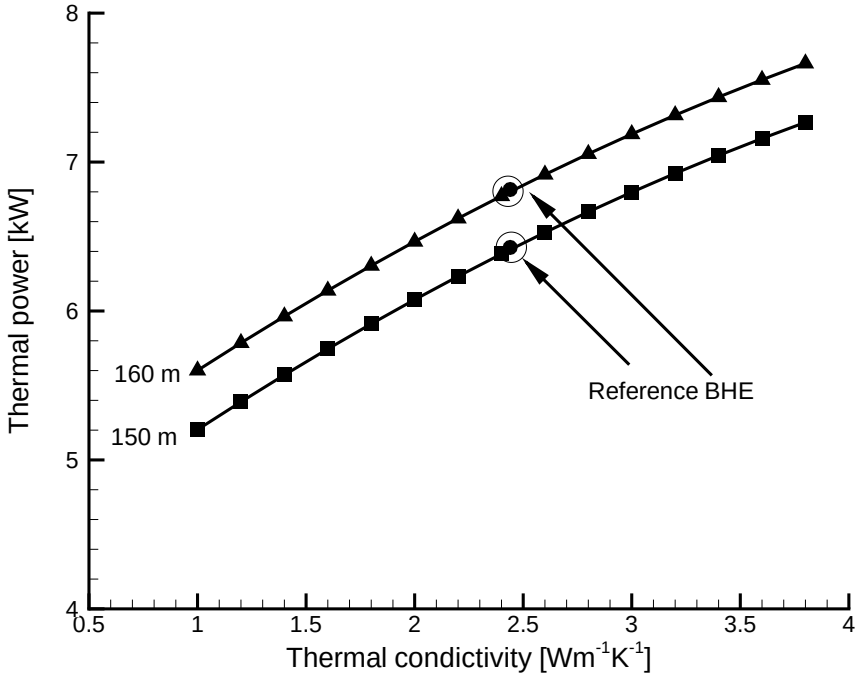

Figure 7-2: Thermal power of the 150 m and the 160 m deep BHE as a function of the thermal conductivity for the conditions given in Chapter 7.1. The circles represent the thermal power of the reference model run.

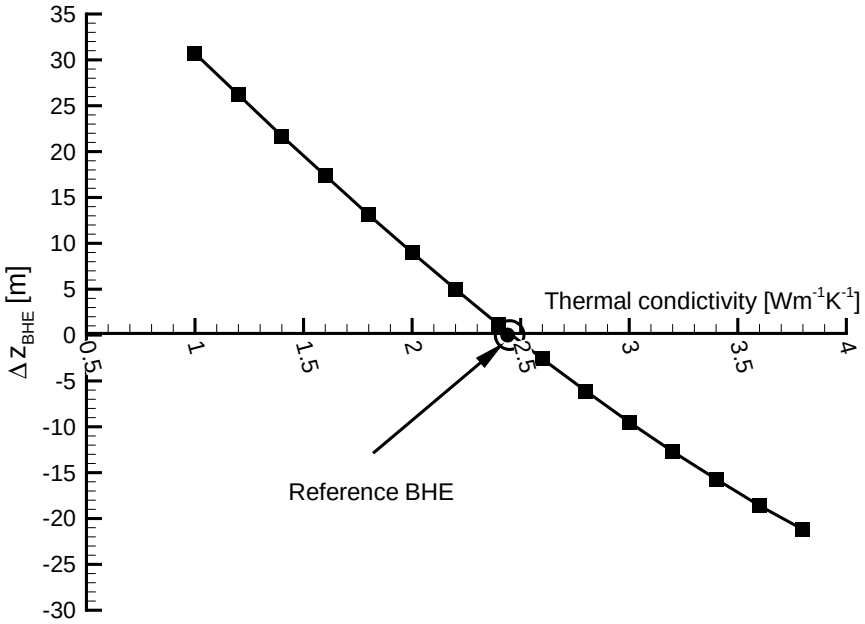

Figure 7-3: Drilling meters, which have to be additionally drilled or which can be saved at a specific thermal conductivity to achieve the same thermal power than the reference BHE indicated by the circle.

Applying Eq. 7-1, the influence of thermal conductivity on the BHE length can be determined for any arbitrary location using this relationship. Thus, regions of higher geothermal potential for this specific geothermal heat pump application can be identified. This will be illustrated for a thermal conductivity model for the city of Zürich. Andenmatten and Kohl (2003) developed a three-dimensional geological model based on geological borehole profiles (see Figure 7-4, from the cantonal office Amt für Abfall, Wasser, Energie und Luft) using the GIS-program GoCAD. The geological column is subdivided into Quaternary Layers, Upper Freshwater Molasse and Upper Marin Molasses. For every geological unit the thermal conductivity can be estimated by the software SwEWS (Leu et al., 1999). The specific local values were attributed to the individual geological layers in the 3D model and a map of the average thermal conductivity along the upper 150 m below Zürich was created. As illustrated in Figure 7-5, the average values in the area of Zürich vary between 1.8 W $m^{-1}K^{-1}$ and 2.8 W $m^{-1}K^{-1}$, reflecting the thermal conductivity variation of Quaternary Layers (λ= 1.8 W $m^{-1}K^{-1}$), Upper Freshwater Molasse (λ= 2.5 W $m^{-1}K^{-1}$), and Upper Marin Molasses (λ= 2.8 W $m^{-1}K^{-1}$). The areas with low thermal conductivity correspond to the area of significant Quaternary cover. Generally the thermal conductivity increases with depth. Chapter 6.3.5 shows that in this case and for heat extraction (heating mode) the average thermal conductivity is a valid approximation for the different thermal conductivities along the BHE. Using Eq. 7-1, the thermal conductivity map can be transformed into a map depicting the difference in drilling meters with respect to the 150 m reference BHE. This drilling depth represents the same thermal power all over the city after the first operational year under pure diffusive thermal conditions. The drilling depths range from -6 m to +10 m. Clearly this presents a procedure that should be applied to other areas where more significant influence of thermal conductivity is expected. However, as Figure 7-3 shows, Δz_{BHE} may change +/- 30 m in the Swiss Alpine Foreland in regard to the reference BHE.

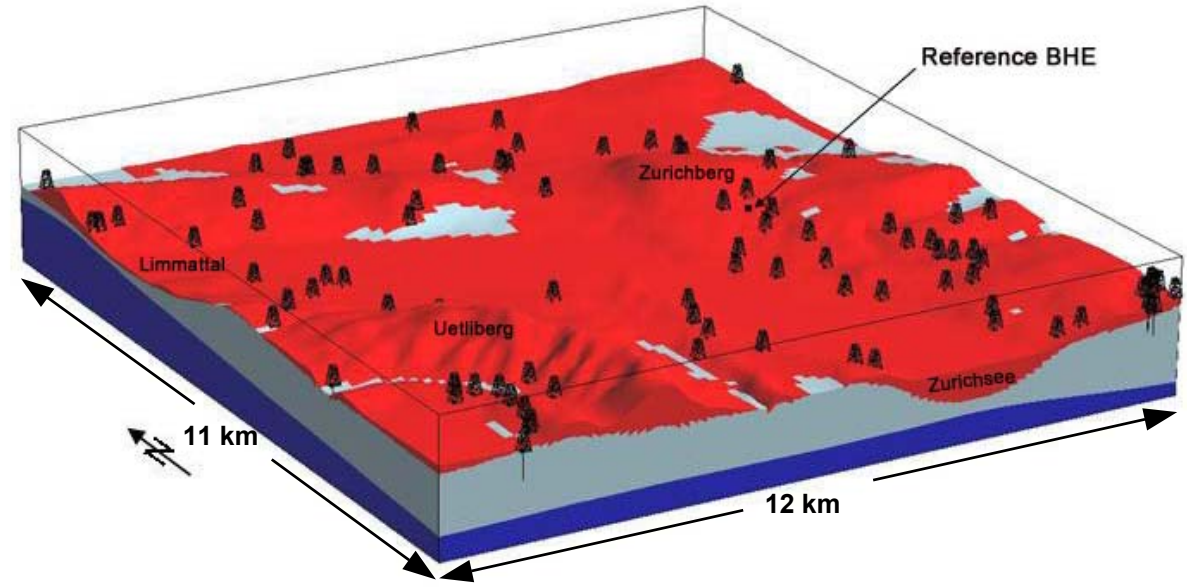

Figure 7-4: 3D geological model for the city of Zürich (Andenmatten and Kohl, 2003). Quaternary Layers are in red, Upper Freshwater Molasse in gray and Upper Marin Molasses in blue. The topography is scaled by a factor of 2. The reference 150 m BHE is indicated with a dot. The drilling derricks represent the BHE locations with known geological profiles.

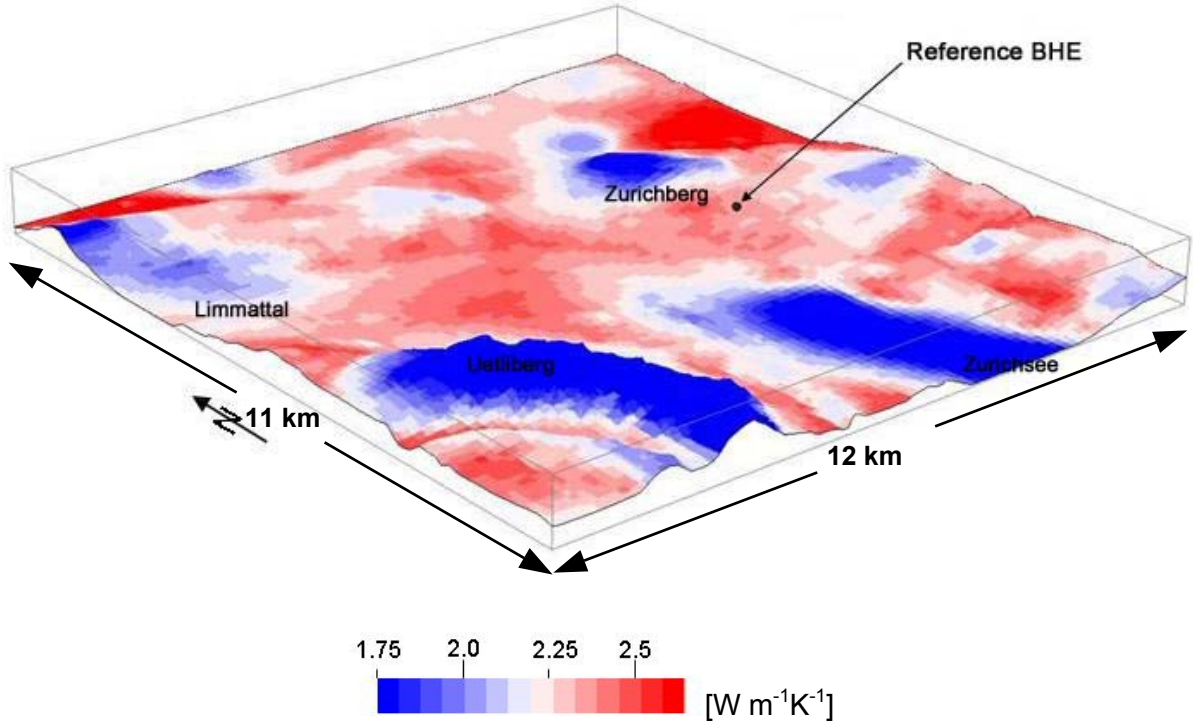

Figure 7-5: Average thermal conductivity along the first 150 m below the city of Zürich. The thermal conductivity values are plotted on the topography scaled by a factor of 2. The reference 150 m BHE is indicated with a dot.

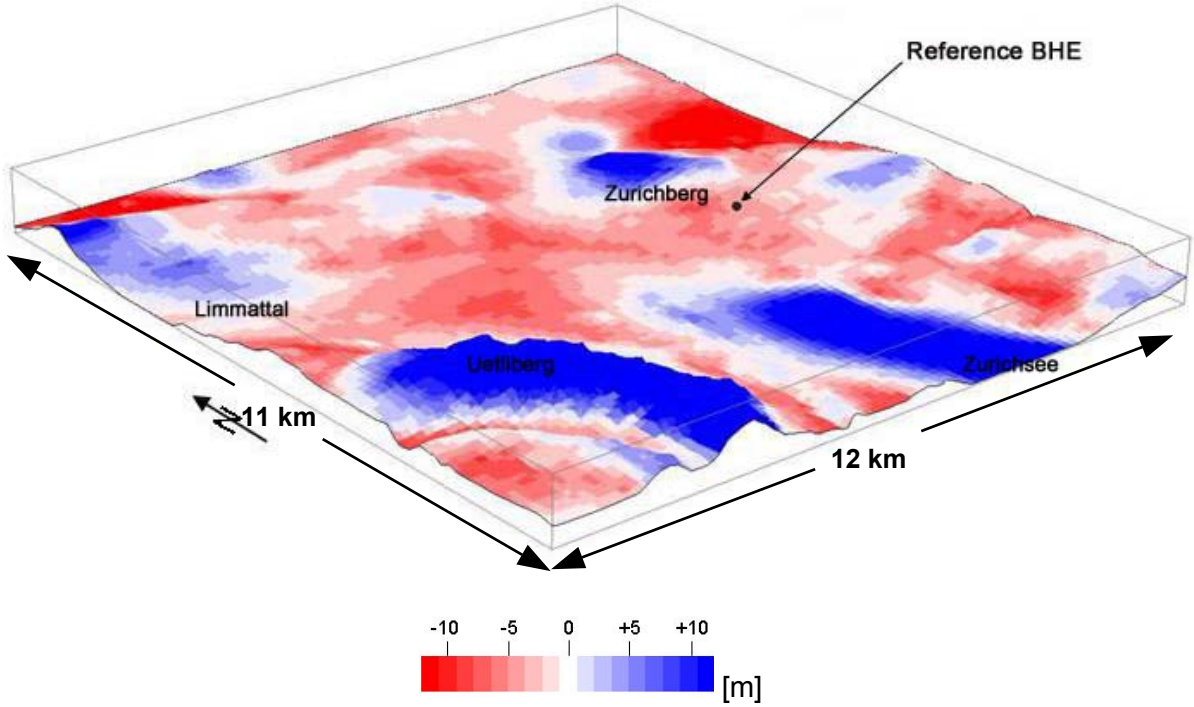

Figure 7-6: Difference in drilling meters with regard to the 150 m reference BHE located at the site of the Swiss Meteorological Institute to achieve the same thermal power at every thermal conductivity after the first operational year (see Figure 7-5). The drilling meter values are plotted on the topography scaled by a factor of 2.

7.3 Influence of Topography

In modestly undulating areas as in the Alpine Foreland, the topographical effect on the subsurface temperature field can be mitigated by the influence of the GST (Kurmann, 2003). Since GST decreases with altitude, the heat content stored in the subsurface is also diminished. As a consequence, BHEs must be drilled deeper at high altitudes to provide the same thermal energy production. Analogous to the previous chapter, the influence of the annual mean GST on the thermal power production is investigated with GST varying between 5 °C and 15 °C in the first year of operation under pure diffusive thermal conditions. This equals roughly an altitude range from 0 up to 2000 m a.s.l. (see Figure 5-3). As Figure 7-7 shows, the thermal power increases linearly with the GST from 3.4 kW (22 W per meter) at 5 °C to 8.5 kW (56 W per meter) at 15 °C for the 150 m deep BHE. This is ~500 W per 1 K (~200 m). For the 160 m BHE, the increase is again linear, but the slope is different. Calculating the difference between the two straight lines shows that higher the GST is, the more power can be extracted by drilling 10 m deeper. This is due to the higher difference between the heat carrier fluid and the surrounding rocks for higher GST

(note constant T_{in}= 1 °C), allowing a higher amount of heat to be extracted from the subsurface. 10 m deeper boreholes will increase the thermal power extraction by ~200 W at GST= 5 °C and by ~490 W at GST= 15 °C. The change in GST may be compensated by the following change in drilling meters, Δz_{BHE}, expressed by the following best fit 3rd order polynomial and illustrated in Figure 7-8 relatively to the reference BHE:

Eq. 7-2 $$\Delta z_{BHE} = -0.08 \cdot GST^3 + 3.47 \cdot GST^2 - 60.7 \cdot GST + 352.8$$

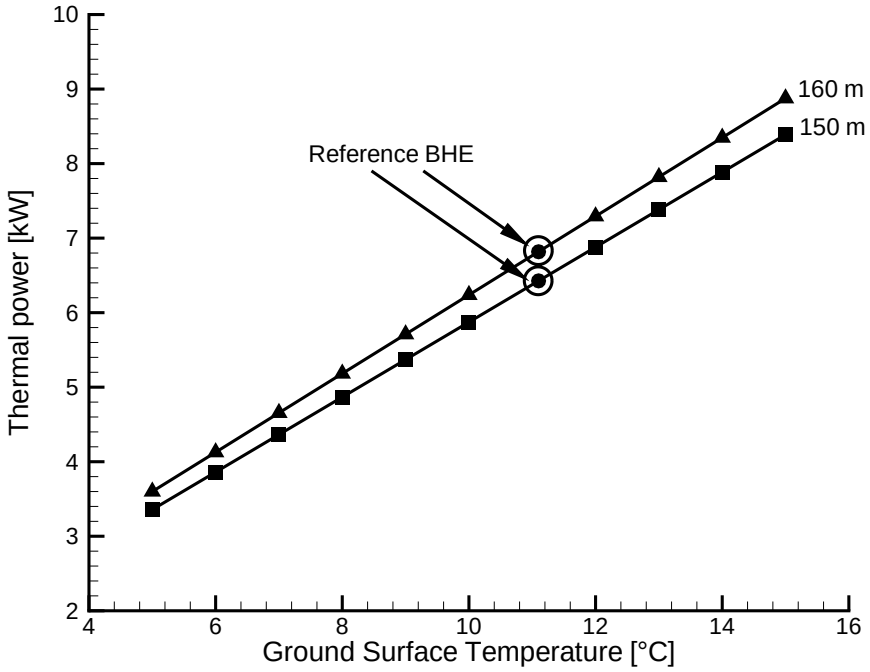

Figure 7-7: Thermal power of the 150 m and the 160 m deep BHE as a function of the GST for the conditions given in Chapter 7.1. The circles represent the thermal power of the reference model run.

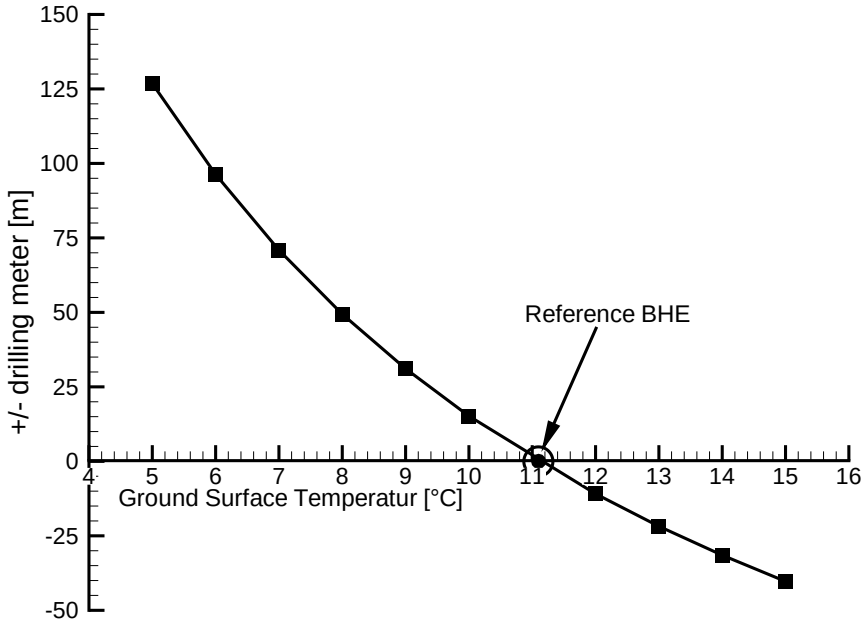

Figure 7-8: Drilling meters, which have to be additionally drilled or which can be saved at a specific GST to achieve the same thermal power than the reference BHE indicated with the circle.

Eq. 7-2 is now applied to the GST map in Figure 5-5. This map is only valid for modestly undulated regions, and not in the High Alps. Thus, the influence of GST on the drilling depth cannot be investigated all over Switzerland. Figure 7-9 shows that depending on the region, a maximum of 30 m of drilling can be saved relative to the reference model at the Swiss Meteorological Institute in Zürich, or in other regions BHEs must be drilled up to 100 m deeper at the end of the first operational year. Equal to the GST, the needed drilling meters are generally altitude-dependent. A GST decrease from 11 °C to 9 °C (altitude change from ~500 m to ~1000 m a.s.l.) requires 20 % deeper BHEs. This highlights the importance of an expert design of BHE systems, especially at higher altitudes. Considering simply the GST conditions in Switzerland, Ticino and the area around the cities of Geneva and Basel are most promising regions. However, broad parts in the Swiss Alpine Foreland, the most densely populated area with the highest demand for BHE, show good conditions for geothermal energy use with nearly identical borehole length necessary to supply the same amount of energy.

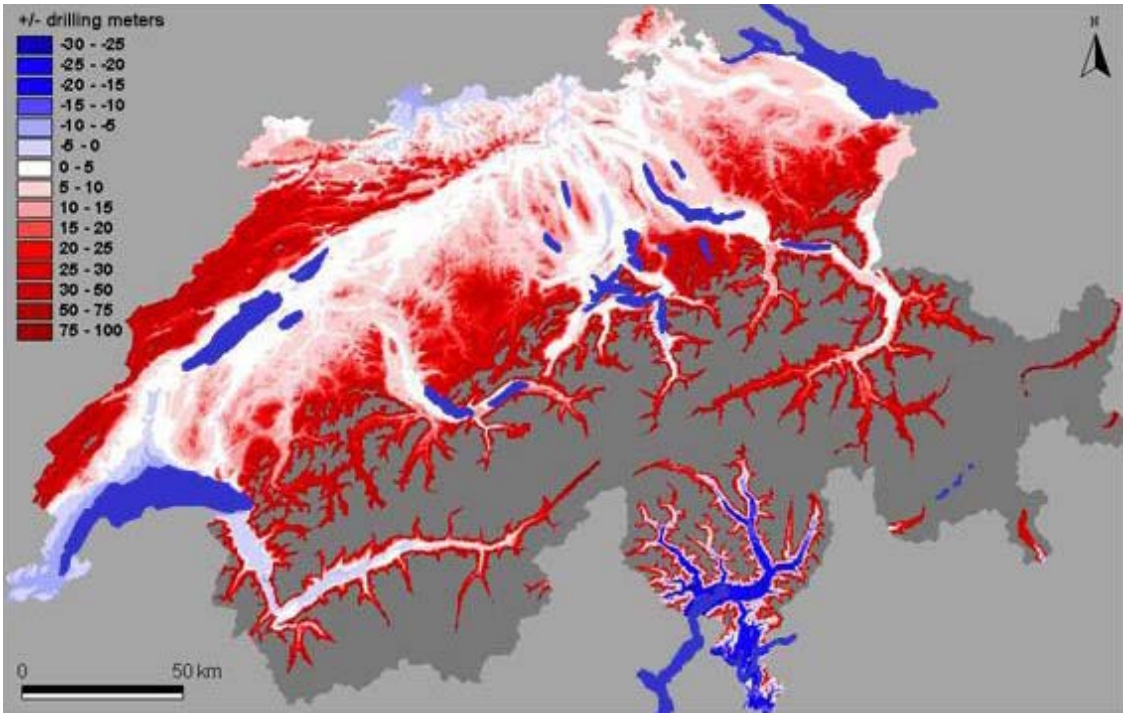

Figure 7-9: Difference in drilling meters with regard to the reference BHE located at the site of the Swiss Meteorological Institute to achieve the same thermal power at GST after the first operational year (see Figure 7-8).

7.4 Discussion

Thermal output of BHEs is dependent upon thermal conductivity of the subsurface and GST. The applied procedure allowed estimating the relations between the thermal power and thermal conductivity on one hand and GST on the other hand. The results may be extrapolated to other areas and can be applied to geothermal prospecting studies. These studies showed that for the values expected in Switzerland, the GST will have a higher impact on the power production than the thermal conductivity. However, in the most densely populated regions in the Swiss Alpine Foreland the site conditions may not change dramatically from one place to the other. Transforming their impact into BHE drilling depth, the variation may the ±20 % under the assumed modeling conditions (±15 m for variations in GST and ±15 m for variations in thermal conductivity).

The study considers the situation after the first year of operation. The efficiency of a BHE system will decrease during the following operational years (see also below in Chapter 8). The subsurface will cool down successively in the in the following years until a new steady-state is reached, and the influence of the thermal conductivity which defines the rate by which the energy can radially flow to the BHE, will become

more significant. For sites with lower thermal conductivity, the degradation will be pronounced, and should be considered in the original design. Future studies should cover several years of operation to quantify this effect.

The investigations presented here were performed for pure diffusive thermal subsurface conditions. Advection of heat by moving groundwater would have a significant impact on the thermal power (see also Chapter 6.3.5). However, the hydrogeological subsurface conditions and their effect on the BHE power production are difficult to simulate. In general, moving groundwater improves the performance of a BHE system, although if the BHE system is also used for heat storage purposes during summer, the groundwater flow may have a negative impact on the performance.

8. SUSTAINABILITY OF BHE SYSTEMS

8.1 INTRODUCTION

About a decade ago the Swiss Federal Government initiated significant steps in the energy police like the action plan ENERGIE2000 (Rybach and Gorhan, 1997) which included developments towards the utilization of indigenous and environmentally friendly forms of energy. Special emphasis was on renewable energy source.

In this context questions on sustainability and renewability of BHE systems are often raised: 1) can the production level be sustained over long time periods (decades/centuries) and 2) will the ground temperature recover within reasonable time? Based on temperature measurements during the first four operational years, Wener et al (1996) were skeptical on the sustainability of BHE systems and suggested the possibility of a thermal collapse after several years of operation. This demanded for an extensive theoretical and experimental investigation of the long-term behavior of BHE systems to proof of the longevity of shallow low-enthalpy systems. For marketing this is especially important to be able to promote these systems.

Rybach and Eugster (2002) addressed the sustainability and renewability aspects of geothermal heat pump systems. In particular, the long-term performance of a single BHE system was analyzed by numerical modeling. The main result was that sustainable production can be achieved and that the ground around the BHE cools and recovers in an asymptotic manner: the cooling is highest at the beginning and slows down later asymptotically; recovery is also strong in the beginning and with time it levels off (Figure 8-1). However, nowadays the BHE installations are characterized by an increasing demand for BHE areas to supply a variety of larger buildings like multi-family houses, schools, factories, administration complexes etc. The number of BHEs in such arrays varies from a few to some hundred BHEs (Lund et al., 2003). Here, the mutual influence is important (see also Chapter 3.3.4). The continued growth of BHE installations depends upon customer confidence, and therefore the long-term stability of the BHE field must also be demonstrated.

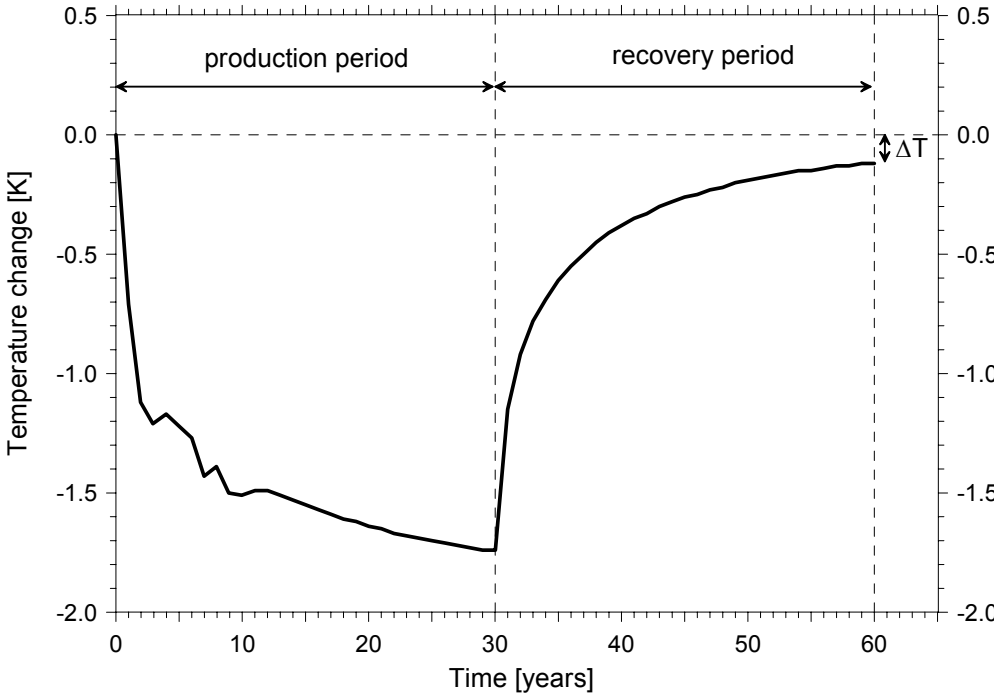

Figure 8-1: Ground temperature change at 50 m depth and at 1 m distance from a 100 m deep BHE; measured during the first 10 years of operation and calculated afterwards (Rybach and Eugster, 2002). After 30 years the recovery is almost total (ΔT = -0.1 °C).

Herein, we report the results of the model simulations on a BHE array (Signorelli et al., 2004). Various constraints (e.g. property size) often limit the spacing between BHEs, and due to mutual influences multiple BHEs provide less heat per BHE than a single BHE. In our analysis we first explore the thermal response of an individual BHE in the array and then treat the thermal effects of the whole array (6 BHEs, each 100 m long). Special attention is given to the BHE spacing. The analysis emphasizes the change in the subsurface temperature and discusses the array design in order to achieve the same production temperatures as a single BHE. The simulated period is for an operation of 30 years, followed by a recovery period of 70 years to estimate the time necessary for the subsurface system to return back to the original state.

8.2 FE MESH OF BHE ARRAYS

For the numerical model simulations, the FE mesh for six 100 m deep BHEs spaced by 7.5 m from Chapter 3.3.2 is taken. The assumed model and site conditions correspond to those in Table 3-1. A total runtime of 1'800 hours per year is applied (heating mode only), subdivided into various runtimes per months as listed in

Table 3-4. As shown in Chapter 3.2.7, the simulated production temperature and the cooling of the subsurface resulting from the BHE operation depends on the load profile applied. But, comparing the subsurface temperature of the different load modes at the reference point at 31 August, as suggested in Chapter 3.2.7, the results of the subsurface cooling are independent of the load profile. Therefore, the "single load profile" from Chapter 3.2.7 is used for the simulations due to moderate calculation time. Furthermore, it was shown that the relative temperature change from one year to the following is nearly identical and thus independent of the load profile. Therefore, for the evaluation of fluid production temperature the "single load profile" can also be applied when the temperatures are compared relatively to each other. In the following one of the central BHEs of the array with the highest mutual influence is always taken for the comparison.

8.3 BHE SPACING AND SUSTAINABILITY

8.3.1 EFFECT OF SPACING

A practitioner's rule of thumb says that spacing should not be less than 8 m. Kälin and Hopkirk (1991) investigated the mutual influence for two neighboring BHEs. They report that with a spacing of 15 m there is no noticeable influence. On the other hand, with a spacing <5 m the influence is so strong that the system operation can break down (permafrost at the BHE!). The situation is better for a BHE field in flowing groundwater. These results correspond well to the findings of Pahud et al. (2002). Moreover, they showed that lower ground thermal conductivity introduces a larger long-term influence, resulting in higher mutual influences than for high thermal conductivities.

To get a more precise hold on the mutual effect of neighboring BHEs the modeling has been performed by varying the spacing in the 6-BHE array between 3 and 15 m. Figure 8-2 compares the relative difference in minimum outlet temperature between the single BHE and the borehole fields over the first three years of operation. Analogous to Kälin and Hopkirk (1991), no significant effect results for BHE spacing of 15 m, but strong influences are visible for spacing shorter than 5 m (up to ~5 K difference). For the 7.5 m-spaced array the mutual influence is still clearly noticeable. This indicates that a BHE in an array must be drilled deeper to achieve the same efficiency as a single BHE. It must be emphasized that production temperatures

below –5 °C can cause mechanical damage of the BHE backfill and thus destroy the thermal contact between the heat exchanger pipes and the surrounding ground.

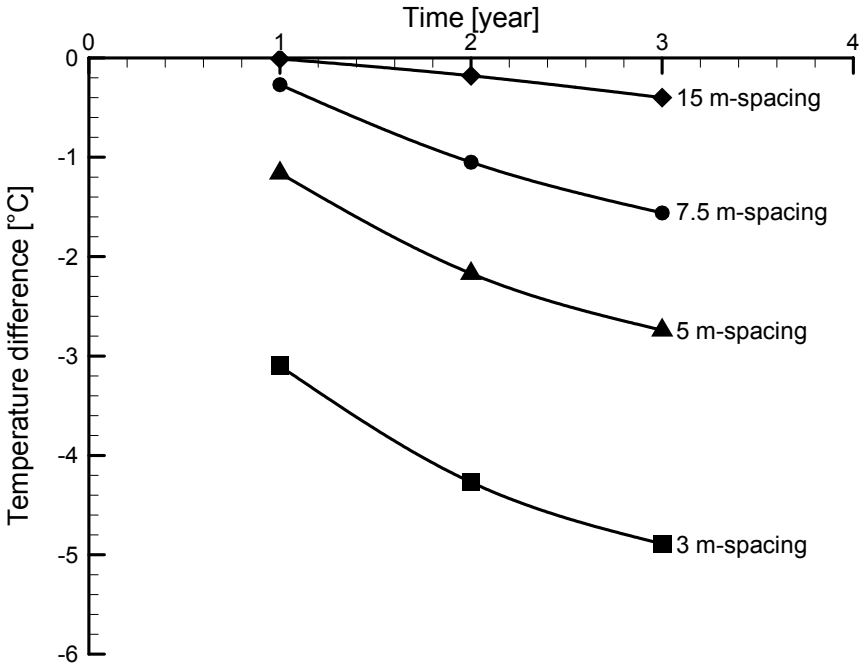

Figure 8-2: Temperature difference of the produced outlet fluid temperature of BHE fields relative to the single BHE.

8.3.2 COMPARISON SINGLE BHE / BHE FIELD

In this section, the sustainability of the single BHE and the 7.5 m-spaced BHE field is investigated. Both BHE arrangements are simulated for an operation of 30 years, followed by 70 years of recovery. Thereby, the central BHE of the field with the highest mutual influence is compared to a single BHE. Figure 8-3 shows the ground temperatures for both model runs. The temperature changes exhibit the same asymptotic behavior as described in Rybach and Eugster (2002): The cooling is strong at the beginning and levels off at later times. The subsurface temperature field stabilizes at a lower temperature level and no thermal collapse occurs. The same behavior results for the recovery period. Due to the mutual influence of BHEs in a field the ground cooling is significantly more pronounced than around a single BHE with no neighbors. The recovery of the BHE field takes 70 years, whereas for the single BHE, the deviation to the initial temperature field is <0.1 K after 24 years.

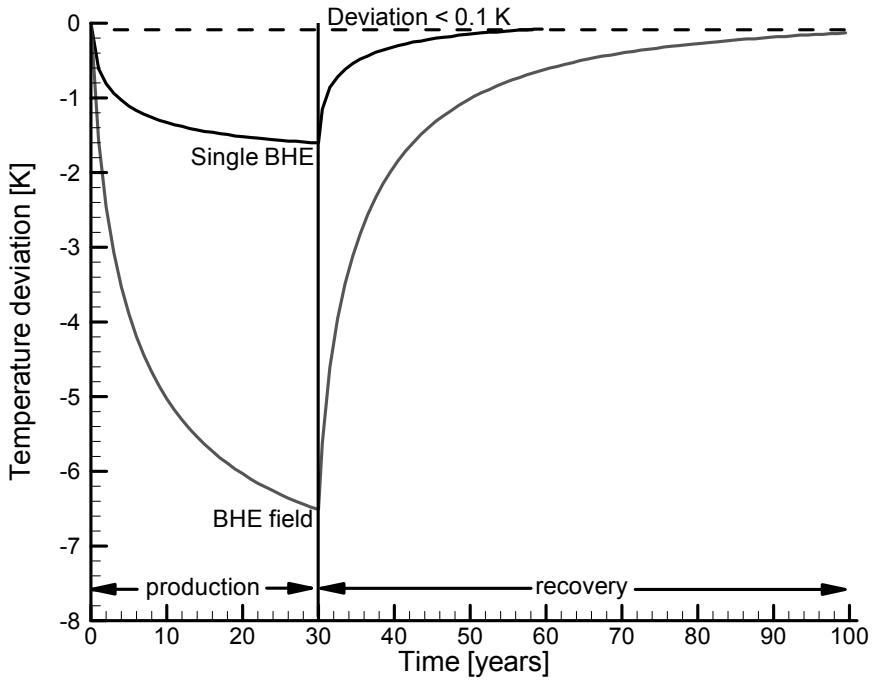

Figure 8-3: Ground temperature changes in 50 m depth at 0.1 m distance from the BHE(s), over a 30 year production and a 70 year recovery period. The temperatures are plotted at the end of August, for the single BHE and for the BHE field with 7.5 m spacing relative to the initial temperature of 12.7 °C. The curve for the BHE field represents the temperature evolution of the central BHE with the highest mutual influence.

8.3.3 Compensation through Additional BHE Lengths

The thermal production power of the array with 6 BHEs is taken to be six times that of a single BHE, i.e. in our case 6 x 5 kW (see Table 3-1). But the mutual influence of the neighboring BHEs leads to lower ground temperatures and correspondingly lower fluid outlet temperatures (see Figure 3-16). The lower temperatures can be compensated for the 7.5 m spacing by longer BHEs. Figure 8-4 shows the deviation of the minimum fluid temperature in the center BHE for various additional BHE lengths up to 50 m, relative to the single BHE, during the first 10 years of operation. Drilling the BHE field deeper by ~30 % yields the same fluid temperature than the single BHE after 10 years of operation. It can be recognized from Figure 8-4 that the temperature decrease slows down with time and the difference in fluid outlet temperature between year 9 and 10 is less than 0.1 K. Therefore, no significant changes must be expected during further operation.

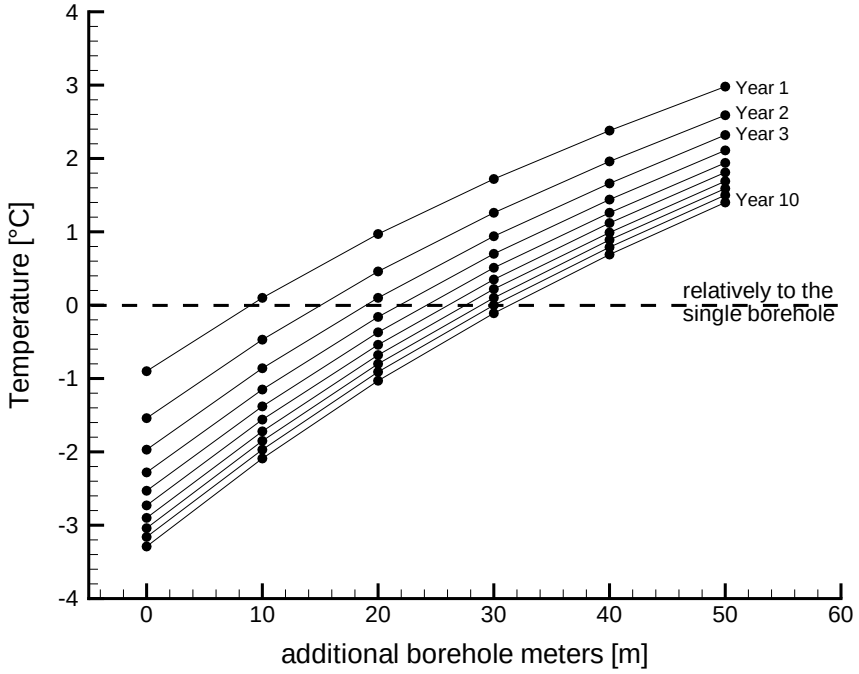

Figure 8-4: Difference between single BHE and BHE field fluid production temperatures during the first 10 years of operation, in function of additional drilling meters. To achieve the same fluid temperature as the single BHE, additional drilling meters of > 30 % are needed for a field with 6 BHEs of 100 m length and 7.5 m spacing.

8.4 CONCLUSIONS

It could be verified that the long-term thermal performance of BHE fields shows the same general behavior as a single BHE. Heat extraction from BHEs increasingly cools the surrounding ground during operation, and the subsurface ground temperature recovers during shut-down due to strong temperature gradients created by the BHE heat sink. Cooling and recovery are asymptotic. The cooling is highest at the beginning and slows down later; recovery is also strong in the beginning and with time it levels off. The recovery duration for a single BHE roughly equals that of operation: After 30 years of operation, the thermal recovery of the ground needs ~30 years (see also Rybach and Eugster, 2002). For BHE fields, the recovery time is longer, approaching ~70 years. The model simulations for single and multiple BHE systems prove that sustainable heat extraction can be achieved and that subsurface temperature recovers from the BHE operations. In fact, the BHEs show stable and reliable performance which can be considered renewable.

The spacing in a BHE field is a critical factor: the mutual influence of neighboring BHEs leads to lower ground temperatures and fluid production temperatures than for a single BHE under the same load. The minimum spacing should not fall short of ~7 m even in ground with high thermal conductivity (>3 W $m^{-1}K^{-1}$) in order to provide sustainable production. Additional drilling meters provide feasible help: drilling the BHE 7.5 m-spaced field deeper by ~30 % yields the same fluid temperature as for the single BHE. This report illustrates that sustainable production from a BHE field can be achieved by proper design.

9. CONCLUSIONS AND OUTLOOK

Understanding the behavior of shallow low-enthalpy systems is a complex undertaking. The proper solution requires the development of numerical modeling tools to realistically simulate the geothermal reservoir and to evaluate the long-term behavior of the system. Geoscientific investigations ranging from determination of petrophysical parameters to subsurface temperature levels provide the basis for such modeling. This work investigates a wide range of topics with regard to borehole heat exchangers (BHE), many of them for the first time. The conclusions strive for a better understanding and dimensioning of shallow low-enthalpy systems. Many of the conclusions can be applied directly to engineering and practical applications. This emphasizes the important link between general geoscientific research and energy-resource development.

9.1 NUMERICAL SIMULATION

Various software tools are available to simulate BHE systems, but generally the software simplifies the system into 2D. Realistic simulation of a basic BHE layout (four tubes grouted in a borehole with circulating fluids) clearly requires 3D treatment. Therefore, the 3D FE model FRACTure was introduced and used for this study.

The accuracy of any numerical calculation depends on the correct model setup. The sensitivity of the temperature simulation in and around the BHE on the model parameters is therefore systematically investigated. A fine spatial mesh in the immediate surrounding of the BHE (<1 m) turned out to be essential for the exact calculation of the production temperature of a BHE system. Fine discretization in time is only necessary for the simulation of the exact temperature evaluation in the first hour. Thus, when only the long-term behavior is of interest, coarse time increments are sufficient. Furthermore, the influence of different load profiles on the temperature of the subsurface was investigated and the results suggest that the subsurface cooling and recovery is independent of the load profile. Also, it was illustrated that the relative temperature change from one year to the following is identical and thus independent of the load profile. Although the numerical simulation procedure was illustrated only for BHE systems, the results about the necessary

discretization and the effect of load time functions are universally valid for shallow low-enthalpy systems such as foundation pile systems for example.

In the past, analytical models were preferred to numerical simulations mainly due to the high CPU-times required. Nowadays, with the powerful computers available, numerical models are increasingly competitive for BHE design. Nonetheless, building up an FE mesh is still time-consuming even with the semi-automated WinFra program. A fully-automated WinFra program would significantly reduce the time-consuming steps. A library could be set up with standard borehole configurations which then would allow an engineer to easily insert typical BHE configurations into arbitrary FE meshes and so make modeling faster.

For a simple heating mode scenario, the FRACTure simulations were compared to calculations by the semi-analytical EED software. Overall good agreement was achieved. Combined heating and cooling BHE systems are increasingly popular and here it is highly important to optimize the different operation modes with each other. In EED, the definition of load profiles is strongly limited to simple base and peak loads. It is questionable if these rough load profiles are sufficient for combined heating and cooling applications. Therefore, the thermal long-term behavior of BHE systems for combined heating and cooling should be investigated in detail. For this purpose, numerical models like FRACTure are particularly suitable, since they allow the combination of heating and cooling during arbitrary operational cycles.

9.2 GEOSCIENTIFIC INVESTIGATIONS

A sophisticated simulation and understanding of shallow low-enthalpy systems requires a precise knowledge of the subsurface temperature field. The temperature field is influenced by a variety of factors like the thermal and hydraulic properties of the subsurface rocks, and the conditions at the ground surface. Therefore, experience in petrophysics and hydrogeology is important for determining these factors. Key parameters for developing low-enthalpy reservoirs are the ground surface temperature (GST), the thermal conductivity of the subsurface rocks, and an understanding of the possible in-situ errors when estimating these parameters.

Evaluating GST is common in applied and general geothermal research. The focus here was investigating GST for Switzerland because of its well-known impact on BHE utilization. For the first time the GST of Switzerland was investigated

systematically with respect to the regional differences. The GST analysis suggests that the recent climate change is more pronounced in Alpine regions than in the Alpine Foreland. The GST is altitude dependent and the relationship between GST and the surface air temperature (SAT) was scrutinized closely. A non-linear fitting approach was applied, and this allowed establishing zones of different altitude dependences. In the altitude range between 200 and ~1000 m a.s.l., the difference between GST and SAT is nearly constant (~1.6 K). Above that interval, the difference increases. This effect could be related to the influence of sub-zero SAT. Also, the relationship between GST and surface exposure was investigated. Contrary to previous publications (Blackwell et al., 1980, Šafanda, 1999), no universal correlation between GST and surface exposure was found, due to local and rapidly changing meteorological conditions.

By further processing, an existing SAT map was converted into the first GST map of Switzerland, which was then verified by GST values extrapolated from boreholes. The new GST map of Switzerland provides useful estimates of regional GST, but not for local effects. The resolution can be improved by additional ground-truth from GST-stations. However, the GST map represents an important improvement in evaluating geothermal resources and determines regional GST distribution for conditions typical of Central Europe.

Recently, it has become popular to measure in-situ thermal conductivity by thermal response tests evaluated generally by a line source analysis. However, until now, no systematic study has been performed to investigate the reliability of this method. Therefore, FRACTure simulations were performed to estimate the accuracy of line-source test interpretation and to provide information about the necessary test duration. Herein, effects of heterogeneous subsurface conditions, groundwater movement, and of variable data quality were presented. It was shown that the deviation from the model parameter can exceed 10 %. Most often the estimated value is an underestimation of in-situ thermal conductivity resulting in an over-dimensioning. At large BHE fields, such a “conservative” design could have a large financial impact on cost-effectiveness.

This comparison to measured data also demonstrated the benefit of using numerical models for evaluating thermal response tests rather than an analytical line source model. The line source approach showed high variation in the evaluated thermal

conductivity, depending on the time interval analyzed. The numerical analysis calculates individual thermal conductivities for every time step, and even allows the identification of the influence of ambient temperature, which may play a role in the in-situ thermal conductivity determination.

The largest handicap of thermal response tests is that they take at least several days to complete and are therefore expensive. A wireless borehole probe has recently been developed for continuous temperature profiling in BHEs (Rybach et al. 2003) which may help to lower costs for thermal response tests. Based on the temperature log along a BHE and the terrestrial heat flow from the heat flow map of Switzerland (Medici and Rybach, 1995) the in-situ thermal conductivity can be estimated. A measurement run in a 300 m deep BHE can take less than 30 minutes. This procedure is now generally tested at different locations in Switzerland.

Such temperature measurements could be utilized for more general scientific and geological understanding of subsurface conditions, possibly unrelated to BHEs. In this context, groundwater-influenced thermal response tests could be used for hydrogeological applications. The idea is to apply the temperature response as a tracer for groundwater flow. Normally, borehole cuttings are available, and from laboratory measurements the thermal conductivity can be determined, and from drilling data, the thickness of the aquifer can be derived. Implementing all this available subsurface information into a numerical model, the hydraulic properties and conditions can be acquired by fitting the actual temperature data to the simulated data without further field tests.

9.3 PRODUCTIVITY INVESTIGATIONS

One application of geoscientific research is determining the productivity behavior of the low-enthalpy systems. This can be ether done by either by sensitivity testing of simulated data or by analyzing measured system data.

Using two sensitivity studies, the influence of GST and thermal conductivity on the performance of a single BHE system was quantified for different locations in Switzerland. The investigation showed the high impact of GST on the power production at high elevations, which require sophisticated dimensioning. The most populated area in the Swiss Alpine Foreland shows generally good conditions for the use of low-enthalpy systems. GST as well as thermal conductivity may not vary

significantly from location to location. This result is significant for general low-enthalpy prospecting studies. Combining the two sensitivity studies, a further investigation concerning the influence of the local heat flow pattern or ground water flow, it is possible to identify relevant geothermal areas. This investigation was only performed for one operational year, but it can be expected that the thermal conductivity, which defines the rate by which the energy can radially flow to the BHE, will become more significant during the following operational years. Future research should therefore be focused on the investigation of the long-term behavior.

The sustainability and renewability of large BHE systems continue to be a controversial subject. Herein, it was verified that the long-term thermal performance of BHE fields shows the same general behavior as a single BHE: the cooling is strong in the beginning and slows down later asymptotically; recovery is also strong in the beginning and levels off with time. In a BHE field the subsurface cooling is stronger and the recovery time is longer than for a single BHE. Furthermore, the spacing in a BHE field turned out to be a critical factor. The minimum spacing should not fall short of ~7 m in order to provide sustainable production. The presented investigation concluded that sustainable production from a BHE field can be achieved by proper design. However, the production from a center BHEs of a BHE field is lower than that of a BHE at the border due to the higher reciprocal influence. The lower fluid production temperature in the BHE field may be compensated by additional drilling meters. Further studies should commence to investigate to quantify the efficiency of center BHEs and to provide information how to improve BHE fields. This should be performed by numerical models which allow treatment of individual BHEs in any area.

The numerical interpretation of measurements during the BHE start-up quantified the effect of the pipe location inside the borehole. The simulations suggest a peripheral location with the tubes maximally separated in the data set. The minimum separation may be a coincidence. However, the peripheral location may generally be true in practice. Due to the tube installation from a windlass, the tubes are expected to be located at the periphery of the borehole with direct contact to the surrounding rock matrix. Thus, the insulation of the grouting material with its relatively low thermal conductivity would have a negligible influence, and only the interaction between the tubes would be important for the production temperature. To reduce this mutual

influence, tube-spacers are promoted in practice. But, spacer-separated BHEs are more expensive, since the spacer must be manually installed by the drilling staff which significantly increases the drilling time. Furthermore, it must be considered that for spacer-separated tubes, not all tubes are located at the periphery, and the insulation of the grouting may influence the BHE behavior. This investigation showed that the numerical simulations for the two extreme peripheral tube locations showed only a difference of ~1 K, and questions the benefit of the spacers.

A more rigorous test with other measurements should be performed to determine whether the assumption for a general peripheral tube location is adequate. For this purpose, other temperature measurements of good quality and with a high sampling rate must be available for the first operational cycle. Such measurements are often difficult to obtain (Signorelli et al., 2003). Parallel to this analysis, the thermal behavior of spacer-separated tube models should be simulated and compared to model runs for peripheral tube locations. This can be easily done using FRACTure.

REFERENCES

Abegg, B, 1996. Klimaänderung und Tourismus. Klimaforschung am Beispiel Wintertourismus in den Schweizer Alpen. NFP 31, Schlussbericht. vdf Hochschulverlag an der ETH Zürich.

Andenmatten Berthoud N., Kohl T., 2003, Geothermische Ressourcen, Erarbeiterung und Bewertung des geothermische Potentials der Schweiz – Endbericht, Bundesamt für Energie.

Austin, W.A., 1998. Development of an in situ system for measuring ground thermal properties. Master of Science Thesis 1998, Oklahoma State University, Stillwater, Oklahoma.

Austin, W.A., Yavuzturk, C., Spitler, J.D., 2000. Development of an in situ system for measuring ground thermal properties. ASHRAE transactions, Vol. 106 (1), 356 – 379.

Baumgartner, W., 1999. Neue Wärmepumpenstatistik: 53'00 elektrische Wärmepumpen in Betrieb. Bulletin des Schweizerischen Elektrotechnischen Vereins und des Verbands Schweizerischer Elektrizitätsunternehmen, Nr. 24/99, S. 9-12.

Bassetti, S., 2003. 3D Simulationen von geothermischen Response Tests. Diplomarbeit am Institut für Geophysik der ETH Zürich.

Bendel, L., 1948. Ingenieurgeologie. Springer, Berlin.

Bennett and Myers, 1982. Momentum, heat, and mass transfer. Third ed., Wiley, New York.

Berkowicz, R., Prahm, L.P., 1982. Sensible heat flux estimated from routine meteorological data by the resistance method. J. Appl. Meteorol. 21, 1845 – 1864.

Blackwell D.D., J.L. Steele & Ch.A. Brott, 1980. The terrain effect on terrestrial heat flow. Journal of Geophysical Research, B85 (9), 4757-4772.

Brehm, D.R., 1989. Entwicklung, Validierung und Anwendung einer dreidimensionalen, strömungsgekoppelten finite Differenzen Wärmetransportmodells. Giessener Geologische Schriften 43, 120 S., Lenz-Verlag, Giessen.

Brenni, R., 2000. Modellsimulationen von Tiefenerdwärmesonden-Anlagen n den Fallbeispielen Weggis und Medyaguino. Diplomarbeit am Institut für Geophysik der ETH Zürich.

Burkart R., Hopkirk R.J., Eugster W., Rybach L., (1989): Erdwärmesonden-Heizanlagen: Durch Messungen und Berechnungen bestimmte Auslegungs- und BetriebsgrÄssen. Schriftenreihe des Bundesamtes für Energiewirtschaft, Bern, Studie Nr. 46, 55 S.

Busslinger, A., 1994. Numerische Modellierung einer Erdwärmesonden–Testanlage. Diplomarbeit am Institut für Geophysik der ETH Zürich.

Busslinger, A., Rybach, L., 1999. Predicting rock temperature for deep tunnels, Tunnel, 1, 24 - 32.

Carslaw, H.S., Jaeger, J.C., 1959. Conduction of heat in solids. 2nd ed., Oxford Univers. Press, London.

Chiasson, A., Rees, S.J., Spitler, J.D., 2000. A preliminary assessment of the effects of ground-water flow on closed-loop ground-source heat pump systems. ASHRAE transactions, Vol. 106 (1), 380 – 393.

Clauser, C., 1988. Untersuchungen zur Trennung der konduktiven und konvektiven Anteile im Wärmetransport in einem Sedimentbecken am Beispiel des Oberrheingrabens. PhD Thesis. Fortschritts-Berichte VDI, Reihe 19, Nr. 28, VDI Verlag, Düsseldorf.

Clauser, C., Huengens, E., 1985. Thermal conductivity of rocks and minerals. In: T.J. Ahrens (Edt.), Rock physics and phase relations – A Handbook of Physical Constants, AGU Reference Shelf, 3, American Geophysical Union, USA, p. 105 – 126.

Cleasson, J., Eskilson, P., 1987. Conductive heat extraction by interacting deep boreholes. Department of Mathematical Physics, Lund University of Technology, Lund, Sweden.

Cleasson, J., Eskilson, P., 1988. Conductive heat extraction to a deep borehole. Thermal Analysis and Dimensioning Rules. Energy 13/6, 509-527.

Claesson, J., Hellström, G., 2000. Analytical studies of the influence of regional groundwater flow on the performance of borehole heat exchangers. Proc. of the 8th International Conference on thermal energy storage, Terrastock 2000, 28 August – 1 September 2000, Stuttgart, Germany, 195 – 200.

Defila, C., Brändli, J., 1989. Bodentemperaturen und Verdunstung, 1951 – 1985. Klimatologie der Schweiz Heft 28 P. Beiheft zu den Annalen der Schweizerischen Meteorologischen Anstalt (Jahrgang 1986)

Dubbel (2001). Taschenbuch für den Maschinenbau. - 20. Neubearbeitete und erweiterte Auflage. Herausgegeben von W. Beitz und K.-H. Grote – Berlin, Springer.

Eklöf, C., Gehlin, S., 1996: TED – A mobile equipment for thermal response tests. Master of Science Thesis 1996:198E, Lulea University of Technology, Sweden.

Eskilson, P., 1986. Superposition borehole model. Manual for computer code. Department of Mathematical Physics, Lund University of Technology, Lund, Sweden.

Eskilson, P., 1987. Thermal analysis of heat extraction boreholes. Department of Mathematical Physics, Lund University of Technology, Lund, Sweden.

Eskilson, P., Cleasson, J., 1988. Simulation model for thermal interacting heat extraction boreholes. Numerical Heat Transfer, 13, 149 – 165.

Eugster, W.J., Rybach, L. (1999): How renewable are borehole heat exchanger systems? Proc. European Geothermal Conference Basel'99.

Eugster, W.J., L., 2002. Angewandte Forschung: Workshop zur Qualitätssicherung von „geothermischen Response Tests". Schlussbericht, Bundesamt für Energie.

Eugster, W.J., Laloui, L., 2002. Workshop: Geothermische Response Tests – Tests de Résponse Géothermique. Proceedings. Ecole Polytechnique Fédéerale de Lausanne.

Freeze, R.A., Cherry, J.A., 1979. Groundwater. Prentice-Hall, Inc., Englewood Cliffs, New Jersey.

Fujii, H., Akibayashi, S., Ohshima, K., 2002. Interpretation of thermal response tests in shallow deposits. Geothermal Resource Council Transactions. Vol. 26, September 22-25, 2002.

Gehlin, S., 2002: Thermal response test – Method development and evaluation. Doctoral Thesis 2002:39, Lulea University of Technology, Sweden.

Gehlin, S., Hellström, G., 2003. Comparison of four models for thermal response test evaluation. ASHRAE transactions, Vol. 109, 1 –12.

Gilby, G.J., Hopkirk, R., 1985. The coaxial vertical probe with solar recharge, numerical simulation and performance evaluation. Proc. 2nd WS on SAHPCS Vienna, 443 – 456.

Gruber, S., Hoelzle, M., Haeberli, W., 2004. Permafrost thaw and destabilization of Alpine rock walls in the hot summer of 2003. Geophys. Res. Lett. 31 (L13504).

Hellström, G., 1991. Ground heat storage: Thermal analyses of duct storage systems. Theory. Department of Mathematical Physics, Lund University of Technology, Lund, Sweden.

Hellström, G., Sanner, B., 2000. EED: Earth Energy Designer. User manual, Version 2.0.

Hellström, G., Sanner, B., Klugescheid, M., Gonka, T., Martensson, S., 1977. Experience with the borehole heat exchanger software EED. Proc. 7th Int. Conf. Energy Storage MEGASTOCK 97, 247 - 252.

Hopkirk R.J., Gilby D.J., Rybach L., 1985. Vertical tube earth heat exchangers - The Swiss experience. In: Proc. 1985 International Symposium on Geothermal Energy, US Geothermal Resources Council, 443 - 446.

Hopkirk R.J, Eugster, W.J., Rybach, L., 1988. Vertical earth heat probes: Measurements and prospects in Switzerland. Proc. 4th International Conference on Energy Storage JIGSTOCK 88, 367 - 371.

Houpert, A., Delouvrier, J., Iffly, R., 1965. Fonctionnement d'un doublet hydraulique de refroidissement, La Houille Blanche, n°3, 239 - 246.

Ingersoll, L.R.Plass, H.J., 1948. Theory of the ground pipe heat source for heat pump. ASHVE transactions, Vol. 54, pp. 339 –348.

IPCC, 2001. Climate Change 2001: The Scientific Basis. Contribution of Working Group I to the Third Assessment Report of Intergovernmental Panel of Climate Change. Cambridge University Press, Cambridge, UK. 881 pp.

Kälin, B., Hopkirk, R. J., 1991. Quantitative Empfehlung über den minimalen Grenzabstand einer Erdwärmesonden-Anlage. Polydynamics, Switzerland.

Kappelmeyer, O., Haenel, R., 1974. Geothermics with special reference to application. Geoexploration monographs, Series 1 – No. 4, Editors: Rosenbach, O. and Morelli, C., Gebrüder Börntraeger, Berlin – Stuttgart.

Knoblich, K, Sanner, B., Klugescheid, M., 1993. Energetische, hydrogeologische und Geologische Untersuchungen zum Entzug von Wärme aus dem Untergrund. Giessener Geologische Schriften 43, 192 S., Lenz-Verlag, Giessen.

Kohl, T., Hopkirk, R. J. 1995. "FRACTure" a simulation code for forced fluid flow and transport in fractured porous rock. Geothermics, 24, 345 - 359.

Kohl, T., 1999. Transient thermal effects below complex topographies. Tectonophysics, 306, 311 - 324.

Kohl, T., Brenni, R., Eugster, W.J., 2002. System performance of a deep borehole heat exchanger. Geothermics, 31, 687 – 708.

Kohl, T., 2002. FRACTure (V.3.1) finite element program with WinFra (V.0.59) mesh generation. User manual.

Kohl T., Andenmatten N., Rybach L., 2003, Statistik Geothermische Nutzung der Schweiz für die Jahre 2000 und 2001 – Endbericht, Bundesamt für Energie.

Kurmann, M., 2003. Topogaphieeffekte beim Betrieb von Erdwärmesonden-Anlagen. Diplomarbeit am Institut für Geophysik der ETH Zürich.

Laloui, L., Moreni, M., Steinmann, G., Fromentin, A., Pahud, D., 1998. Test en conditions réelles du comportement statique d'un pieu soumis à des solicitations thermomécaniques. Rapport intermédiaire de juillet 1998. Office fédéral de l'énergie, Bern, Switzerland.

Leu, W., Keller, B., Mégel, T., Schärli, U., Rybach, L., 1999: PC-Programm für die Berechnung geothermischer Eigenschaften der Schweizer Molasse (Tiefenbereich 0 – 500 m). Benutzerhandbuch zu SwEWS (Version 1.0). Bundesamt für Energie, Schlussbericht.

Lewis T.J., 1998. The effect of deforestation on ground surface temperatures, Glob. & Planet. Change, 18,1 - 13

Lewis T.J., Wang K,, 1992. Influence of terrain on bedrock temperatures, Glob. & Planet. Change, 6 (2), 87 - 101.

Lewis T.J., Wang K,, 1998. Geothermal evidence for deforestation induced warming: Implication for climatic impact of land development, Geophysical Research Letters, Vol. 25, No. 4, 535 - 538.

Lund, J., Sanner, B., Rybach, L., Curtis, R., Hellström, G., 2003. Ground-source heat pumps. Renewable Energy World, July-August 2003, 218 - 227.

Maraini, S.. 2000. Vergleich von Software zur Dimensionierung von Erdwärmesonden-Anlagen. Diplomarbeit am Institut für Geophysik der ETH Zürich.

Medici F., Rybach L., 1995. Geothermal map of Switzerland 1:500‘000 (Heat Flow Density). Beitr. Geol. Schweiz, Ser. Geophys. Nr. 30, 36 p.

Medici F., Rybach L., 2002. Switzerland. In. Atlas of geothermal resources in Europe. S. Hurter and R. Haenel (Eds.). Publication number EUR17811 of the European commission.

Meteotest AG/BFE, 1997. METEONORM – Global meteorological database for solar energy and applied climatology. Software and data on CD-ROM, version 3.0, Edition 1997.

Morgensen, P, 1983: Fluid to duct wall heat transfer in duct system heat storage. Proc. Int. Conf. on Surface Heat Storage in Theory and Practice. Stockholm, Sweden, June 6 - 8 1983, 652 – 657.

Pahud, D., 2001. Two response tests of two “identical” boreholes drilled to a depth of 160 m near Luzern. Proceedings: Workshop: Geothermische Response Tests – Tests de Résponse Géothermique. Ecole Polytechnique Fédérale de Lausanne, Seiten 37 - 47.

Pahud, D., Kohl, T., Mégel, T., Brenni, R., 2002. Langzeiteffekt von Mehrfach-Erdwärmesonden. Bundesamt für Energie, Schlussbericht.

Perry, R.H., Chilton, C.H., 1984. Chemical Engineers’ Handbook sixth ed. McGraw-Hill, New York.

Pfister M., Rybach L., 1995. High-resolution digital temperature logging in areas with significant convective heat transfer. Geothermics 24, 95 - 100.

Pikul, J.L. JR., 1991. Estimating soil surface temperature from meteorological data. Soil Science, Vol. 151, No. 3, p. 187 – 195.

Powell, W.G., Chapman, D.S., Balling, N., Beck, A.E., 1988. Continental heat-flow density. In: Haenel, R., Rybach, L. and Stegena, L. (eds.), Handbook of Terrestrial Heat-Flow Density Determination, 167 – 222. Kluwer Academic Publishers.

Rohner, E., 2003. Erdwärmenutzung: Planung und Berechnung von Anlagen. Weiterbildungskurs. Hochschule für Technik und Architektur Luzern.

Rybach, L., Pfister, M., 1994: Temperature predictions and predictive temperatures in deep tunnels. Rock Mech. Rock Eng. 27 (2), 77 - 88.

Rybach, L., Hopkirk, R.J., 1995. Shallow and deep borehole heat exchangers - achievements and prospects. In: Proc. World Geothermal Congress 95, Florence (I), Vol. 3, 2133 - 2139.

Rybach, L., Gorhan, H., 1997. Geothermal R&D in Switzerland: achievements and prospects. In: Proc. NEDO Int. Geothermal Symp. Sendai/Japan, 342 - 350.

Rybach, L., Eugster, W., 1997. Borehole heat exchangers to tap shallow geothermal resource: The Swiss success story. In: S.F. Simmons, O.E. Morgan, M.G. Dunstall (eds.): Proc. 19th New Zealand Geothermal Workshop, 63 - 69.

Rybach, L., Eugster, W., 1998. Reliable long term performance of BHE systems and market penetration - The Swiss success story. In: L. Stiles (ed.): Proc 2nd Stockton International Geothermal Conference, 41 - 57.

Rybach, L., Bunner, M., Gorhan, H., 2000: Swiss geothermal update 1995 – 2000. Proceedings World Geothermal Congress 2000, Kyushu – Tohoku, Japan.

Rybach, L., Eugster, W.J., 2002. Sustainability aspects of geothermal heat pumps. In: Proceedings of the 27th Workshop on Geothermal Reservoir Engineering, Stanford University, California, USA, 55 - 64.

Rybach, L., Bassetti, S., Baumgartner, R., Rohner, E., Schärli, U., 2003. Drahtloser Minidatenlogger für Temperaturmessungen in Erdwärmesonden. Bundesamt für Energie, Schlussbericht.

Šafanda, J., 1999. Ground surface temperature as a function of the slope angle and slope orientation and its effect on surface temperature field, Tectonophysics, 360, 367 – 375.

Salton, M., 1999. Untersuchungen zum Verhalten von Erdwärmesonden. Diplomarbeit am Institut für Geophysik der ETH Zürich.

Sanner, B., 1986. Schwalbach ground-coupled heat pump (GCHP) research station. Newsletter IEA Heat Pump Centre, 4/4, 8 – 10.

Sanner, B., Hellström, G., 1996. „Earth Energy Designer“, eine Software zur Berechnung von Erdwärmesondenanlagen. Proc. 4. Geothermische Fachtragung Konstanz, GtV, 326 - 333.

Sanner, B., Reuss, M., Mands, E, 2000. Thermal response test – Experience in Germany. Proc. of the 8th International Conference on thermal energy storage, Terrastock 2000, 28 August – 1 September 2000, Stuttgart, Germany. 177 – 182.

Sanner, B., Karytsas, C., Mendrinos, D., Rybach, L., 2003. Current status of ground source heat pumps and underground thermal energy storage in Europe. Geothermics, 32, 579 - 588.

Schärli, U., Rybach, L., 1999. D4-Unternehmens- und Innovationszentrum Längebold, Root (LU). Interner Bericht Nr. 4321. Institut für Geophysik, Eidgenössische Technische Hochschule Zürich, Zürich, Switzerland.

Schärli, U., Kohl, T., 2002. Archivierung und Kompilation geothermischer Daten der Schweiz und angrenzender Gebiete. Beitrage zur Geologie der Schweiz, Geophysik Nr. 36. Publiziert durch die Schweizerische Geophysikalische Kommission. Druckerei am Schanzengraben, Zürich.

Schärli, U., Rybach, L., 2002. Bestimmung thermischer Parameter für die Dimensionierung von Erdwärmesonden: Erfahrungswerte – Labormessungen – Response Test. Proceedings: Workshop: Geothermische Response Tests – Tests de Résponse Géothermique. Ecole Polytechnique Fédéerale de Lausanne, Seiten 76 - 88.

Seifert, P., Eugster, W.J., Kälin, B., Hopkirk, R.J., 1992. Auswirkungen von Bergklima und Bodentypen auf das Betriebsverhalten von Erdwärmesonden. Bundesamt für Energiewirtschaft, Schlussbericht.

Shonder, J.A., Beck, J.V., 1999. Determining effective soil formation properties from field data using a parameter estimation technique. ASHRAE transactions, Vol. 105(1), 458 – 466.

Signorelli, S., Kohl, T., Rogg, W., 2002. Validieren das Programms EWS und Optimieren der Erdwärmesondenlänge. Bundesamt für Energie, Schlussbericht.

Signorelli, S., Kohl, T., Rogg, W., Rohner, E., 2003. Produktivitätsuntersuchung des Systems Erdwärmesonde mit Wärmepumpe. Projekt- und Studienfond der Elektrizitätswirtschaft, Schlussbericht.

Signorelli S., Kohl T., 2004. Regional Ground Surface Temperature Mapping from Meteorological Data. Glob. & Planet. Change, 40 (1), 267 - 284.

Signorelli S., Kohl T., Rybach, L., 2004. Sustainability of production from borehole heat exchanger fields. In: Proceedings of the 29th Workshop on Geothermal Reservoir Engineering, Stanford University, California, USA.

Signorelli, S., Bassetti, S., Pahud, D., Kohl, T.. 3D Numerical Modeling of Thermal Response Tests. Submitted to Geothermics.

Smith, M., Perry, R., 1999. In situ testing and thermal conductivity testing. Proc. Of the 1999 GeoExchange Technical Conference and Expo, Oklahoma State University, Stillwater, Oklahoma, May 16 – 19, -.

Spitler, J.D., Yavuzturk, C., Rees, S.J., 1999: More comments on in-situ borehole thermal conductivity testing. The Source, Vol. 12, No. 2, March/April 1999. 4 – 6.

Stalder, T., Hopkirk, R.J.,, Hess, K., 1995. Auswirkungen von Klima, Bodentyp, Standorthöhe auf die Dimensionierung von Erdwärmesonden in der Schweiz. Bundesamt für Energiewirtschaft, Schlussbericht.

VDI Guideline 4640 Part 2, 2001. Thermal use of the underground – Ground source heat pump systems. Editor: VDI Verein Deutscher Ingenieure (The Association of Engineers), VDI-Gesellschaft Energietechnik (VDI-GET) (VDI Society for Energy Technology). Beuth Verlag GmbH, Berlin, Germany.

Wagner, R., Clauser, C., 2002. Berechnung der Entzugsleitung einer Erdwärmesonde: Einfluss von Diffusivität, ihrer Temperaturabhängigkeit und Grundwasserströmung. Proceedings: Workshop: Geothermische Response Tests – Tests de Résponse Géothermique. Ecole Polytechnique Fédéerale de Lausanne, Seiten 89 - 99.

Werner, A., Bigler, R., niederhauser, A., et al., 1996. Grundlagen für die Nutzung von Wärme aus dem Boden und Grundwasser im Kanton Bern. Thermoprogramm Erdwärmesonden, Burgdorf. Schlussbericht. Wasser- und Energiewirtschaftsamt des Kantons Bern (WEA).

Witte, H.J.L., 2001. Geothermal response tests with heat-injection and heat-extraction: application in research and design of geothermal ground heat exchangers. Workshop Geothermische Response Tests - Proceedings. Editors: Eugster, W.J. and Laloui, L.. Ecole Polytechnique Fédérale de Lausanne, Lausanne 25. – 26. October 2001.

Witte, H.J.L., Van Gelder, G., Spitler, J. 2002. In-situ thermal conductivity testing: A Dutch perspective. ASHRAE transactions 2002, Vol. 108, 263 – 272.

WPZ-Bulletin, 2003. Bulletin Nr. 36 (Juli 2003).

Yavuzturk, C., Spitler, J.D., Rees, S.J., 1999. A transient two-dimensional finite volume model for the simulation of vertical U-tub ground heat exchangers. ASHRAE transactions, Vol. 105(2), 465 – 474.

Z'graggen, L., 2001. Strahlungsbilanz der Schweiz. Dissertation Nr. 14158, ETH Zürich.

Zimmermann, K., Kienast, F., 1995. Klimakarten lassen sich nicht kartieren, sie werden gerechnet. Informationsblatt des Forschungsbereiches Landschaftsökologie, Nr. 27 / Juli 1995.

CURRICULUM VITAE

Sarah Franca Signorelli

Date of Birth	25. April 1974
Citizen of	Trimbach (SO), Switzerland

Education

10 / 2000 – 4 / 2004	PhD student at Research Group Geothermics and Radiometrics, Institute of Geophysics, ETH Zürich.
11 / 1999 – 9 / 2000	Technical Assistant at Research Group Geothermics and Radiometrics, Institute of Geophysics, ETH Zürich.
4 / 1999 – 10 / 1999	Diploma in natural sciences. Diploma thesis: Geothermische Messungen im NEAT Schacht Sedrun und ihre Interpretation.
1994 – 1999	Student at the Swiss Federal Institute of Technology Zürich (ETH), Earth Science. Major subjects: Applied and theoretical geophysics, engineering geology.
1981 – 1994	Primarschule Trimbach Kantonsschule Olten